

Optimisation of Fatigue Behaviour of Ti-6Al-4V Alloy Components Fabricated by Metal Injection Moulding

**Vom Promotionsausschuss der
Technischen Universität Hamburg-Harburg
zur Erlangung des akademischen Grades
Doktor Ingenieur (Dr.-Ing.)
genehmigte Dissertation**

von

Orley Milagres Ferri

aus

Belo Horizonte, Brasil

2010

Vorsitzender des Prüfungsausschusses:	Prof. Dr.re.nat. G. Schneider
1. Gutachter:	Prof. Dr.-Ing. R. Bormann
2. Gutachter:	Prof. Dr.-Ing. J. Albrecht
3. Gutachter:	Prof. Dr.-Ing. K.U. Kainer

Tag der mündlichen Prüfung:

29 Oktober 2010

Acknowledgments

Many people contributed to my doctoral thesis over the last three years. Especially, I would like to thank ...

- ... my advisor, Prof. Rüdiger Bormann, for giving me the opportunity to work on this exciting topic, as well as for his guidance, support and motivation.
- ... my co-advisor, Dr. Thomas Ebel, for the excellent orientation and discussions along experimental and written steps of my doctoral thesis.
- ... Prof. J. Albrecht and Prof. K.U. Kainer for co-reviewing the thesis.
- ... present members of the research group of WZM at GKSS: Wolfgang Limberg, Martin Wolff, Andreas Dobernowsky, Prof. M. Dahms and Gitta Hillis.
- ... all former students who worked on term, diploma or master thesis: Juliano Soyama, Gideon Obasi, Akaichi Haithem, Björn Wiese, Arno Twardogorski and Sascha Fensky.
- ... all former students who worked on term of DAAD rise program: Alyson Liser and William Andrew Sharp II.
- ... my wife Lígia for her love, unfailing support and encouragement.

Geesthacht, Oktober 2010

1. Introduction	1
1.1. Scope of the work	2
2. State of the art.....	3
2.1. Ti-6Al-4V alloy	3
2.2. Metal injection moulding process.....	6
2.2.1. Powders for MIM	7
2.2.2. Binder for MIM	7
2.2.3. Injection moulding and debinding.....	8
2.2.4. Sintering	10
2.3. MIM of Ti-6Al-4V alloy	13
2.4. Fatigue	14
2.4.1. Fatigue in Ti-6Al-4V alloy.....	17
3. Experimental procedures	20
3.1. Materials	20
3.2. MIM process.....	20
3.2.1. Binder content	22
3.2.2. Particle size.....	23
3.2.3. Boron addition	23
3.3. The hot isostatic pressing	24
3.3.1. Powder+HIP	24
3.3.2. MIM+HIP	25
3.4. Surface modification and characterisation	25
3.5. Characterization of the samples.....	26
3.5.1. Impurity levels, microstructural features and relative density	26
3.5.2. EBSD measurements	28
3.5.3. Dilatometry.....	28
3.5.4. Tensile test.....	29
3.5.5. Fatigue experiments.....	30
4. Verification of the four-point bending fatigue tests	32
4.1. Experimental procedure.....	32
4.2. Results and discussion	32
5. Results	35

5.1. The MIM31L samples	35
5.1.1. Tensile mechanical behaviour	36
5.1.2. Fatigue behaviour	37
5.2. Binder content.....	41
5.2.1. Microstructural features.....	41
5.2.2. Tensile properties	44
5.2.3. Fatigue behaviour	46
5.3. Shot peening as a surface treatment	48
5.3.1. Fatigue behaviour	48
5.3.2. The internal stresses promoted by the shot peening	52
5.4. Particle size.....	55
5.4.1. Microstructural features and tensile properties	55
5.4.2. Fatigue behaviour	57
5.5. The MIM+HIP configuration	59
5.5.1. Microstructural features.....	59
5.5.2. Tensile properties	60
5.5.3. Fatigue behaviour	61
5.6. The Powder+HIP configuration.....	64
5.6.1. Microstructural features.....	64
5.6.2. Tensile properties	66
5.6.3. Fatigue behaviour	67
5.7. Addition of boron on Ti-6Al-4V alloy	70
5.7.1. Boron content	70
5.7.2. Dilatometry.....	72
5.7.3. Impurity levels and microstructural features.....	74
5.7.4. Tensile properties of the Ti-6Al-4V-0.5B alloy	79
5.7.5. Fatigue behaviour	80
6. Discussion.....	84
6.1. The influence of interstitial elements on the mechanical properties of MIM samples	84
6.2. Ti-6Al-4V alloy processed by MIM.....	85
6.2.1. Tensile properties	86

6.2.2. Fatigue behaviour	86
6.3. Influence of surface quality	88
6.3.1. Influence of the binder content.....	89
6.3.2. Influence of shot peening	92
6.4. Influence of the porosity.....	95
6.4.1. Influence of the particle size.....	95
6.4.2. Influence of the HIP process	96
6.5. Influence of the microstructure morphology	98
6.5.1. Microstructural features.....	99
6.5.2. Tensile properties	99
6.5.3. Fatigue behaviour	100
6.6. Enhancement of the high cycle fatigue behaviour of the MIM components by microstructure design	101
6.6.1. Variation of boron content.....	102
6.6.2. Sintering process	102
6.6.3. The microstructure of Ti-6Al-4V-0.5B alloy sintered at 1400 °C	104
6.6.4. The tensile property of Ti-6Al-4V-0.5B alloy sintered at 1400 °C.....	106
6.6.5. Fatigue behaviour of Ti-6Al-4V-0.5B alloy sintered at 1400 °C.....	107
7. Conclusions	109
8. Suggestions for future work	112
References	114
Tables	123
Figures	125
Abbreviations index.....	132

1. Introduction

Research on titanium and its alloys is of great interest because of their unique combination of properties such as: high specific strength, outstanding corrosion resistance and biocompatibility [1]. Titanium is a nearly ideal material for the development of bone reinforcement and replacement products [2]. Furthermore, special attention has been given to extending the application of titanium in the automotive industry due to demands to reduce energy consumption [3]. In terms of space technologies, e.g. the Ti-6Al-4V alloy has been widely used as a viable engineering material [4]. However, due to the rather high costs of processing and raw materials, the use of titanium alloys in mass production remains limited.

Powder metallurgy (PM) has been used to lower the cost of titanium alloy parts since the 1970s [5]. In contrast to traditional PM techniques such as pressing, metal injection moulding (MIM) combines the materials flexibility of powder metallurgy with the design flexibility of plastic injection moulding. Nowadays, it is possible to fabricate Ti-6Al-4V alloy components produced by MIM with excellent tensile properties (UTS > 800 MPa, $\epsilon > 14\%$) [6]. However, components such as permanent implants, automotive parts and some special aerospace parts require extremely high reliability, when e.g. dynamic loading is applied. Unfortunately, the performance of the MIM components with respect to fatigue resistance is not as good as demonstrated for the static tensile behaviour. A recent investigation [7] demonstrated that the fatigue endurance limit of the Ti-6Al-4V alloy at 10^7 cycles is approximately 380 MPa. This value is significantly lower than the value found, typically around 600 MPa, for annealed, wrought material with its usual lamellar microstructure [8, 9]. Moreover, it is much lower compared to the thermo-mechanically treated Ti-6Al-4V alloy with an equiaxed microstructure which exhibits an endurance limit typically above 800 MPa [10-12].

It has been assumed so far, that the main factors responsible for such behaviour are related to surface quality and the presence of pores. Nevertheless, it is important to point out that no systematic study of the influence of these features on the fatigue behaviour of Ti-6Al-4V alloy processed by MIM has been carried out to date. Furthermore, the interaction between microstructural features such as porosity, grain size and impurity

levels with the fatigue behaviour of MIM components remains unclear. Consequently, if Ti-6Al-4V alloy components fabricated by the MIM technique are to be used in applications where fatigue resistance in the range of wrought material is required, then identification of the critical features responsible for the degradation of fatigue behaviour of the MIM parts is necessary.

1.1. Scope of the work

In the present work, the high cycle fatigue behaviour of Ti-6Al-4V components fabricated by MIM is investigated in detail. Experiments were conducted in an attempt to determine the influence of critical features such as surface quality, porosity and microstructural features on the fatigue behaviour of MIM Ti-6Al-4V components. In order to identify the crack initiation mechanism, detailed examination of the fatigued fracture surfaces was performed. In a second step, the fatigue response of different configurations is described in terms of tensile properties, microstructural features, surface quality and composition.

The present work contributes to the understanding of the influence of surface quality, microstructural features and process parameters on the fatigue behaviour of MIM Ti-6Al-4V components. Based on this comprehensive understanding, an alloy has been designed with the microstructural features required to minimise the degradation of the high cycle fatigue behaviour resulting from the presence of inherent MIM processing defects.

2. State of the art

2.1. Ti-6Al-4V alloy

Titanium was first discovered by the mineralogist and chemist, William Gregor in 1791. Four years later, Martin Klaproth, based on the story of the Greek mythological children, the Titans, named the element as titanium. After that, more than 100 years were necessary to isolate the titanium metal from its oxide. Finally, the first alloys, as well as the popular Ti-6Al-4V alloy, were developed in the late 1940s. The Ti-6Al-4V alloy is the most common used alloy among the commercially available titanium alloys. The reason for this success is the good balance of its properties and the intensive development and testing of this alloy during the approximately last 60 years [13].

Ti-6Al-4V alloy belongs to the group of $\alpha + \beta$ titanium alloys. The aluminium acts as a α stabilizer and the vanadium as a β stabilizer. At this specific composition both phases, α and β , are presented in the microstructure at room temperature. Typically, three different microstructure morphologies can be obtained by changing the thermo-mechanical processing route: fully lamellar structures, fully equiaxed structures, and so-called bi-modal microstructures [14].

The fully lamellar microstructure (Fig. 1b) is characterized normally by packages of lamellae. The typical thermo-mechanical processing route applied to obtain the fully lamellar microstructure is schematically illustrated in Fig. 1.

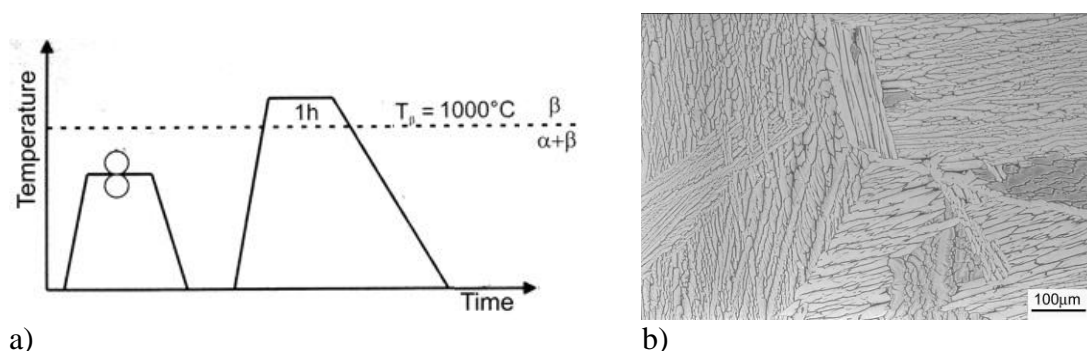


Fig. 1. Figure (a) illustrates the processing route for fully lamellar microstructure, and (b) the resultant microstructure.

The most important parameter in the processing route is the cooling rate from β phase field during the recrystallization step since it delineates the size of the α lamellae, the α colony size and the thickness of the α layers at β grain boundaries. In the fully lamellar microstructure the α colony size, alternating α and β plates with distinct orientation relationship, is the feature that defines a grain, or in other words, the size of the slip length during plastic deformation. Thus this feature determines mechanical properties such as tensile yield strength and high cycle fatigue strength.

In the case of fully equiaxed (Fig. 2b) microstructure the typical thermo-mechanical treatment is illustrated in Fig. 2a.

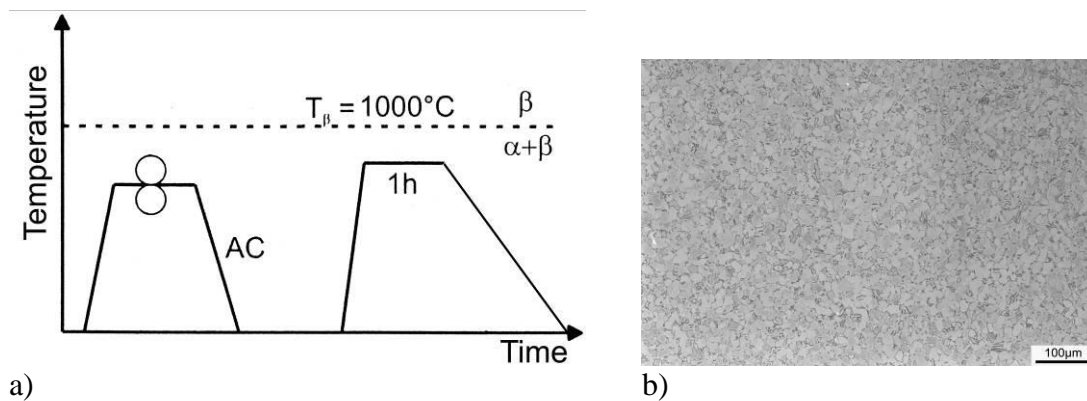


Fig. 2. Figure (a) illustrates the processing route for fully equiaxed microstructure, and (b) the resultant microstructure.

Again, the critical process segment is related to the cooling rate of the recrystallization process step. The cooling rate needs to be sufficiently low in order to allow only growth of α grains with no formation of α lamellae within the β grains, resulting in an equilibrium volume fraction of β phase located at the “triple-points” of the α grains. The microstructure feature that defines the grain size or the slip length for this microstructure is the α grain size.

Finally, the bi-modal microstructure (Fig. 3b) is obtained from the typical process route shown in Fig. 3a.

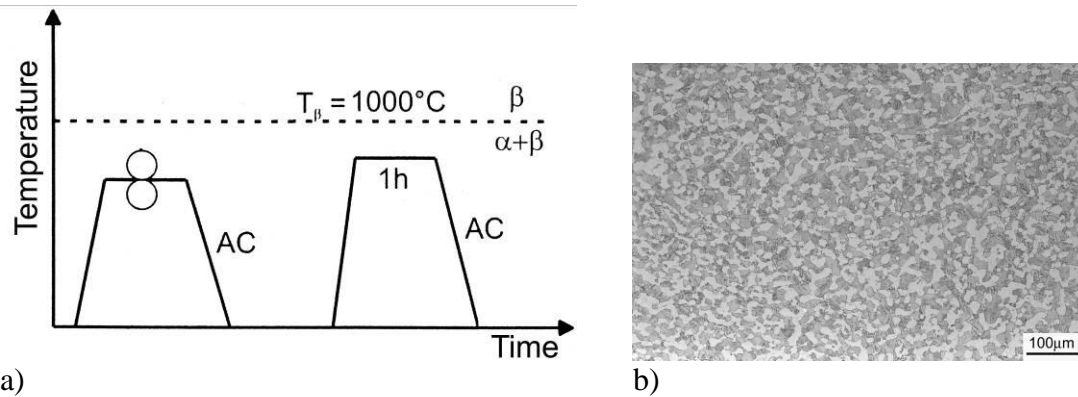


Fig. 3. Figure (a) illustrates the processing route for bi-modal microstructure, and (b) the resultant microstructure.

The microstructure consists of equiaxed primary α grains situated at the triple points of β grains. The background of matrix constituent, often referred to as “transformed β ,” contains a lamellar structure of β phase plus secondary α lamellae. For the bi-modal microstructure the feature that defines the slip length is the distance between the equiaxed primary α grains.

Among the microstructures cited above, the fully lamellar microstructure is usually the microstructure obtained after sintering the Ti-6Al-4V alloy powder processed by MIM. The two most relevant parameters during the sintering process are the maximum sintering temperature and, as for the thermo-mechanical process route, the cooling rate. These two factors will determine the α colony size and consequently the mechanical properties.

Besides the difference in microstructure morphology, another important feature that describes the mechanical properties of Ti-6Al-4V alloy is the amount of interstitial elements, such as O, C and N. Conrad [15] proposed an equivalent oxygen content ($O_{(eq.)} = O + 2N + 0.75C$) in order to describe the effect of dislocations-impurity interaction on the tensile properties of commercial titanium alloy. Furthermore, Meester et al. [16] noticed that the interaction of dislocations with interstitial impurities (C, N and O) for the Ti-6Al-4V alloy was similar to that for unalloyed titanium. In general the tensile strength and the high cycle fatigue strength increase with a subsequent increase

of $O_{(eq.)}$ [14, 17] whereas the ductility and specially the fracture toughness decrease with a higher amount of interstitial elements [18-20].

2.2. Metal injection moulding process

The idea of using thermoplastics as vehicle for metal or ceramic powders to get moulded parts of a desired shape has been developed since the late 1920's [21]. Evolution of this process idea in terms of maximization of the solid particles content and the extraction of the thermoplastic polymer binder during sintering allowed the production of metals and ceramics parts with a highly complexed shape, low cost forming, and high performance properties [22]. Consequently, this new process named powder injection moulding (PIM) combines the advantages of powder metallurgy process with the design flexibility of thermoplastic injection moulding technique [23, 24]. If ceramics are used, the process is termed "ceramic injection moulding" (CIM) and if metals are applied the term is "metal injection moulding" (MIM) [23, 25]. The principle of the MIM process is illustrated in Fig. 4, displaying the technique performed at GKSS. Initially, powder and thermoplastics are mixed by using kneaders in order to obtain the feedstock. This feedstock is heated and injected into a mould using a conventional injection moulding machine. After injection, the moulded part or the so called green sample is exposed to chemical debinding. Usually, one component of the binder system is removed in the chemical debinding step with the objective of opening micro-channels in the sample to facilitate the extraction of the remaining binder during following thermal debinding. Finally, the sample is exposed to thermal debinding and sintering in a single furnace run.

It is important to note that MIM of ferrous materials is a well establish fabrication process. Nowadays, there is even an ASTM standard (ASTM B883-05) with acceptable chemical composition levels and minimal tensile properties values for the most common ferrous alloy such as: MIM 2700 low alloy steel, MIM-316L austenitic stainless steel or the MIM-17-4PH precipitation hardening stainless steel. Unfortunately, such a standard does not exist yet for the MIM titanium alloys. This contributes to the actual lack of available data related to the desired chemical composition and/or mechanical properties of the MIM titanium alloys.

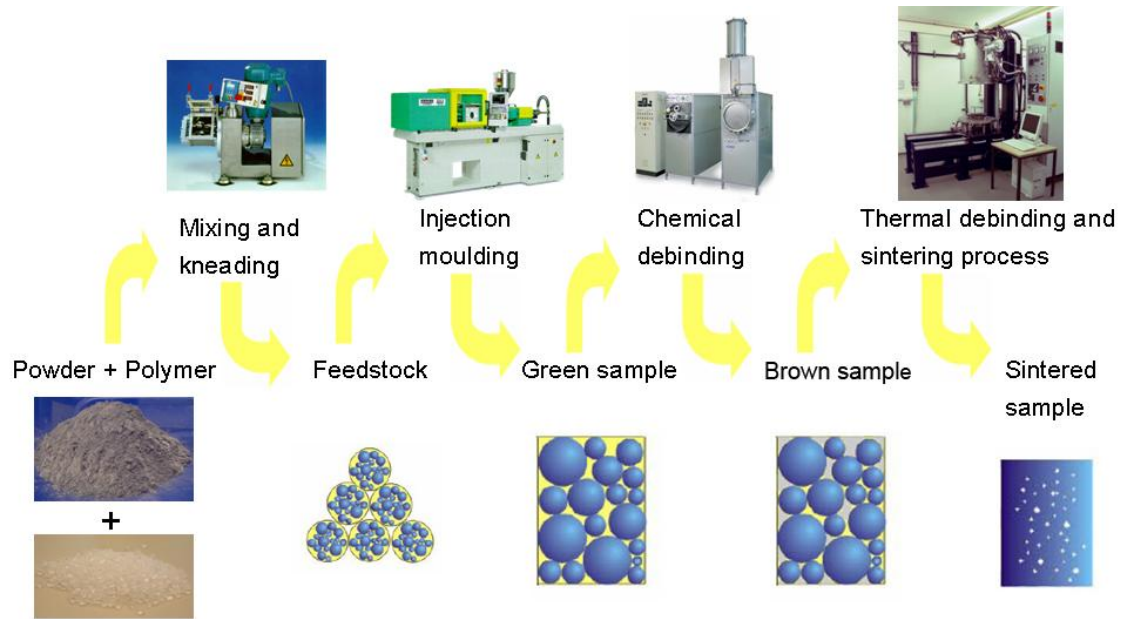


Fig. 4. A schematic diagram of the processing steps, equipments involved and sample configuration in powder injection moulding.

2.2.1. Powders for MIM

Particle morphology has a large effect on the success of the MIM process. While irregular particles exhibit better moulded parts shape retention during binder removal, the packing coordination number and density are degraded by an irregular particle shape. The particles size may be in the range between around 1 μm up to 45 μm . Coarser powders are usually not used because their lack of sintering activity [26]. In terms of titanium powders, three main different kinds of powders exist: sponge fines, hydride-dehydride (HDH) and gas atomised powder. The sponge fines and HDH powders are cheaper for MIM production compared to atomised powders. However, due to irregular particle morphology, which reduces the maximum powder loading of the feedstock, the sponge fines and HDH powders are typically deprecated in favour of atomised powders [23, 27].

2.2.2. Binder for MIM

A primary requirement of the binder is that it allows flow and packing of the particles into the mould cavity [28]. The binder is usually designed as a multi-component system.

The backbone component, typically a thermoplastic, retains the moulded shape during all phases prior to the later stages of debinding. The second component, which is typically a wax, has the function to improve the flowability of the mixture. Furthermore, as the wax is the first component to be extracted during debinding, open pores will be created. This will allow the gaseous products of the remaining polymer to diffuse out of the structure without generating an internal vapour pressure that might cause compact failure. In addition, removal of half the amount of binder means to reduce the potential pick-up of carbon during thermal debinding significantly. Finally, additives such as surfactants are added in order to reduce the contact angle by lowering the surface energy of the binder-powder interface [29, 30].

Currently, there are a number of binder systems, e.g. Polyethylene, Paraffin, Stearic Acid [31], Naphthalene, Stearic Acid, Polyethylene Vinyl Acetate [32] and etc., which appear to have the necessary characteristics to process titanium alloys by MIM technology approach.

2.2.3. Injection moulding and debinding

In the injection moulding process, temperature and pressure are varied to deliver the feedstock to the mould cavity. During injection the so called “jetting filling” (Fig. 5) should be avoided, because of the associated surface weld lines and trapped air defects. The progressive mould filling is most desirable for a successful production of parts by the injection moulding technique [22].

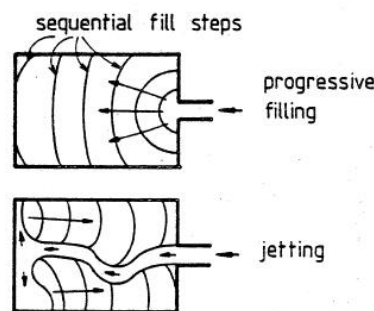


Fig. 5. A schematic comparison of the sequential feedstock flow in progressive mould filling and jetting [22].

In terms of rheological behaviour, the feedstock should exhibit a pseudo-plastic flow characteristic [33]. Pseudo-plastic flow refers to a substance that demonstrates a decrease in viscosity as the shear rate increases. Apart from shear rate, in general the viscosity of the feedstock is also dependent of temperature, powder loading, powder characteristics and the binder system composition. It is desirable that the viscosity of the feedstock should decrease quickly with increasing shear rate during moulding. The shear thinning of MIM feedstock with the increase of shear rate results from the powder particle ordering and the binder molecule orientation with flow [34]. Empirical studies have demonstrated that a viscosity of less than 10^3 Pa·sec is desired in order to obtain flow conditions. Furthermore, during moulding the shear rates usually ranges between 10 and 10^5 sec⁻¹, with the low shear rate at the walls and the high shear rate at the gate [35, 36]. Because of so large variations of the viscosity and non-homogeneous viscosity distribution during the filling process, it is possible that at critical conditions powder binder segregation or other defects related to the filling behaviour occur [37].

The binder removal process includes a series of physical or chemical process such as the transport of the evaporated or decomposed binder phase to the surface through the connected pore channels inside of the compacts, the flow and redistribution of liquid binder phase in compacts due to capillary forces and the evaporation or decomposition of the binder components [38]. The spaces between the powder particles, which are filled with the binder phase, are opened gradually during the first step of debinding process. Barone et al. [39] and Cima et al. [40] observed that after approximately 40% binder extraction the connected pore channels were formed in the moulded parts. These connected pore channels are essential for the subsequent debinding of the remaining binder.

Potential defects formed during debinding consist of internal cracks, distortion, slumping, warping, surface pits and discoloured spots [41]. Fig. 6 illustrated several possible defects in a cross sectioned MIM part. These defects are created due to inhomogeneous mixture, mould filling errors or wrong debinding parameters. In order to achieve good mechanical properties such defects should be eliminated or minimized by changing the MIM process parameters.

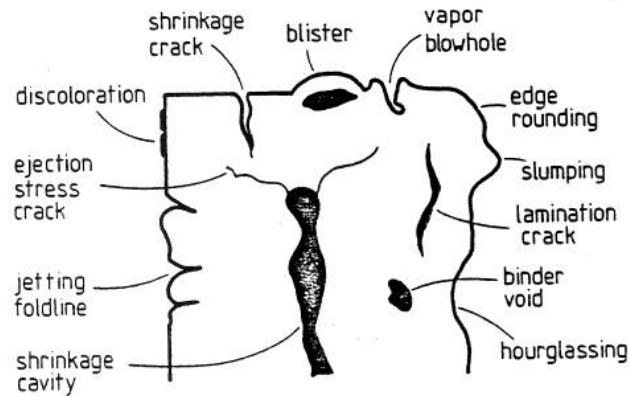


Fig. 6. Possible defects in a MIM component that might be noted after debinding or sintering process [22].

2.2.4. Sintering

Sintering is a process where particles bond together by atomic motions acting to reduce the high surface energy associated with an unsintered powder [42]. Theoretical concepts of sintering are based on thermally activated processes effecting the growth of contacts between particles and their coalescence [43]. Thus, local kinetics of the process, contact formation and driving force nature have been studied to a large degree [44-46]. The main driving force for the sintering process is the reduction in surface free energy of the particle. The reduction is achieved mainly by diffusional transport of material from the centres of particles to the particle-particle necks [47]. Basically, mass transport during sintering without liquid phases have been discussed under two categories for polycrystalline materials:

- diffusion mechanism and
- plastic deformation mechanism.

The first mechanism can be divided in three main segments:

- evaporation-condensation mechanism,
- surface diffusion mechanism and
- volume diffusion mechanism.

Surface diffusion and evaporation-condensation mechanisms are transport mechanisms that can produce surface smoothing, particle joining and pore rounding, but do not

produce volume shrinkage [48]. Alternatively, the volume diffusion is fairly important to the densification of sintered materials. The volume diffusion can be further divided in lattice diffusion and grain boundary diffusion.

The second mechanism was postulated by Lenel [49] and is more applicable to the early stage of sintering where a dislocation climb mechanism may be rate controlled by the diffusion of vacancies toward the dislocations. The experimental evidence which has been presented in support of the deformation mechanism for material transport is strong, especially under pressure condition, e.g. sintering with hot isostatic pressing (HIP) [46].

However, in the absence of an applied pressure the available stress in the system is insufficient to nucleate new dislocations [22, 50]. Furthermore, Taskinen [51] demonstrated for a carbonyl nickel powder that the material transport in the sintering of normal powder (particle size 50 to 500 μm) is never controlled or dominated by dislocation motion. Only in the case of micron-size particles is it possible for dislocations to be the dominated material transport mechanism.

In order to better understand the sintering behaviour of a given material, the process is typically divided in three stages [42]:

- initial stage: the particles form bonds at the particles contacts and a fully interconnected pore structure with a rough pore shape are presented,
- intermediate stage: at this point significant densification occurs, where the density is normally in the range of 70 to 92% of the bulk value. The interaction between pores and grain boundaries is crucial for the further densification.
- final stage: the pores at this stage tend to be isolated and rounded. Further densification is nearly inhibited since vacancy diffusion through the lattice to the grain boundaries is required in order to eliminate the isolated pores. In general coarsening of the microstructure is also observed at this stage.

During sintering of a powder compact, both densification and grain growth occur simultaneously [52-54]. It has been recognised that the relationship between densification and grain growth must be assessed in order to understand and control the sintering process. A prominent approach is to investigate the interaction between pores and grain boundaries. These interactions can be expressed into three forms: the pores

can act as a barrier for grain growth [55], the pores can be dragged by the grain boundaries, or the grain boundaries can break way from the pores, leaving them isolated in the grain interior [42]. The first and the second situation are favourable to the densification whereas the third situation supports the coarsening of the microstructure. Brook [56] explained the breakaway of the grain boundaries from the pores in terms of pores and grain boundary mobility. Separation of pores from the grain boundary will occur, when pore and grain boundary velocity become different. Additionally, he demonstrated that the pore and the grain boundary mobility are related to the size of these features. Fig. 7 illustrated schematically when the breakaway occurs as a function of grain and pore sizes for a hypothetical system.

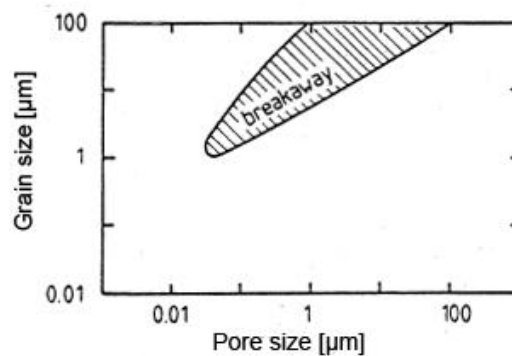


Fig. 7. Grain size and pore size interaction during sintering, showing the condition where breakaway may occur [56].

Pores and second phase inclusions may inhibit the grain boundary migration and can be used to improve densification since the pores located at grain boundaries can be removed faster by grain boundary diffusion than those located in the interior of the grains [54].

Another attractive option for increasing the final densification of sintered parts is the utilization of additional phases which improve the diffusion rates by stabilizing desirable crystal structures or, more typically, to form a liquid phase to increase the sintering rate [57].

Despite a strong research activity for decades, numerous questions remain open, in particular when real systems are concerned. The main problem of real system is the fact that the sintering kinetics of real porous bodies is determined not only by the properties of the particles and the nature of their interaction, but also by macroscopic factors such as defects due to powder packing faults, presence of inclusions, particle rearrangement and anisotropic shrinkage [43].

2.3. MIM of Ti-6Al-4V alloy

A major concern of titanium alloys is their high manufacture cost compared to steels or aluminium alloys. In order to reduce these cost near net shape techniques such as MIM and precision casting have been successfully applied in the fabrication e.g. of Ti-6Al-4V alloy [8, 27, 58, 59]. MIM is basically the approach of choice when a large number of small parts of highly complex shape are required [60]. However, the unsuccessful application of MIM technology in the mass production of titanium parts during the last decades was mainly related to the unavailability of suitable powder and to inadequate sintering atmosphere and binders for a material as reactive as titanium [61]. However, nowadays it is possible to produce Ti-6Al-4V components fabricated by MIM with excellent mechanical properties at a tolerable impurity level [6, 62-65]. Gas atomised spherical and prealloyed titanium powders are currently the best option among the available powders for obtaining MIM components. A maximum oxygen content of 0.2 wt.% and tensile elongation in the range of 15 % [62] are achievable. Nevertheless, the powder cost is a barrier to widespread applications. An alternative could be the use of HDH titanium powder. Unfortunately, poor rheological properties and sintering activity due to irregular particle shape and often too contaminated powders leading to insufficient tensile properties are obstacles for the application of HDH titanium powder in MIM process for commercial applications [66, 67].

An essential problem in using the MIM technology for small and complicated titanium parts is the high affinity of the powder towards carbon, oxygen and nitrogen. As discussed in section 2.1 these elements tend to affect the mechanical properties of titanium alloys and for many applications the loss of ductility due to high impurities level is unacceptable [68]. Recently, much effort has been put into regulating powders,

modifying binders and optimising other MIM process steps in order to reduce contamination [69].

2.4. Fatigue

The study of the fatigue of materials and structures started in the nineteenth century because of the appearance of service fractures during cyclic loading of components at relative low loads e.g. below the yield strength [70]. One of the first studies concerned with the identification of the phenomenon of fatigue was carried out by Wöhler [71]. In his study Wöhler investigated the dependence of the stress on the number of loading cycles to complete fracture. The maximum stress at which fracture does not occur even after a very high number of loading cycles (of the order of 10^7) was assumed to be the fatigue limit. The relationship between stress and cycles was believed to be as a rectangular hyperbolic relationship with a horizontal asymptote (fatigue limit) [70]. However, such condition may not exist for all metallic materials as reported by Bathias [72]. He noticed that for the Ti-6Al-4V alloy fatigued up to 10^9 cycles the fatigue limit was approximately 100 MPa lower than the values obtained at 10^7 cycles.

The fatigue process has proved to be very difficult to study. Nonetheless, the basic principles of fatigue behaviour of metallic materials has been summarised in numerous publications [73, 74]. Now, it is generally agreed that four distinct phases of fatigue may occur [17]:

- nucleation,
- structurally dependent crack propagation (microstructurally short cracks phase),
- crack propagation that is described by either linear elastic, elastic-plastic or fully plastic fracture mechanics and
- final instability.

A more general approach separates the fatigue life of a component in two parts: the fatigue crack initiation and the fatigue crack propagation. During high cycle fatigue regime the crack initiation phase, which includes nucleation and propagation of microstructurally short cracks, is the determinant phase. In case of normally processed samples, it is assumed that approximately 90 % of the total fatigue life is determined by the crack initiation phase [75]. Additionally, the period of crack nucleation in smooth

specimens without defects is assumed to be in the range of 5-20 % of the fatigue life. The major part of the life is spent in the growth of microstructurally short cracks [76]. Consequently, in order to predict the fatigue response of a given material it is essential to identify and understand the dominant mechanisms during nucleation and propagation of microstructurally short cracks propagation.

Crack nucleation in ductile metals is often associated with local plastic deformation. In the absence of metallurgical defects such as casting pores or impurity inclusions, fatigue crack in single-phase materials initiate at the surface [77]. Surface cracks are typically observed to form at the following sites: slip bands, grain boundaries, precipitates, dispersoids and twin boundaries. All of these regions are subject to stress concentrations and thus to a possible localized plastic deformation.

Among possible sites of crack initiation, the slip band is preferentially the one for pure single-phase metals [78]. The cyclic strain is concentrated along the slip band and extrusion or intrusion is accompanied with it. The models proposed to explain such phenomenon are based on Mott's assumption [79], that dislocations move along different paths in the slip bands under forward and reverse loadings. Fig. 8 illustrates schematically the crack initiation due to irreversible slip bands.

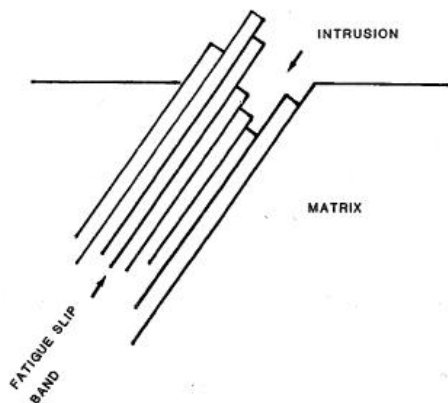


Fig. 8. Schematic illustration of single slip system of intrusion formation [80].

In polycrystalline metals, however, the grain boundary is often an additional relevant factor for the crack initiation. During cyclic deformation, the grain boundary serves as an obstacle to the slip bands resulting in the build-up of high stress concentration at the

boundary. Such high stress concentrations promote early crack initiation during fatigue [76, 81].

Recently, Miller [82] introduced the concept of microstructure fracture mechanics (MFM) which is essential in order to understand the very long-life fatigue failures ($10^6 - 10^{12}$ cycles). Basically, he emphasized the existence of two fundamentally different conditions in polycrystalline metals, one related to long crack growth behaviour involving minimal effects of microstructure, and another concerned with microstructure dominated threshold condition. Furthermore, he pointed out that the fatigue limit of most materials does not reflect the critical stress for crack initiation, but the threshold stress for non-propagation of the crack emanating from original cracks, defects or inhomogeneities. Finally, he highlighted the statement of Kitagawa and Takahashi [83] that linear elastic fracture mechanics (LEFM) should not be applied to either physically small or microstructurally short cracks since the assumption of small-scale yielding conditions at such short cracks does not apply.

Fig. 9 depicts the typical situation in the early growth stage of a microstructurally short crack in an f.c.c polycrystal. In a large surface grain a crack is nucleated along persistent slip bands or along twin boundary, i.e. in a $\{111\}$ crystallographic plane of the grain. When the crack reaches the boundary, two favourable oriented slip systems become active in the neighbouring grains. Only if such a grain is oriented for single slip the crack can advance along the $\{111\}$ planes. A unique crack front is only formed if the crack growth in all the neighbouring grains is correlated. Consequently, some cracks will stop due to the unfavourable slip plane orientation. This leaves secondary cracks that are often identified on the fracture surface [84].

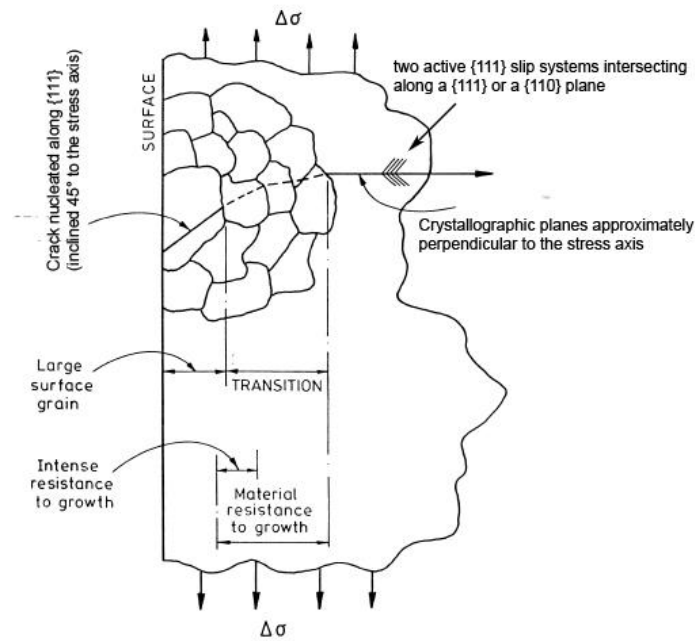


Fig. 9. Schematic of the growth of microstructurally short cracks in a polycrystal.

2.4.1. Fatigue in Ti-6Al-4V alloy

The resistance to fatigue crack initiation for titanium alloys decreases with coarsening of the microstructure. Fig. 10 shows the S-N curves of differently processed Ti-6Al-4V specimens. Typically, fine equiaxed microstructure produced by thermo-mechanical treatment exhibits higher fatigue resistance than the coarse cast lamellar structures.

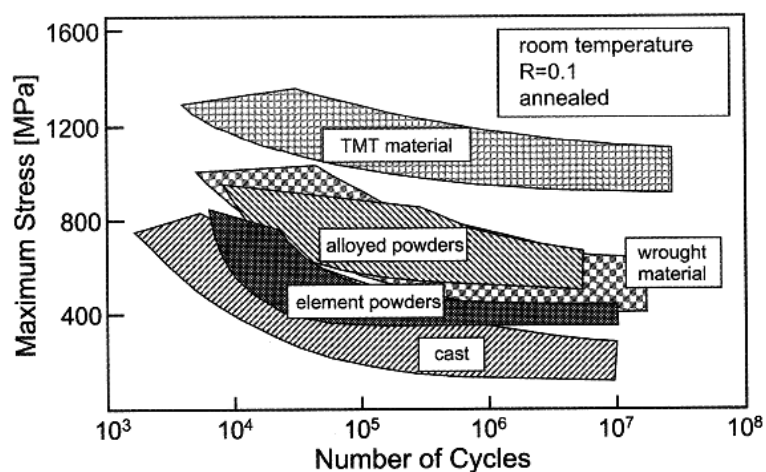


Fig. 10. High cycle fatigue behaviour of Ti-6Al-4V alloy obtained by different processes route [85].

Stubbington and Bowen [86] investigated the influence of microstructure size on the fatigue behaviour of Ti-6Al-4V alloy. They conclude that by refinement of the microstructure from fully lamellar to an equiaxed microstructure, the fatigue strength could be improved from 440 MPa to 670 MPa.

Generally, the high cycle fatigue strength at 10^7 cycles is directly related to the resistance against fatigue crack nucleation [14]. In terms of fatigued fracture surfaces, normally the crack initiation sites are characterized by a faceted fracture surface [87]. For example, fatigue cracks in fully lamellar microstructure nucleate at slip bands within the α lamellae or at α zones along beta grain boundaries [17].

The first model accounting for the formation of facets due to the dislocations pile-up at a critical point (e.g. grain boundaries) was proposed by Stroh [88]. Fig. 11 illustrated the model that describes the quasi-cleavage facets formation in titanium alloys.

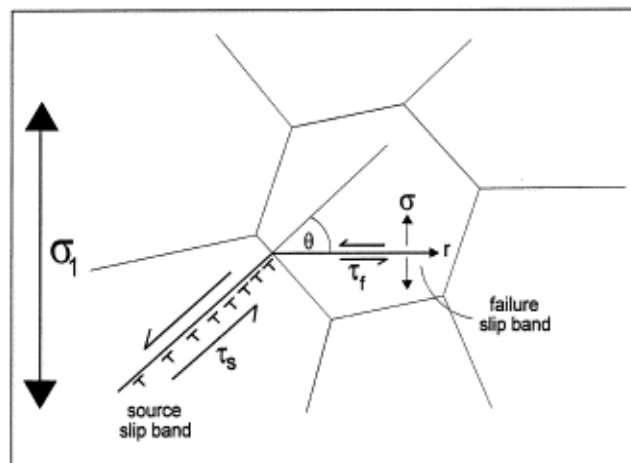


Fig. 11. Stroh's model to describe quasi-cleavage facets formed in titanium alloys [88].

It is important to note that the term “quasi-cleavage” does not mean that the facet is created in a single load cycle (brittle fracture mechanism), but instead due to the gradual separation of slip damage concentrated within a persistent planar slip band [89]. In a recent publication Pilchak et al. [90] suggest that all terminology with the word cleavage for the description of the facets formation on the titanium alloys should be abandoned in favour of low ΔK faceted growth. They argued that this term is intended

to be a phenomenological descriptor that does not imply anything about the number of load cycles required to produce the facet.

Tanaka and Mura [91, 92] proposed a model that during fatigue loading, irreversible slip occurs in a favourably oriented surface grain, leading to dislocation motion on a slip plane (I), see Fig. 12, and dislocation pile-up at grain boundaries. During unloading, dislocations with opposite signs are activated on an adjacent plane (II), producing reverse slip and the formation of vacancy and interstitial dislocation dipoles at the ends of the double pile-up. Consequently, the crack nucleation is assumed to be related to the stored energy in the dislocation dipoles.

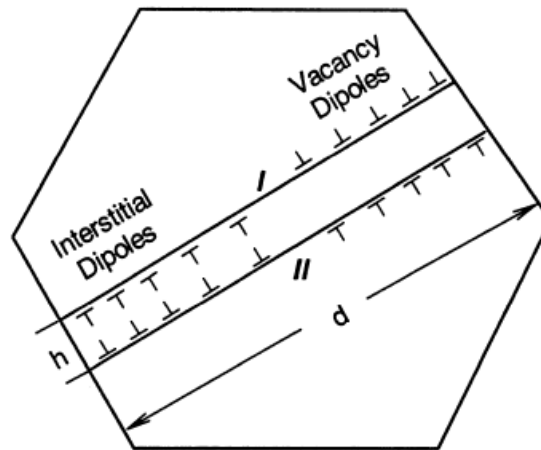


Fig. 12. A schematic showing the fatigue crack initiation process along a planar slip band due to dislocation pile-up. (d) is referring to grain size and (h) is the slip band width [91].

A prominent modification of this model has been made by Chan [93] which includes crack size and relevant microstructural parameters. Although the slip band width (which is related to the work hardening behaviour of the material) was used as fitting parameter, excellent agreement between the model and experimental data was obtained for different materials including Ti-6Al-4V alloy [84].

3. Experimental procedures

3.1. Materials

The materials used in this work are gas atomised spherical Ti-6Al-4V alloy ASTM grade 23 (ELI – extra low interstitial) powder with particle diameter $< 45 \mu\text{m}$, supplied by TLS Technik GmbH, Germany and amorphous boron powder (grade I, 95% purity) with a particle diameter $< 2 \mu\text{m}$, supplied by H.C. Starck. The Ti-6Al-4V ELI (Fig. 13) alloy powder has been produced by argon gas atomisation with respective impurity levels of: $1000 \mu\text{g/g}$ in O, $100 \mu\text{g/g}$ in N and $200 \mu\text{g/g}$ in C.

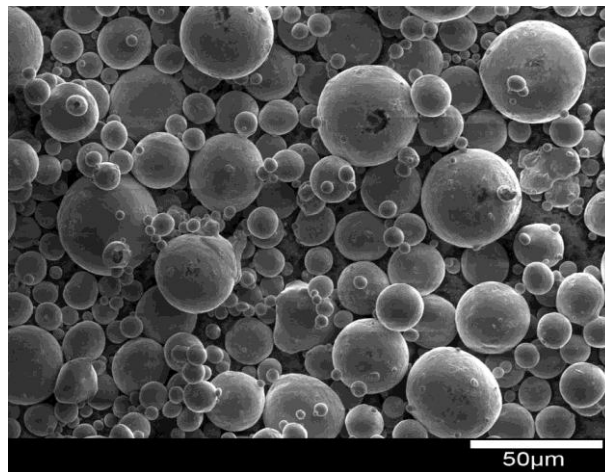


Fig. 13. Scanning electron microscope image (SE-mode) of the powder size fraction used for the present metal injection moulding experiments.

The amorphous boron powder exhibited maximal impurity levels of: $15,000 \mu\text{g/g}$ in O, $2,000 \mu\text{g/g}$ in N and $5,000 \mu\text{g/g}$ in Mg. The binder system used in this study consisted of 60 wt.% paraffin wax, 35 wt.% polyethylene vinyl acetate (EVA) and 5 wt.% stearic acid.

3.2. MIM process

The feedstock (mixture of metallic powder and binder) contained 31 vol. % of a binder system. The metallic powder (Ti-6AL-4V ELI) and the binder system were mixed in a Z-blade mixer at a temperature of $120 \text{ }^\circ\text{C}$ for two hours under argon atmosphere. After

granulation the feedstock was injection moulded using an Arburg 320S machine. As moulded, the bending fatigue specimens and “dog-bone” specimens measured approximately 10 % bigger than the nominal values presented in Fig. 14 and Fig. 15, respectively.

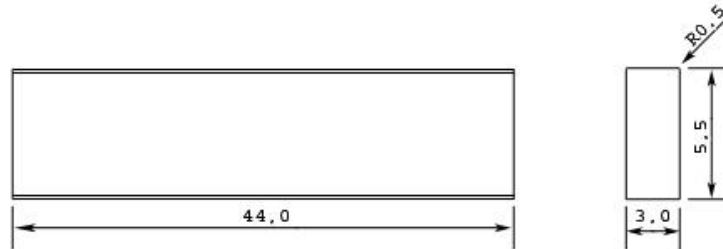


Fig. 14 – Geometry of bending fatigue specimens. Dimensions of as sintered part and measured in millimetres.

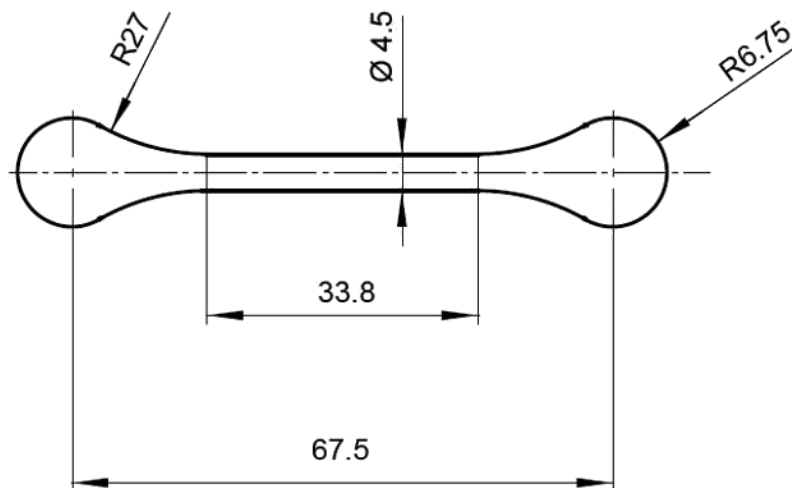


Fig. 15 - Geometry of “dog-bone” tensile test specimen. Dimensions of as sintered part and measured in millimetres.

The paraffin was removed by chemical debinding with heptane at 40 °C during 20 h. Final removal of the remaining binder and subsequent sintering were carried out in a single-step heat treatment run. Sintering was conducted in a cold wall furnace with tungsten heating elements and shield packs of molybdenum. Sintering was performed in vacuum of 10^{-5} mbar at 1250 °C with a holding time of two hours, followed by controlled furnace cooling (10 °C/min).

The samples processed with the parameters described above will be referred to as MIM31L (L is related to “low” sintering temperature and “31” refers to the corresponding volume percentage of binder in the feedstock). It is important to note that these samples are assumed for this investigation to be the starting point condition. Further experiments were planned based on the results obtained for this configuration. In one attempt to separate the influences of critical parameters such as surface quality, porosity and microstructural features on the fatigue behaviour of the MIM components the following approaches were used:

- Surface quality → samples with different binder content or surface treatment.
- Porosity → samples with different initial powder size or application of HIP on sintered samples.
- Microstructure features → samples with different grain size or microstructure morphology by means of alloy modification or a powder+HIP manufacture route.

In the following only the difference in processing between the MIM31L samples and the other investigated configurations is pointed out.

3.2.1. Binder content

Firstly, the influence of the binder content on the mechanical properties of Ti-6Al-4V alloy was investigated. For that a feedstock with a binder system fraction of 35 vol.% instead of the usual 31 vol.% was prepared. Differences in the binder content of the feedstock imply different particle distances prior to sintering resulting in different porosities if sintering time and temperature are kept constant. Therefore, in order to yield approximately the same level of porosity after sintering without prolongation of the process time, the samples were sintered at different maximum temperatures. Two maximum sintering temperatures (1250 °C and 1350 °C) were used for this set of experiments.

One complete S-N curve was measured for the samples with a binder system fraction of 35 vol. % sintered at 1350 °C. Additionally, nine of those samples were sintered at 1250 °C and tested at three different stress levels. This last experiment was carried out in order to evaluate the influence of maximum sinter temperature on the mechanical properties.

In the following the samples fabricated with a binder system fraction of 35 vol. % sintered at 1250 °C and 1350 °C will be referred to as MIM35L and MIM35H, respectively, with “H” corresponding to “high” temperature and “35” is associated to volume fraction of binder.

3.2.2. Particle size

In order to decrease the total amount of remaining porosity samples with a smaller particle size were fabricated. A feedstock with metal powder size below 25 µm and with binder content of 35 vol.% was used. Sintering was performed at 1250 °C for two hours followed by controlled furnace cooling (10 °C/min).

In the following, the samples with a powder size below 25 µm and with 35 vol.% of binder will be referred to as 25MIM35L (25 is referring to powder size, L is related to the “low” sinter temperature and 35 is associated to the binder content).

3.2.3. Boron addition

It is well known that during casting small addition of about 0.1 wt.% of boron to the Ti-6Al-4V alloy decreases the grain size by approximately one order of magnitude [94]. However, it is unclear if during a sintering process such an effect occurs too. Therefore, in order to evaluate possible changes in microstructure of MIM Ti-6Al-4V alloy samples with 0, 0.1 and 0.5 wt.% boron added were sintered at 1250 °C. Moreover, samples with 0 and 0.5 wt.% of boron addition were also sintered at high temperatures of 1400 °C.

Addition of amorphous boron powder was carried out during the mixture of the powders and the binder system (feedstock preparation). The feedstock contained 35 vol.% of binder system. The further process, apart from maximum sintering temperature, was

carried out as described for the MIM31L samples in section 3.2. The maximum sintering temperature of 1400 °C was defined on ground of the dilatometry experiments (see 3.5.3).

3.3. The hot isostatic pressing

The HIP process was applied to fabricate components from Ti-6Al-4V alloy powder without pores.

3.3.1. Powder+HIP

A HIP process was applied on the Ti-6Al-4V alloy powder with particle size < 45 μm (same powder used to fabricated the MIM components) to produce samples for micro-tensile test and for the four-point bending fatigue experiments. The HIP process was carried out at Jülich Forschungszentrum. The powder (1.13 kg) was packed inside a thick-walled titanium can of 50.8 mm diameter and 211 mm length. This container was evacuated during eight hours at room temperature and sealed after six hours at 400 °C. The canned powder was consolidated using the process cycle illustrated in Fig. 16. It is important to note that the process was carried out below the β transus temperature (approximately 1000 °C for the Ti-6Al-4V alloy [95]).

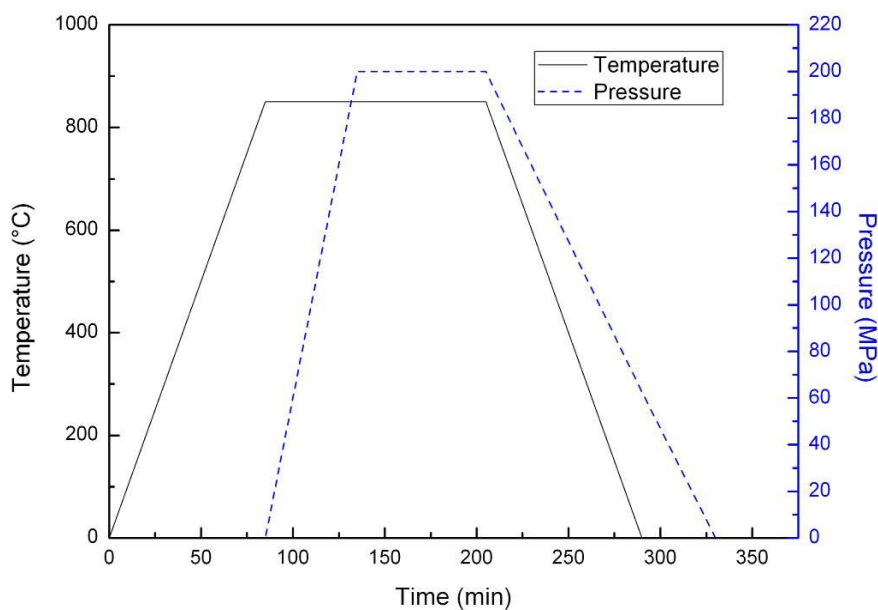


Fig. 16. HIP process cycle.

After the HIP process the impurity levels and the final microstructure were investigated. The samples for micro-tensile and fatigue tests were spark eroded to the final geometry shown in Fig. 14 (fatigue samples) and Fig. 19 (micro-tensile samples). These samples will be referred to as Powder+HIP.

3.3.2. MIM+HIP

In order to obtain specimens fabricated by MIM process with no remaining pores a HIP process was applied on some of the MIM35H samples after sintering. The HIP process was carried out in a shared titanium cycle running at Bodycote HIP N.V., Belgium, with a maximum temperature of 915 °C for two hours at 100 MPa. Microstructural features and impurity levels were evaluated after the HIP process. Tensile and fatigue tests were carried out.

In the following the samples fabricated by MIM and exposed to a HIP process will be referred to as MIM35H+HIP.

3.4. Surface modification and characterisation

Fatigue properties of titanium alloys are largely determined by surface defects [96], microstructures [86], and crystallographic textures [97]. In order to evaluate the influence of surface quality on the fatigue behaviour some of the samples were exposed to shot peening. The shot peening was conducted on an air-blast machine using zirconium oxide particles with a diameter of 500 µm. The air pressure was 4 bar with an exposure time of 10 seconds for each surface sample. The nozzle diameter was 6 mm and the work distance applied was 50 mm.

Light microscopy was used to investigate the influence of shot peening on the surface quality of MIM samples. The surface roughness was estimated by using a Hommel tester T1000.

Four MIM35H samples with shot peening were subjected to a further heat treatment. The samples were heated up to 915 °C for 30 min in vacuum of approximately 10^{-5} mbar. The furnace used was the same applied for the sintering process. After the heat treatment the samples were exposed to fatigue loading under four-point bending

configuration. This experiment was carried out in order to relieve possible compressive stresses in the surface. Furthermore, if the samples after the shot peening application contain a higher degree of local plastic deformation it might be possible to do a recrystallization of the microstructure (finer microstructure at the deformed regions). The microstructure at the surface and the fatigue fracture surfaces were investigated by using light microscopy and SEM.

3.5. Characterization of the samples

3.5.1. Impurity levels, microstructural features and relative density

The impurity levels such as oxygen, nitrogen and carbon of the specimens were determined using a conventional LECO melt extraction system. The TC – 436AR equipment was used to analyse the nitrogen and oxygen levels. The CS – 444 was applied in order to determine the carbon content. In an attempt to evaluate the influence of these elements on the mechanical properties of samples processed with different parameters, the concept of oxygen equivalent $O_{(eq.)}$ introduced in section 2.1. was applied. It is important to note that at least three samples were examined for each different sintering furnace run (batch). Consequently, the impurity level values presented for this investigation are average from these samples.

The microstructure of the samples was examined by optical microscopy after polishing and etching in Kroll's reagent (containing 3% HF and 10% HNO₃). The average grain size was measured using an image analysis system (Olympus Soft Image Solution, analysis pro). A linear intercept technique (ASTM E112-96) was applied in order to determine the grain size. For this investigation, the grain size was assumed to be the microstructural feature that defines the slip length. Therefore, the α colony size (Fig. 17, length a)) and the α phase (Fig. 18, length a)) or α colony (Fig. 18, length b)) sizes are the features that define a grain for lamellar and quasi equiaxed microstructures, respectively.

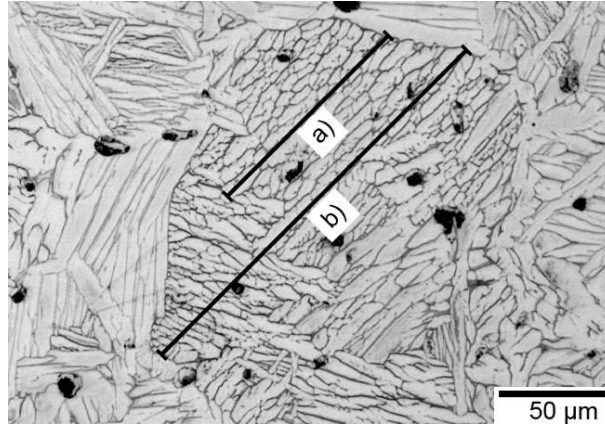


Fig. 17. Typical MIM lamellar microstructure; a) α colony size; b) β grain size.

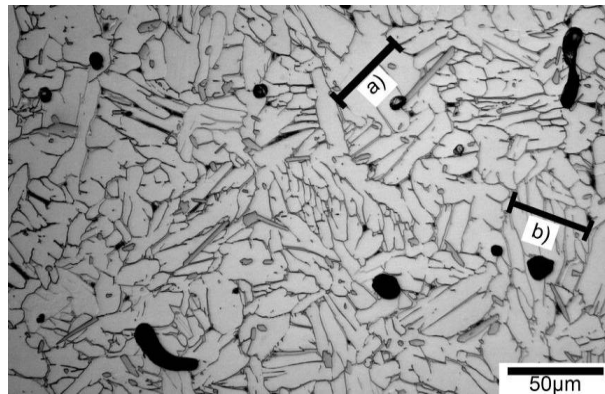


Fig. 18. Quasi-equiaxed microstructure; a) α grain size, b) α colony size.

The relative densities of green (after injection) and sintered samples were determined by the immersion method outlined in ASTM B311. The bulk density of the Ti-6Al-4V alloy component without pores was determined to be 4.41 g/cm^3 after measuring a sample exposed to an additional HIP process following the MIM production. Therefore, it was possible to estimate the porosity of the sintered samples by using:

$$\text{Porosity [\%]} = 100 - \left[\left(\frac{\rho_0}{\rho_B} \right) \cdot 100 \right] \quad . 1$$

Where ρ_0 is the apparent sintered or the apparent green density measured by immersion method and ρ_B is the apparent bulk density of Ti-6Al-4V alloy component without pores.

3.5.2. EBSD measurements

Electron backscatter diffraction (EBSD) was performed using hardware fabricated by ZEISS, GEMINI (ULTRA™ 55) and TSL OIM Analysis 5.2 software. Spatially resolved EBSD maps were acquired at 15 keV using a step size of 0.2 μm . The samples were prepared by conventional polishing procedures followed by a final polishing (5 min.) with a Struers oxide polish suspension (OPS) compound. When electropolishing $\alpha + \beta$ titanium alloys the β phase is attacked preferentially. This makes it impossible to detect the β phase and its texture during the EBSD mapping. For this reason, the samples were finally polished in a vibration machine (Buehler Vibromet 2) during 48 hours in colloidal silica polishing suspension (MasterMet® 0.06 μm).

Electron backscattered diffraction Kikuchi patterns (EBSPs) were used to help clarify the borides' structure. The lattice parameters and the fractional coordinates of atoms in TiB and TiB₂ are given in Table 1. These data made it possible to distinguish local crystallographic differences by means of EBSD patterns.

Table 1 – Crystal structure, lattice parameters, and fractional coordinates in TiB and TiB₂.

Phase	Structure/space group	Unit cell [10^{-10} m]	Atomic positions
TiB	Orthorhombic/Pnma	a = 6.12 b = 3.06 c = 4.56	Ti: 4c, m, x = 0.1777, y = 1/4, z = 0.123 B: 4c, m, x = 0.029, y = 1/4, z = 0.603
TiB ₂	Hexagonal/P6/mmm	a = 3.03 c = 3.23	Ti: 1a, $\bar{6}$ /mmm, x = 0, y = 0, z = 0 B: 2d, $\bar{6}$ m2, x = 1/3, y = 2/3, z = 1/2

3.5.3. Dilatometry

The influence of the boron addition on the sintering behaviour of the Ti-6Al-4V alloy was investigated by dilatometry. The maximum sintering temperature applied to the fabrication of the Ti-6Al-4V-0.5B alloy specimens was chosen based on the dilatometry results. For this experiment, the MIM samples made from Ti-6Al-4V and Ti-6Al-4V-

0.5B were chemically and thermally debinded followed by pre-sintering at 700 °C for 1 hour. The diameter of the samples was approximately 5 mm with a length of 10 mm. The dilatometer used was a vertical configuration dilatometer fabricated by LINSEIS (L70/2171). A heating rate of 10 °C/min and an isotherm of 1400 °C for two hours were used. Argon atmosphere was applied during the heating and cooling processes of the dilatometry experiments.

3.5.4. Tensile test

Fig. 15 illustrates the geometry used for the tensile experiments. Micro-tensile specimens (Fig. 19) were also used. The difference of specimen geometry is due to the fact that for some configuration, such as Powder+HIP samples, the amount of material was not enough to fabricate specimens with the required dimensions (Fig. 15). Therefore, in order to compare the results obtained for the micro-tensile specimens with the dog-bone specimens, both micro-tensile and dog-bone specimens were fabricated for the MIM35H samples. Tensile tests were performed on a servohydraulic structural test machine equipped with a 100 kN load cell. The tensile tests were carried out at room temperature at a strain rate of $1.2 \times 10^{-5} \text{ s}^{-1}$. At least three dog-bone specimens and five micro-tensile samples were tested for each investigated configuration.

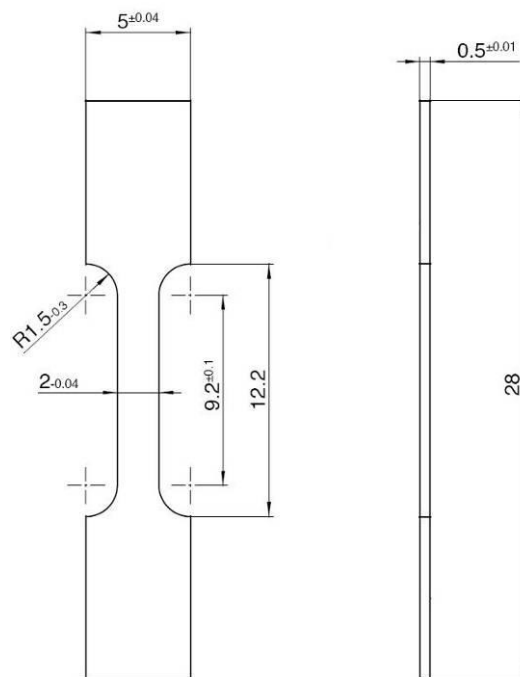


Fig. 19. Micro-tensile specimen geometry. Dimensions are in millimetres.

3.5.5. Fatigue experiments

High cycle fatigue testing was done in four-point bending configuration using a resonance machine fabricated by RUMUL (Mikrotron 654-H, 20kN). Tests were conducted under load control with a cyclic frequency of ~95 Hz (sine wave) at a load ratio $R=\sigma_{\min}/\sigma_{\max}$ of 0.2. All the experiments were carried out at room temperature in air. The fatigue endurance limit was defined as 10^7 cycles. The geometry used for the high cycle four-point bending fatigue test is shown in Fig. 14.

The maximum initial tensile stress σ within the loaded bar was calculated using equation 2 where F is the applied force, L is the gauge length, W is the bar thickness and $(I_{xx})_r$ is the moment of inertia of rectangular cross section with corner radius r.

$$\sigma = \frac{FLW}{24(I_{xx})_r} \quad .2$$

The true moment of inertia $(I_{xx})_r$ about the neutral axis x-x is:

$$(I_{xx})_r = \frac{B(W - 2r)^3}{12} + \frac{(B - 2r)r^3}{6} + (1/2)(B - 2r)(W - r)^2r + 4r^4\left(\frac{\pi}{16} - \frac{4}{9\pi}\right) + \pi r^2\left[\frac{W}{2} - r\left(1 - \frac{4}{3\pi}\right)\right]^2 \quad .3$$

where B is the bar width and r is the corner radius.

The fracture surfaces of broken specimens were analyzed by a stereoscope (LEICA MZ95) in order to identify the crack initiation location. The microstructure and fracture surface of the samples were investigated using a scanning electron microscope (ZEISS – DSM962). The observations were focused upon the crack initiation location. In addition, the chemical composition of selected regions was investigated by using scanning electron microscopy (SEM) coupled with energy dispersive X-ray spectroscopy (EDX).

In an effort to better understand the influence of the microstructural features on the fatigue crack nucleation and propagation, crack front profiles at the possible crack nucleation site were investigated for samples with and without boron addition.

4. Verification of the four-point bending fatigue tests

Usually, the high cycle fatigue tests are performed in a constant amplitude axial fatigue test machine following the ASTM standard (E466). According to this standard to ensure test section failure, the grip cross-sectional area should be at least four times the test section area. However, the manufacture of such component by MIM technique is complicated due to problems related to sample integrity after injection and sinter processes. Therefore, in this work as a first step on the investigation of fatigue behaviour of Ti-6Al-4V components fabricated by MIM technique, the high cycle fatigue tests were performed in a four-point bending configuration. Bending fatigue test requires a simple geometry, which can be easily processed by MIM technology.

4.1. Experimental procedure

A hot rolled and annealed commercial Ti-6Al-4V ELI (ASTM grade 23) alloy cylinder with a diameter of 55 mm and a length of 250 mm supplied by Enpar, Germany was used to fabricate the specimens for the verification of the fatigue experiments. The samples were machined in the rolled direction to the final geometry shown in Fig. 14 via electric discharge machining. In order to minimize the influence of surface difference on the fatigue behaviour, the samples were exposed to shot peening. The shot peening was conducted on an air-blast machine and the same parameters used for the MIM samples were also applied here. In the following, these samples will be referred to as reference material.

The fatigue tests were performed with the same parameters applied for MIM samples, as described in 3.5.5.

4.2. Results and discussion

The reference material exhibited an equiaxed microstructure, as illustrated in Fig. 20, with an average α grain size of approximately 5 μm .

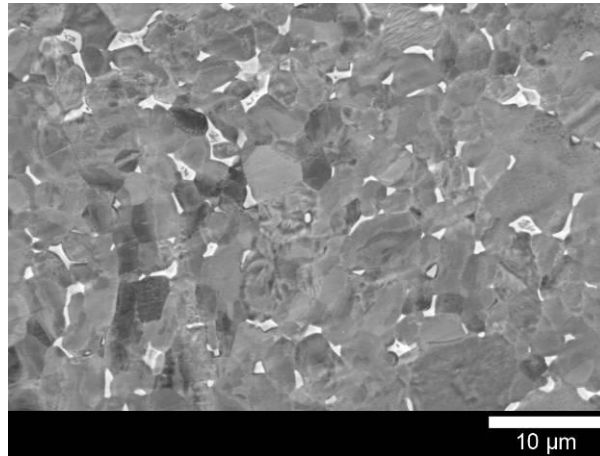


Fig. 20. BSE image of the reference material microstructure (equiaxed microstructure).

The result of high cycle four-point bending fatigue tests for the reference material is shown in Fig. 21. For all S-N curves demonstrated in this investigation the numbers between parentheses indicate the amount of samples that survived at a specific stress level (run out).

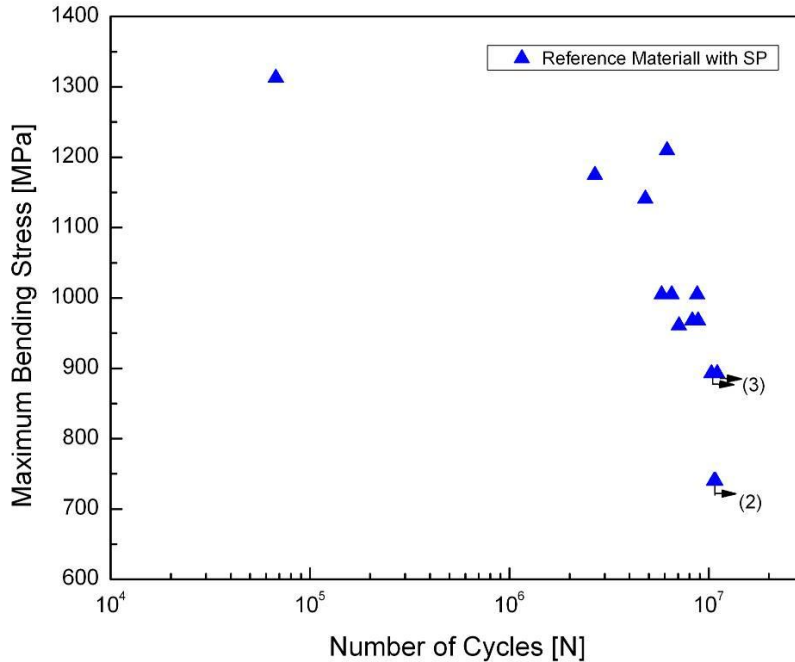


Fig. 21. S-N curve for reference materials samples with shot peening (SP).

The reference samples with shot peening demonstrated a fatigue endurance limit of approximately 890 MPa. Unfortunately, it is not possible to compare directly this result with literature values due to the lack of data related to high cycle four-point bending fatigue test of Ti-6Al-4V alloy. Akahori et al. [10] carried out high cycle axial fatigue test with $R=0.1$ and found a value of 800 MPa for fatigue endurance limit of Ti-6Al-4V alloy with equiaxed microstructure. This lower literature value of fatigue endurance limit compared to our reference material is expected. Morrissey et al. [98] described the influence of stress ratio R on mean and amplitude stresses for Ti-6Al-4V alloy at fatigue life of 10^7 cycles. Increasing of R leads to a decrease of stress amplitude and an increase of mean stress. Therefore, it is expected that tests with higher R values cause greater values for maximum stress. Moreover, it should be pointed out that the shot peening promoted an increase in the fatigue strength which could be an additional reason for the higher fatigue endurance limit observed for our reference material compared to literature values. Thus, it is possible to assume that the results demonstrated in this work are in an acceptable range with literature data.

5. Results

5.1. The MIM31L samples

The MIM31L sintered samples presented a fully lamellar microstructure, as illustrated in Fig. 22. The α colony size, alternating α and β with distinct orientation relationship, was approximately 100 μm . The apparent densification was 96.6 % (3.4 vol.% of remaining porosity).

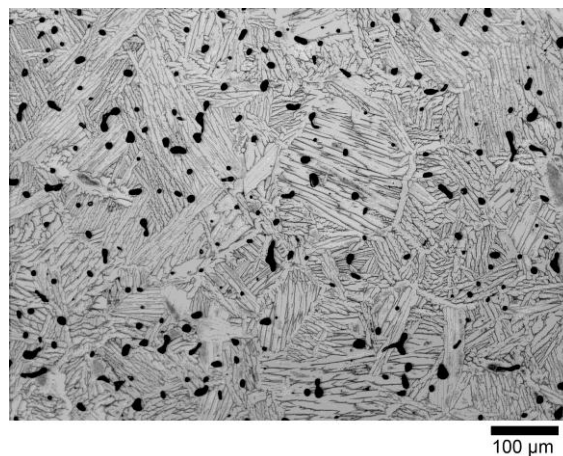


Fig. 22. Microstructure of MIM Ti-6Al-4V with 31 vol.% of binder and sintered at 1250 °C for two hours (MIM31L).

The porosity was near-circle shape with diameter size of approximately 9 μm . The pore size distribution and the cumulative probability are illustrated in Fig. 23. The maximum pore diameter measured was 33 μm (almost 300 pores were evaluated for this configuration).

The oxygen, carbon, nitrogen and the oxygen equivalent contents of the applied powder, sintered MIM31L samples and the Ti-6Al-4V ELI alloy (ASTM grade 23) are given in Table 2. An expected increase of impurity levels due to the MIM process was observed.

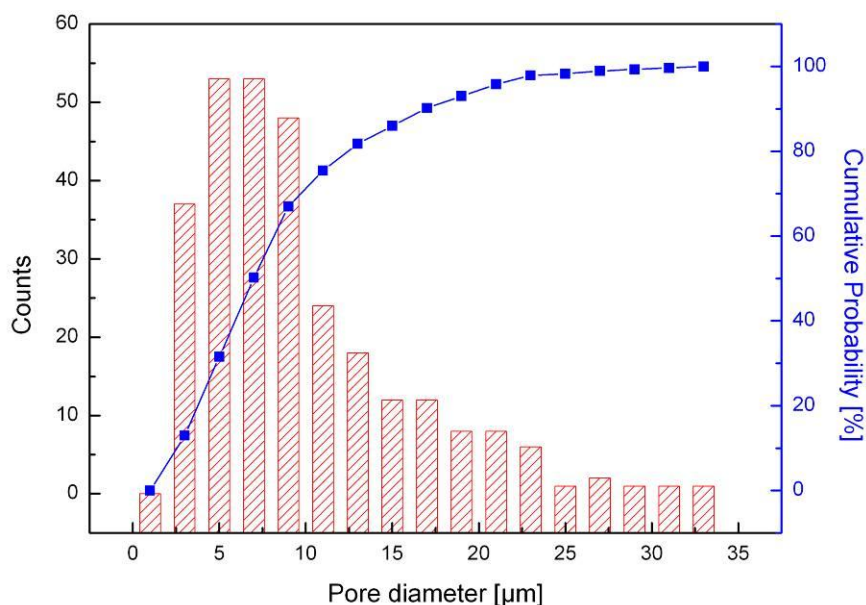


Fig. 23. Pore diameter distribution and cumulative probability for MIM31L samples.

Although the MIM31L and MIM31L* samples were fabricated with the same process parameters, a difference of approximately 250 $\mu\text{g/g}$ in terms of oxygen equivalent was observed.

Table 2. Chemical concentration of interstitial alloying element.

Material	O [$\mu\text{g/g}$]	C [$\mu\text{g/g}$]	N [$\mu\text{g/g}$]	Oxygen Equivalent [$\mu\text{g/g}$]
Ti-6Al-4V ELI powder	1000	200	100	1350
MIM31L	1900 \pm 90	450 \pm 20	180 \pm 15	2598 \pm 135
MIM31L*	2128 \pm 119	370 \pm 39	222 \pm 58	2850 \pm 264
Ti-6Al-4V ELI	1300	800	300	2500

*typical variation of impurity levels of the MIM samples

5.1.1. Tensile mechanical behaviour

The tensile properties of the MIM31L samples are summarized in Table 3. Samples fabricated by MIM technique exhibited lower strength compared to ASTM B 348-02 for Ti-6Al-4V ELI values. However, the elongation of the MIM31L samples was higher

than the minimal values accepted for this alloy. It is important to note that the interstitial elements concentration for the MIM31L samples (Table 2) was higher than the accepted concentrations of Ti-6Al-4V ELI as described in ASTM B348-02.

Table 3. Tensile properties of the Ti-6Al-4V ELI (ASTM Grade 23) and the MIM31L samples.

Material	σ_y [MPa]	UTS [MPa]	Elongation [%]
Ti-6Al-4V ELI	Min. 759	Min. 828	Min. 10
MIM31L	700 ± 5	800 ± 1	15.1 ± 1
MIM31L*	703 ± 3	806 ± 3	13.7 ± 1

The difference of approximately 250 $\mu\text{g/g}$ in oxygen equivalent between MIM31L and MIM31L* samples was not enough to significantly affect the mechanical properties. Fig. 24 illustrates a typical tensile fracture surface of the MIM31L samples. A relatively coarse dimpled structure with remaining porosity is observed.

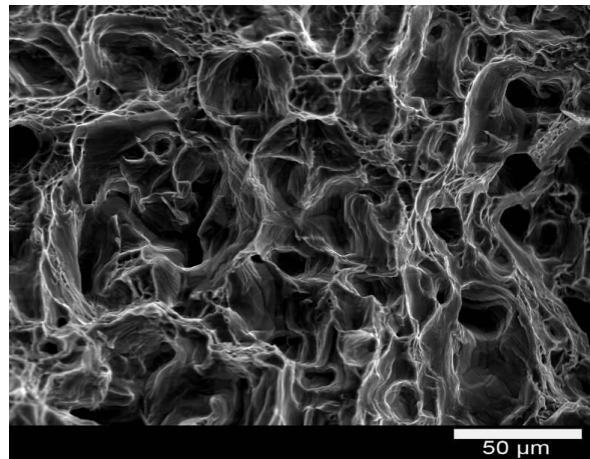


Fig. 24. Typical tensile fracture surface of MIM31L samples. Pores and dimples are visible.

5.1.2. Fatigue behaviour

The four-point bending fatigue behaviour of MIM31L samples is shown in Fig. 25. It is important to note that the data points shown are composed from measurements on both MIM31L and MIM31L* samples.

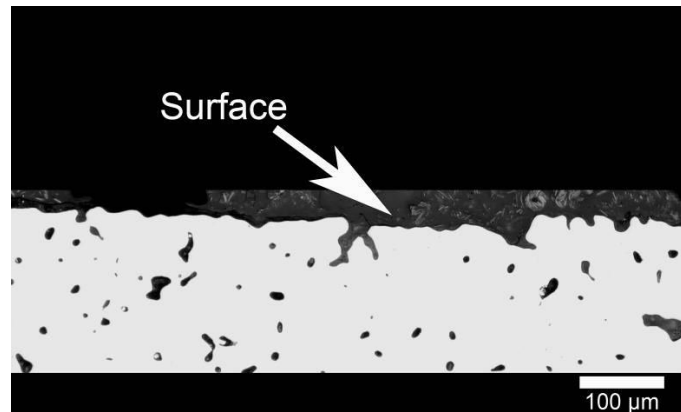


Fig. 26. Surface quality of MIM31L samples.

The fracture surfaces of broken fatigue specimens were investigated. Fig. 27 illustrated a typical fracture surface, indicating that the fatigue crack nucleation started at the surface.

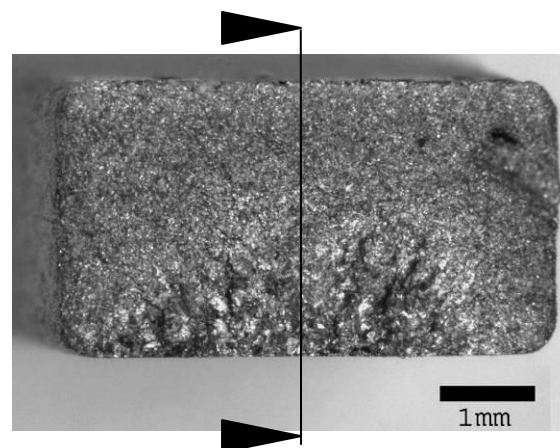


Fig. 27. Typical fracture surface of MIM31L samples. The black line indicates the position where the crack front profile (Fig. 29) was evaluated.

The white arrow in Fig. 28a indicated the surface exposed to tensile stress during four-point bending fatigue test. The white arrow in Fig. 28b appoints for the assumed crack initiation location. Two distinct regions are visible: one region shows a normal fracture surface, where it is possible to identify lamellae boundaries (area 1). The other region illustrates the original powder surface (area 2), which demonstrates that in this region the particles were not connected.

This disconnection of the particles resembles a notch located at surface sample, as illustrated by Fig. 26. It is important to note that all investigated fracture surfaces of the

MIM31L samples presented at the assumed crack nucleation site the presence of notches as illustrated in Fig. 28b. The maximum observed size of the notches located at the samples surface was approximately 100 μm . Apparently, these defects are randomly distributed over the sample surface. Furthermore, note that apart from the notches at the surface, typical microstructural features presented at the assumed crack initiation region were facets and pores as illustrated in Fig. 28b in the region 1.

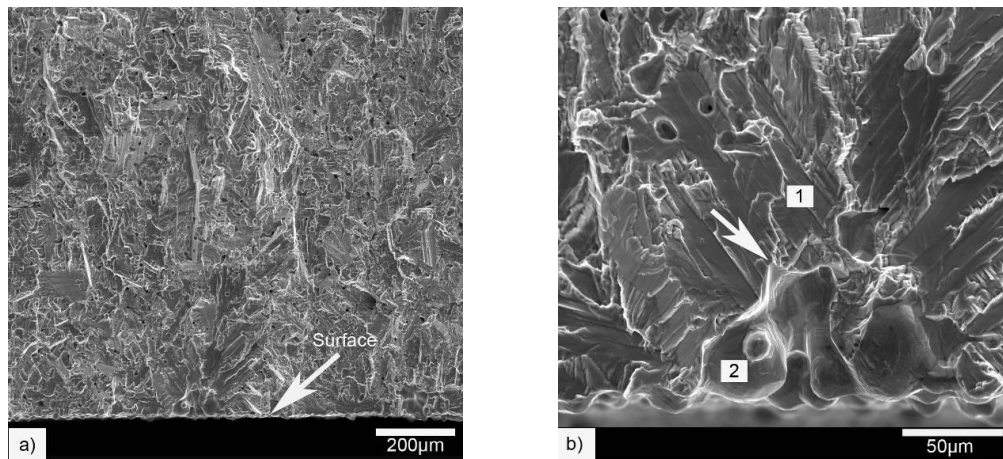


Fig. 28. Typical fracture surface of MIM31L samples: (a) lower magnification and (b) higher magnification of the assumed crack initiation location.

In order to understand the interaction between microstructural features and the crack nucleation and propagation, crack front profiles at the possible crack nucleation site were investigated. The black line in Fig. 27 illustrates the region where the crack front profile (Fig. 29) was evaluated. The right side of Fig. 29 represents the lower middle side of Fig. 27, which is assumed to be the crack initiation location.

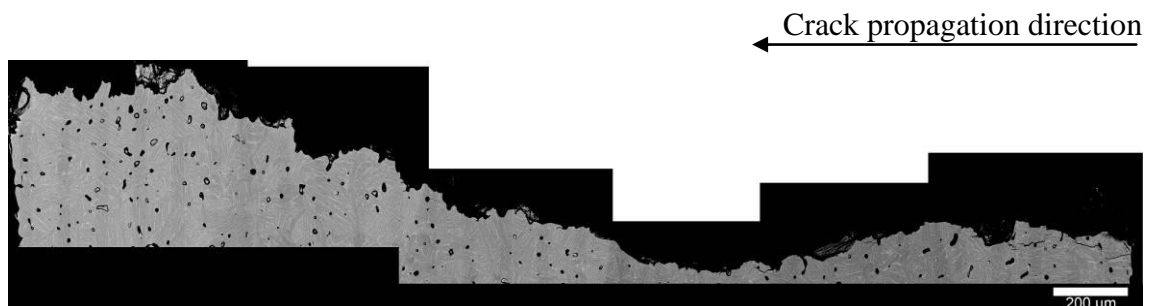


Fig. 29. Typical crack front profile of MIM31L samples.

Secondary cracks and micro cracks deflections were observed on the assumed crack nucleation side as illustrated in Fig. 30a. Furthermore, the black arrow in Fig. 30b points to a region with a different surface morphology. This particle surface morphology located directly on the sample surface resembles again the existence of the surface defects as illustrated in Fig. 26 or in Fig. 28b.

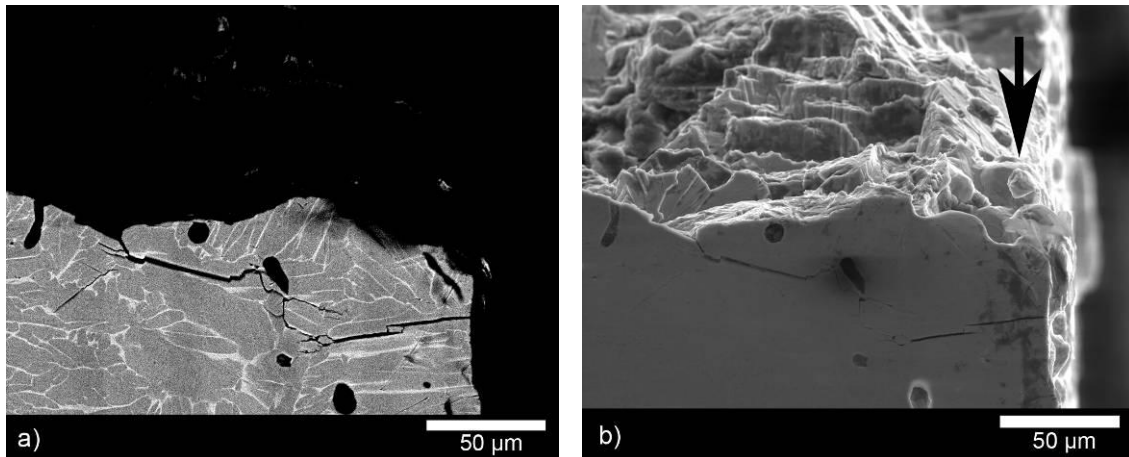


Fig. 30. Higher magnification of the crack front profile at crack nucleation site: (a) BSE image, (b) SE image.

5.2. Binder content

5.2.1. Microstructural features

Table 4 shows the microstructural features and chemical composition of MIM31L, MIM31L*, MIM35L and MIM35H samples. The results referent to interstitial impurity elements for MIM31L and MIM31L* were illustrated already in Table 2. The MIM35L samples presented the highest porosity value of approximately 6 %. Moreover, it is important to note that the MIM35H samples and the MIM31L samples showed approximately the same amount of porosity. No significant difference in the level of impurities was observed among the three different configurations. E.g. the variation of the oxygen content was between 1900 $\mu\text{g/g}$ and 2300 $\mu\text{g/g}$. The same trend is observed for $O_{(\text{eq})}$.

Table 4. Microstructural features of samples sintered at a maximum temperature of 1250 °C and 1350 °C with different binder content.

Microstructural Features	MIM31L	MIM31L*	MIM35H	MIM35L
Green density [g/cm ³]	3.31	3.31	3.2	3.2
Sinter density [g/cm ³]	4.26	4.26	4.25	4.16
Porosity [%]	3.4	3.4	3.6	5.7
α colony size [μm]	97 \pm 9	100 \pm 11	148 \pm 20	77 \pm 10
Average C content [$\mu\text{g/g}$]	450 \pm 20	370 \pm 39	409 \pm 23	422 \pm 23
Average N content [$\mu\text{g/g}$]	180 \pm 15	222 \pm 58	172 \pm 24	190 \pm 19
Average O content [$\mu\text{g/g}$]	1900 \pm 90	2128 \pm 119	2318 \pm 44	2066 \pm 35
O _(eq.) [$\mu\text{g/g}$]	2598 \pm 135	2850 \pm 264	2969 \pm 109	2763 \pm 90

The increase of sintering temperature promoted an increase in α colony size. In addition, contrary to the MIM31L (Fig. 22) and MIM35L samples (Fig. 31), a well defined continuous α layer at β grain boundaries is observed in the MIM35H samples (Fig. 32).

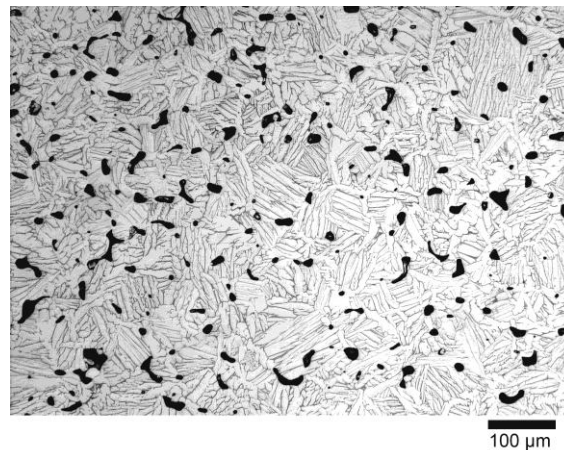


Fig. 31. Microstructure of MIM Ti-6Al-4V with 35 vol.% of binder and sintered at 1250 °C (MIM35L).

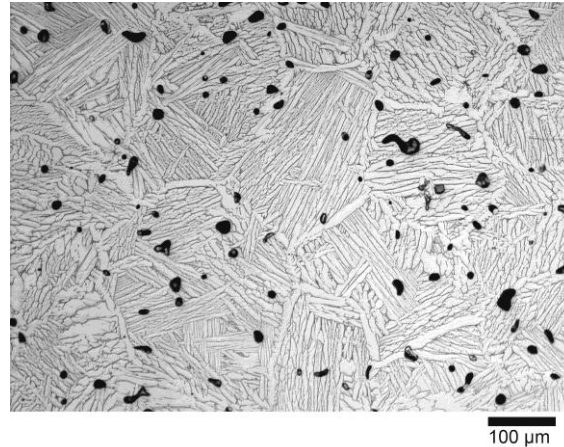


Fig. 32. Microstructure of MIM Ti-6Al-4V with 35 vol.% of binder and sintered at 1350 °C (MIM35H).

Fig. 33 and Fig. 34 depict a typical pore diameter distribution for the MIM35L and MIM35H samples, respectively. The average pore diameter for MIM35L was approximately 14 μm with a maximum value of 86 μm (1530 pores were analysed). The MIM35H samples exhibited a maximum observed pore size of 46 μm and an average of approximately 12 μm (510 pores were analysed).

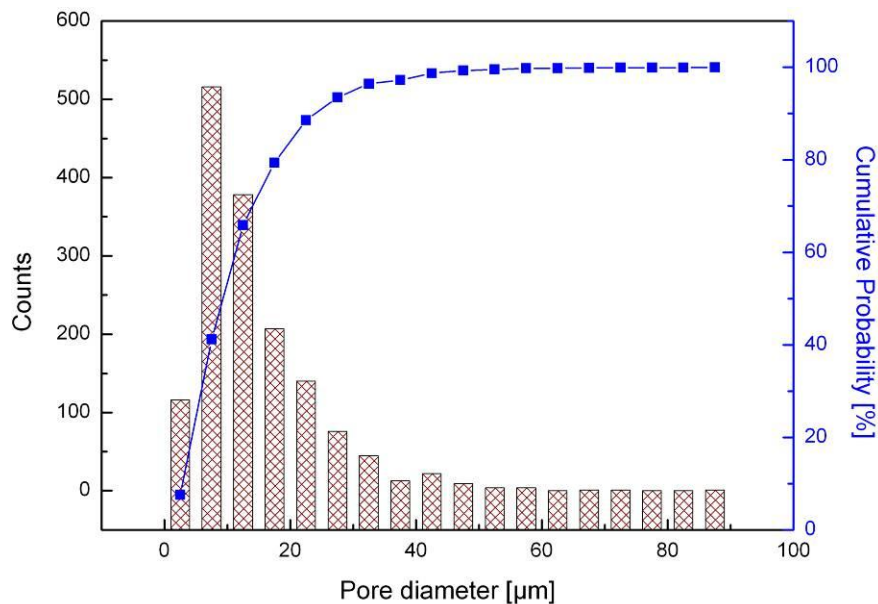


Fig. 33. Pore diameter distribution and cumulative probability for MIM35L samples.

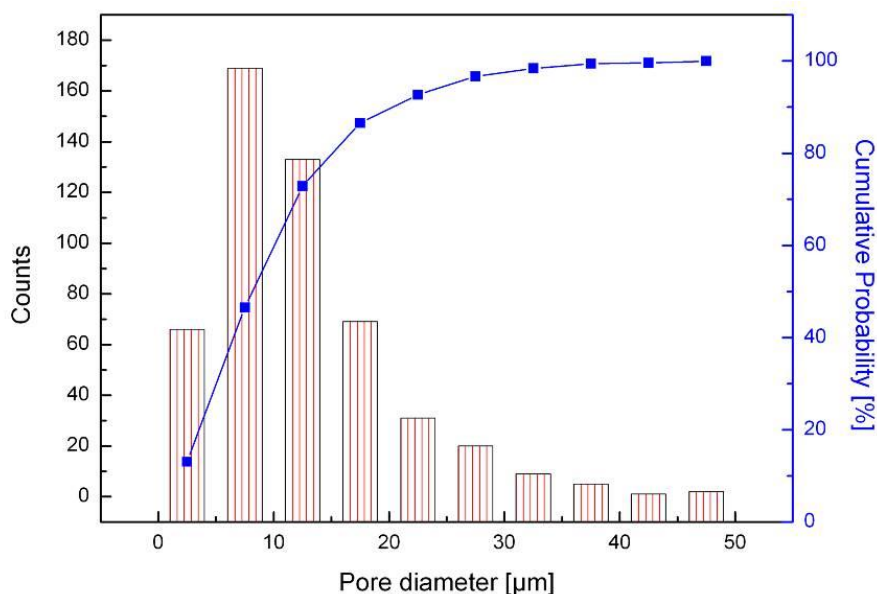


Fig. 34. Pore diameter distribution and cumulative probability for MIM35H samples.

5.2.2. Tensile properties

The tensile properties of the MIM31L, MIM31L*, MIM35L and MIM35H samples are summarized in Table 5.

Table 5. Tensile property and fracture surface analysis.

Tensile property	MIM31L	MIM31L*	MIM35L	MIM35H
Yield Stress [MPa]	700 ± 5	703 ± 3	680 ± 2	720 ± 2
Maximum Stress [MPa]	800 ± 1	806 ± 3	784 ± 0.8	824 ± 4
Elongation [%]	15.1 ± 1	13.7 ± 1	10.8 ± 0.3	13.4 ± 0.7

The results presented in Table 3 for MIM31L and MIM31L* samples are illustrated again in Table 5, in order to compare the mechanical properties with the MIM35L and MIM35H samples. As illustrated in Table 5 the samples with higher amount of porosity (MIM35L) exhibited the poorest tensile properties. However, the elongation values for all four configurations are above the minimal value accepted for wrought Ti-6Al-4V ELI alloy (ASTM Grade 23).

The typical tensile fracture surfaces of MIM35L and MIM35H samples are shown in Fig. 35 and Fig. 36 , respectively. A dimpled structure with remaining porosity is observed.

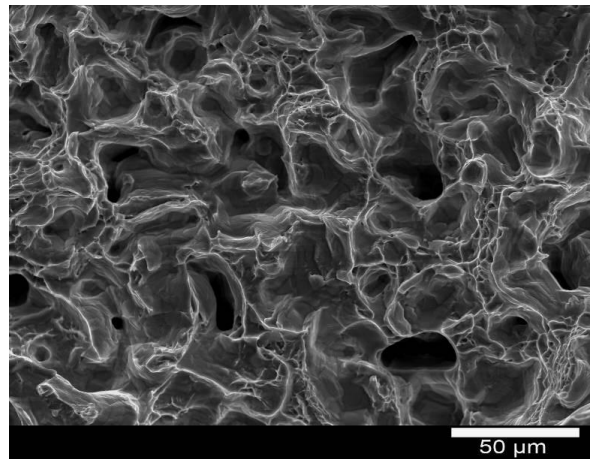


Fig. 35. Typical tensile fracture surface of MIM35L samples. Pores and dimples are visible.

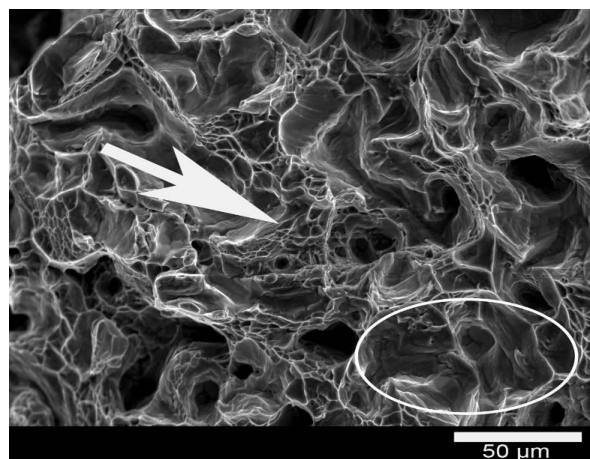


Fig. 36. Typical tensile fracture surface of MIM35H samples. Pores and dimples are visible.

Two distinct regions are presented on the tensile fracture surface of the MIM35H samples. The white arrow on Fig. 36 points to a fine dimpled structure, here called “fine dimples”. In the other region, indicated by the white ellipse on Fig. 36, it was possible to observe a coarser dimpled structure with remaining porosity. Apparently the amount of fine dimpled structures increases with a subsequent improvement of the sintering temperature.

5.2.3. Fatigue behaviour

The results of high cycle four-point bending fatigue tests for the three configurations, MIM31L, MIM35L and MIM35H are shown in Fig. 37. The MIM35H samples demonstrate a superior endurance limit compared with MIM31L samples. Surprisingly, the MIM35L samples apparently achieved a fatigue behaviour similar to that of the MIM35H samples.

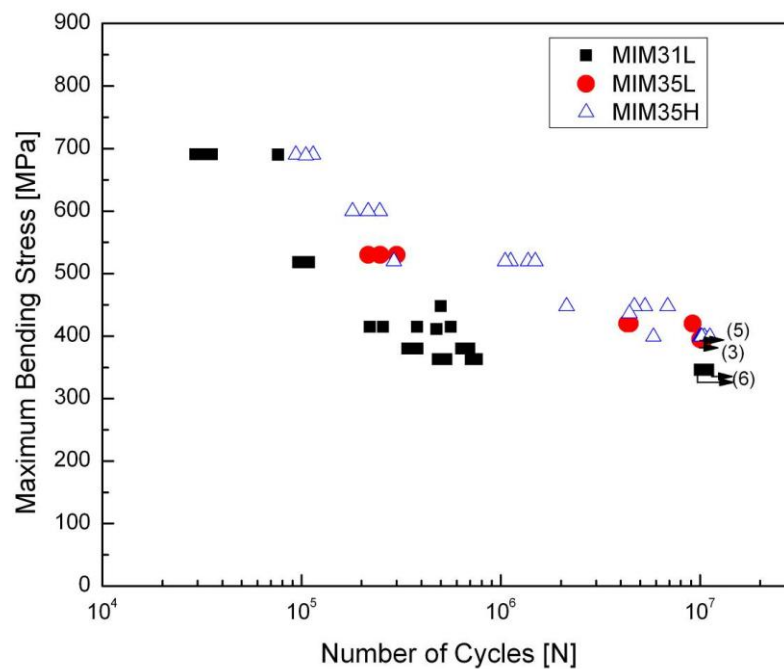


Fig. 37. S-N curves for MIM31L, MIM35L and MIM35H samples.

Compared to MIM31L (Fig. 26) the surface quality of MIM35H samples (Fig. 38) and MIM35L samples (Fig. 39) appears to be different in terms of surface roughness. It is interesting to note that however the roughness measurement revealed no significant difference on the R_a values for MIM31L ($R_a=1.95 \mu\text{m}$) and MIM35H ($R_a=2.08 \mu\text{m}$). Apparently, the surface quality of MIM35L samples is similar to that of MIM35H samples.

Fractography of fatigued specimens revealed the possible region for the crack nucleation of MIM35L (Fig. 40) and MIM35H (Fig. 41). The maximum observed size of the notches located at the surface of the samples was approximately $50 \mu\text{m}$ for both configurations.

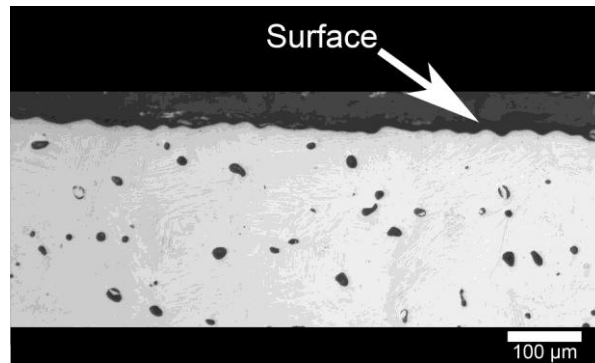


Fig. 38. Surface quality of the MIM35H samples.

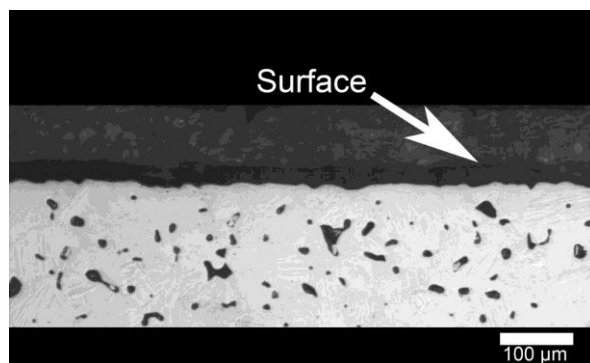


Fig. 39. Surface quality of the MIM35L samples.

It was possible to identify in Fig. 40 and Fig. 41 the presence of facets regions. Such a microstructural feature at the assumed crack initiation region was also observed for the MIM31L samples (Fig. 28b). However, the size of the facets for the MIM35H samples was apparently bigger than the MIM35L samples.

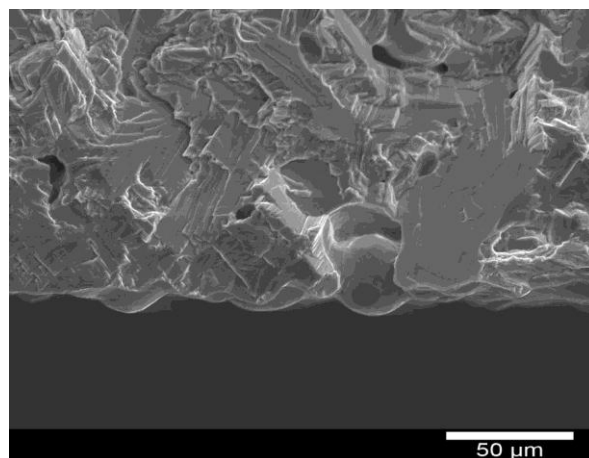


Fig. 40. Typical fracture surface of MIM35L samples. Possible crack nucleation region.

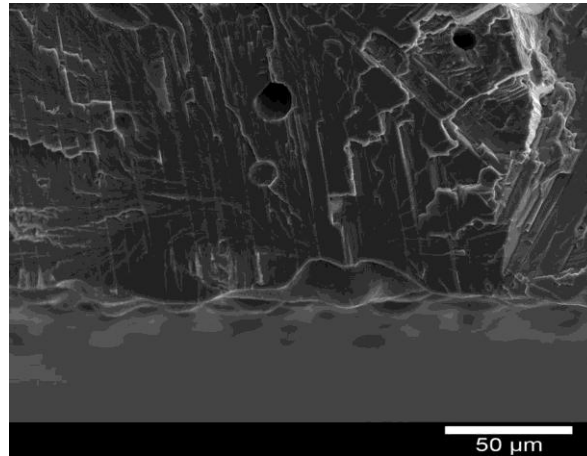


Fig. 41. Typical fracture surface of MIM35H samples. Possible crack nucleation region.

5.3. Shot peening as a surface treatment

High cycle fatigue properties of engineering materials can be enhanced by surface treatment. Shot peening is by far the most common and the least costly surface treatment technique employed [11]. The benefits of shot peening are related to the surface work hardening and the development of subsurface compressive residual stresses [11, 99, 100]. Therefore, in order to evaluate the fatigue behaviour of MIM samples with a different surface quality without change others relevant parameters such as porosity or grain size the MIM31L and the MIM35H samples were exposed to a shot peening process (for details see 3.4).

5.3.1. Fatigue behaviour

Fig. 42 and Fig. 43 illustrate the fatigue behaviour of MIM Ti-6Al-4V alloy components with and without shot peening. The MIM31L samples with shot peening showed a significant higher endurance limit (450 MPa) than those without shot peening (Fig. 42). The same trend was observed for the MIM35H samples, where shot peening enhanced the endurance limit by approximately 50 MPa (Fig. 43). However, the absolute enhancement seems somewhat lower.

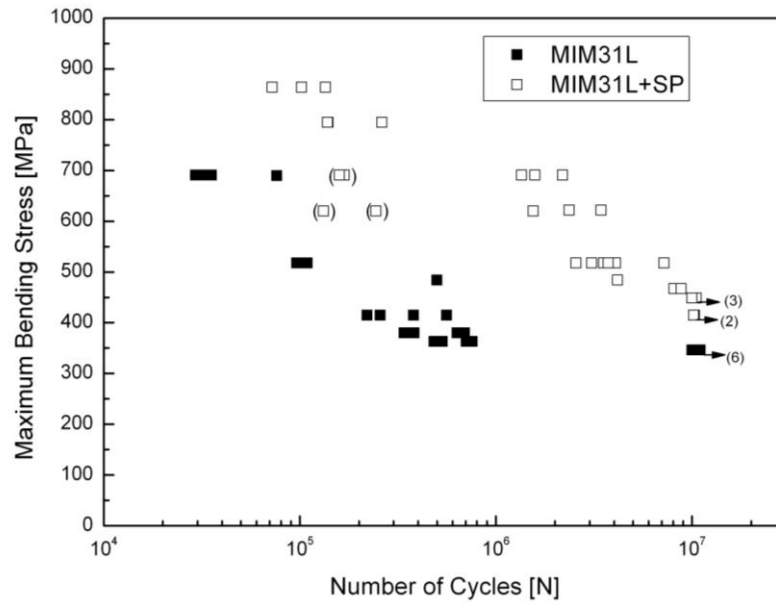


Fig. 42. S-N curves for MIM31L samples with and without shot peening (SP).

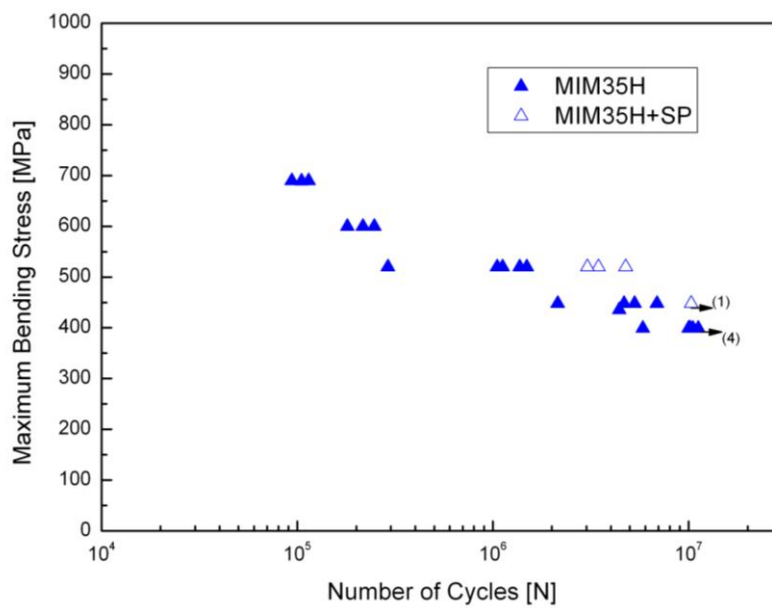


Fig. 43. S-N curves for MIM35H samples with and without shot peening (SP).

A typical cross section of the MIM31L samples after the shot peening application is illustrated in Fig. 44. The MIM35H samples with shot peening (Fig. 45) showed the same surface morphology as the MIM31L samples with shot peening.

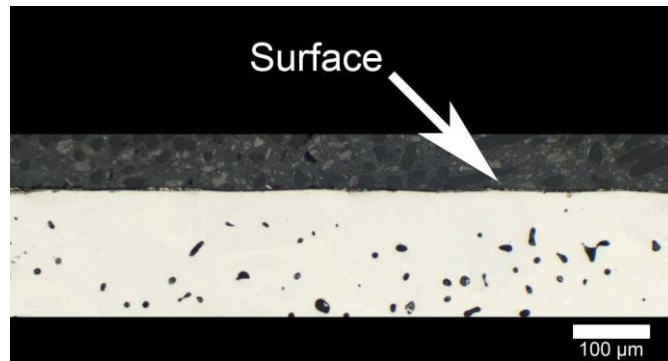


Fig. 44. Surface quality of the MIM31L samples with shot peening.

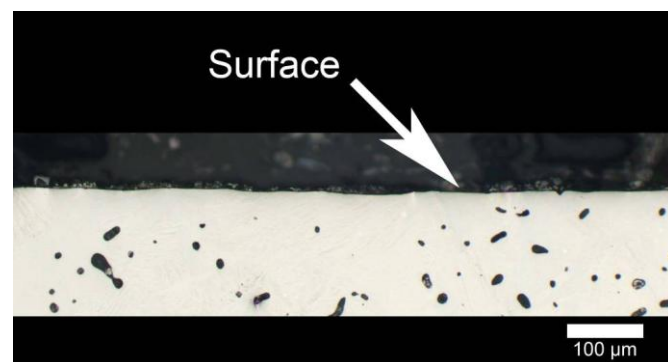


Fig. 45. Surface quality of the MIM35H samples with shot peening.

The possible crack nucleation site was also investigated on the fatigue fracture surface of the MIM31L and MIM35H samples with shot peening. Since MIM31L and MIM35H samples with shot peening presented approximately the same fracture surface morphology, only MIM31L fracture surface is presented in the following Figs. 46 to 50. The shape of rough region in Fig. 46 indicates that the crack initiation location was in some place near to the lower left corner. Scanning electron micrographs of a typical fracture surface of the MIM31L samples with shot peening are shown in Fig. 47.

The white arrows in Fig. 47a and Fig. 47b indicate the surface under tensile stress during testing and the crack initiation location, respectively. Note that for all samples the crack initiated at a location inside the samples instead of the surface, except for the samples marked with parenthesis in Fig. 42. For these samples the crack initiated at the surface as illustrated in Fig. 48.

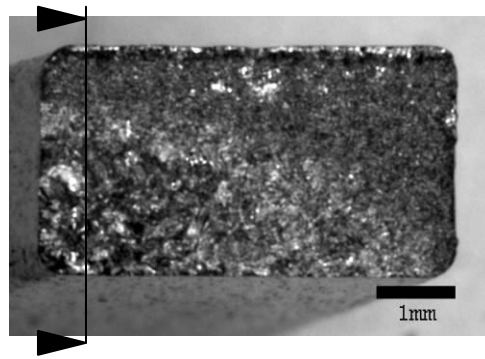


Fig. 46. Typical fracture surface of MIM31L samples. The black line indicates the position where the crack front profile (Fig. 49) was evaluated.

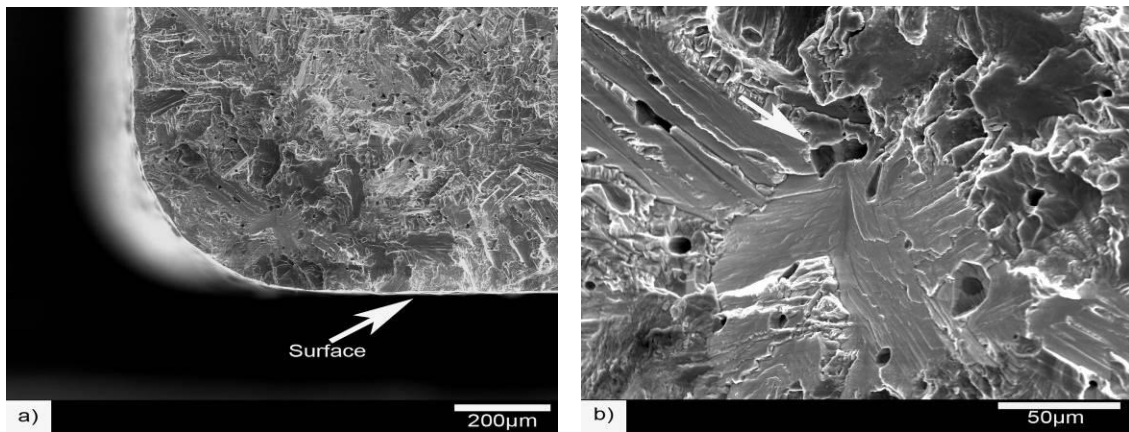


Fig. 47. Typical fracture surface of MIM31L samples with shot peening: (a) lower magnification and (b) higher magnification of crack initiation location.

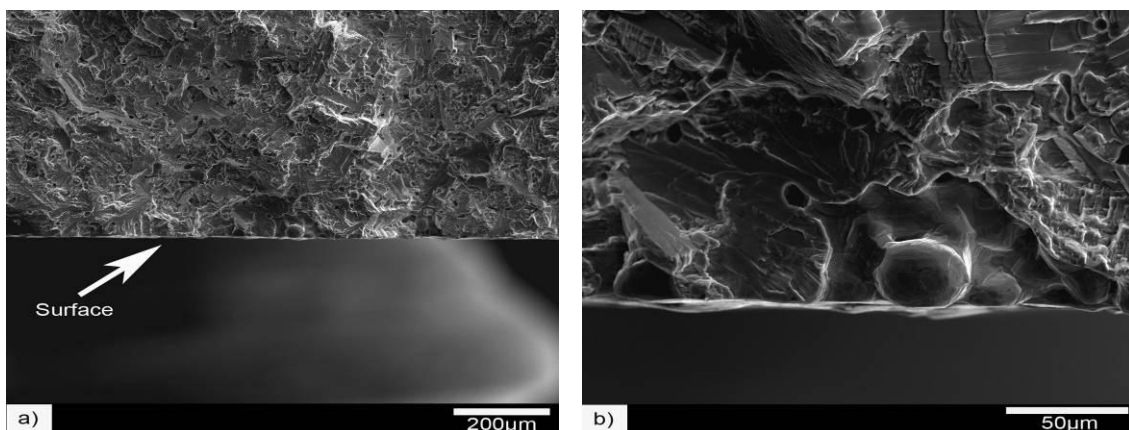


Fig. 48. Typical fracture surface of MIM31L samples (Fig. 42 with parentheses) with shot peening and (a) lower magnification (b) higher magnification of crack initiation location.

Accordingly to the samples without shot peening (Fig. 27), the black line in Fig. 46 demonstrates schematically the position where the crack front profile was evaluated.

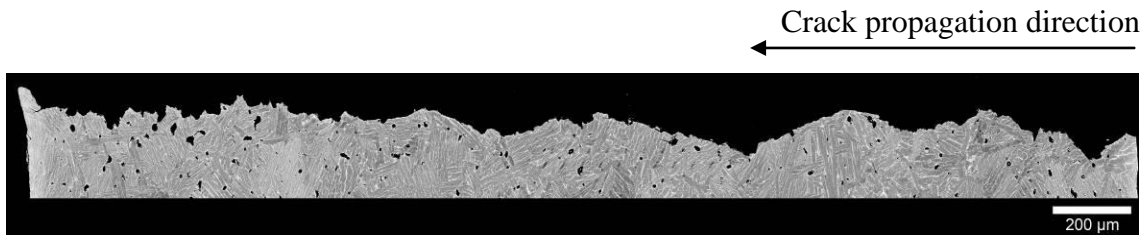


Fig. 49. Typical crack front profile of MIM31L samples with shot peening.

The right side of Fig. 49 represents the lower left side of Fig. 46, which is assumed to be the crack initiation location. Higher magnification of the assumed nucleation region is illustrated in Fig. 50.

Apparently, secondary cracks are originated in a subsurface level. Typical features near by the secondary cracks were flat regions (facets) pointed to by the white arrows.

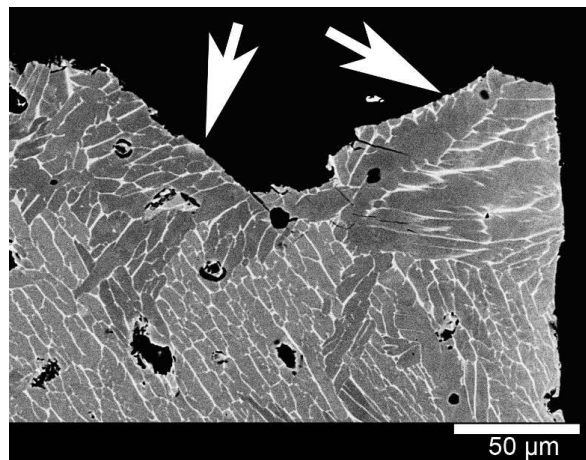


Fig. 50. Higher magnification of the crack front profile at crack nucleation site of MIM31L samples with shot peening, BSE image mode.

5.3.2. The internal stresses promoted by the shot peening

Several authors demonstrated that the application of shot peening on Ti-6Al-4V alloy samples promoted internal compressive residual stress in the range of 600 MPa to 900 MPa [12, 14, 100-102]. Furthermore, Lütjering [14] reported that with a pressure of

4 bar the depth of the layer that exhibited internal compressive stress for the Ti-6Al-4V alloy is approximately 300 μm . It is expected that within this layer the dislocation density is much larger than in the interior of the samples. Thus, it should be possible to do a recrystallization process by heat treatment, if the dislocation density is high enough to promote the nucleation of the new grains.

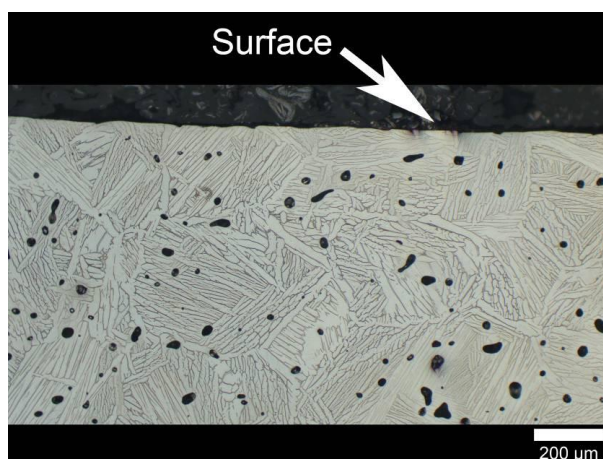


Fig. 51. Typical microstructure of the MIM35H+SP+HT samples.

Nevertheless, as illustrated by Fig. 51 the microstructure at the surface of the MIM35H+SP+HT sample exhibited the same features compared to the inner regions. This indicated that no refinement (recrystallization) occurred during the heat treatment. Furthermore, the heat treatment did not promoted a significant change in the impurity levels as illustrated in Table 6.

Table 6. Chemical concentration of interstitial alloying element of MIM35H and MIM35H+SP+HT samples.

Interstitial alloying element	MIM35H	MIM35H+SP+HT
Average C content [$\mu\text{g/g}$]	409 ± 23	346 ± 14
Average N content [$\mu\text{g/g}$]	172 ± 24	136 ± 9
Average O content [$\mu\text{g/g}$]	2318 ± 44	2142 ± 123
$\text{O}_{(\text{eq.})}$ [$\mu\text{g/g}$]	2969 ± 109	2673 ± 152

The fatigue behaviour trend of the MIM35H+SP+HT samples is plotted in Fig. 52. After the heat treatment the samples exhibited approximately the same fatigue behaviour as the MIM35H samples without shot peening.

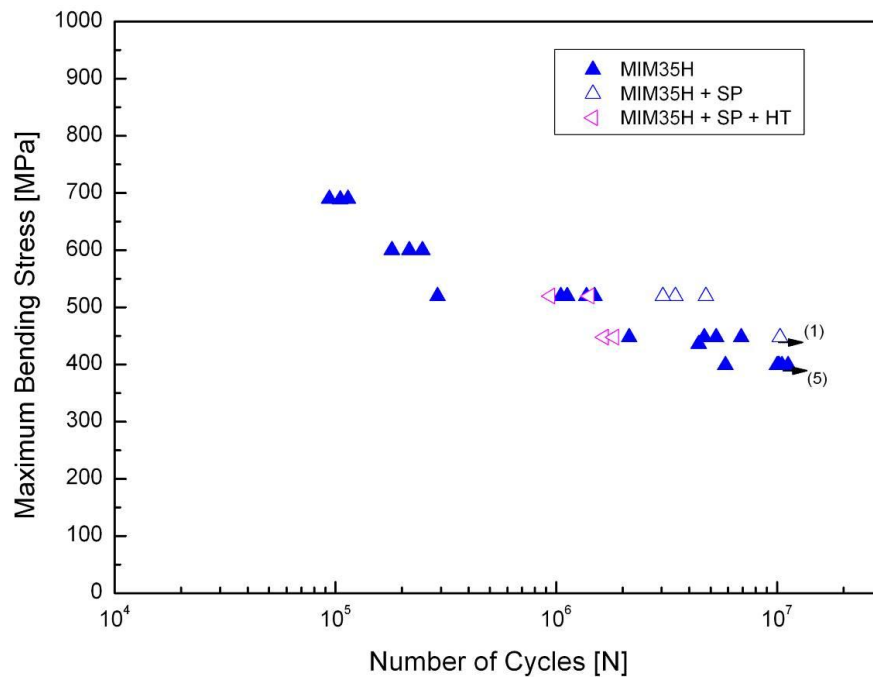


Fig. 52. S-N curve of the MIM35H, MIM35H+SP and MIM35H+SP+HT samples.

A typical fracture surface of the MIM35H+SP+HT samples at the assumed crack nucleation site is shown in Fig. 53. The crack nucleation for these samples is assumed to be located at the surface of the samples. A facet is directly located near to the surface as illustrated in Fig. 53b. The typical notches presented in the assumed crack nucleation site of the MIM31L samples without shot peening (Fig. 41) were not observed for the MIM35H+SP+HT samples.

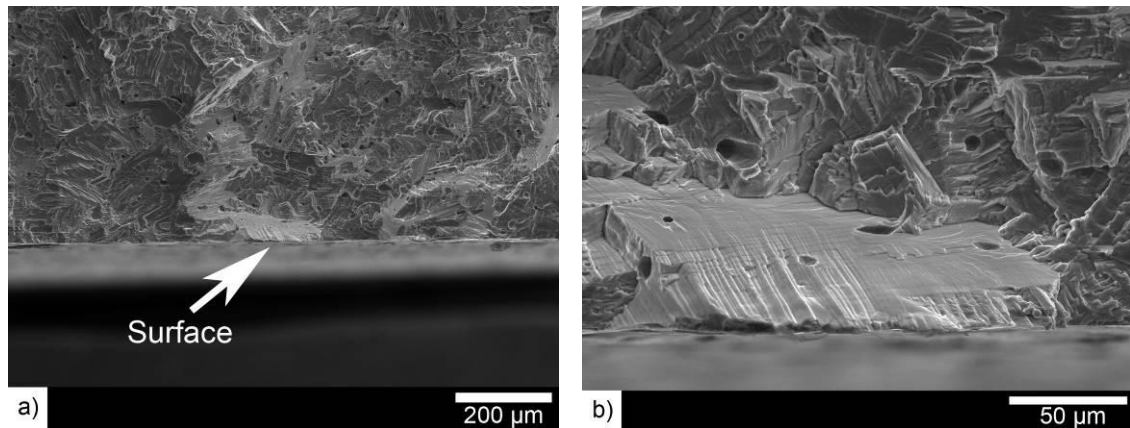


Fig. 53. Typical fracture surface of MIM35H+SP+HT samples, (a) lower magnification (b) higher magnification of crack initiation location.

All the samples used to obtain the following fatigue results were exposed to shot peening prior the fatigue tests. Such procedure was carried out due to the fact that differences in the surface quality tend to be the determinant factor to describe the fatigue behaviour of a given material. This means other factors could remain undetected. Therefore, the surface quality needs to be as similar as possible in order to investigate e.g. the influence of microstructural features. As an attempt to assure relatively identical surface qualities for the different studied configurations shot peening was applied.

5.4. Particle size

In one attempt to obtain lower porosity levels, samples were fabricated by using a Ti-6Al-4V ELI powder with a particle size below 25 μm (samples are referring as 25MIM35L).

5.4.1. Microstructural features and tensile properties

The α colony size of 25MIM35L samples was approximately 150 μm (Table 7). The apparent porosity, also visible in Fig. 54, observed on 25MIM35L samples was 2.0 vol.%.

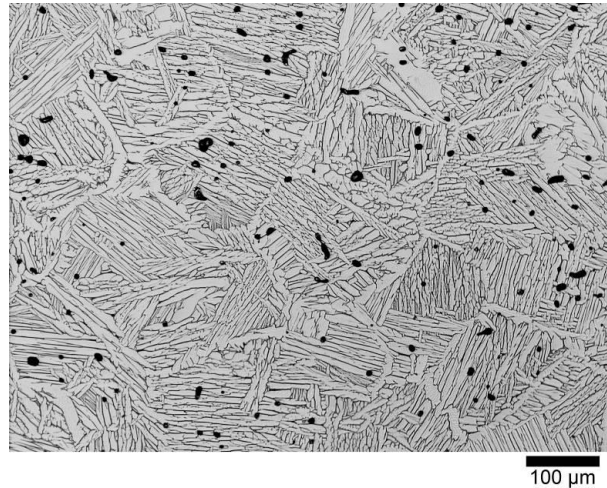


Fig. 54. Microstructure of MIM Ti-6Al-4V with 35 vol.% of binder, particle size below 25 μm and sintered at 1250 $^{\circ}\text{C}$ (25MIM35L).

The amount of porosity for the 25MIM35L decreased compared to MIM31L or MIM35H samples (Table 4). Additionally, similar grain size was obtained for 25MIM35L samples and MIM35H samples.

Fig. 55 illustrates the pore diameter distribution for the 25MIM35L samples.

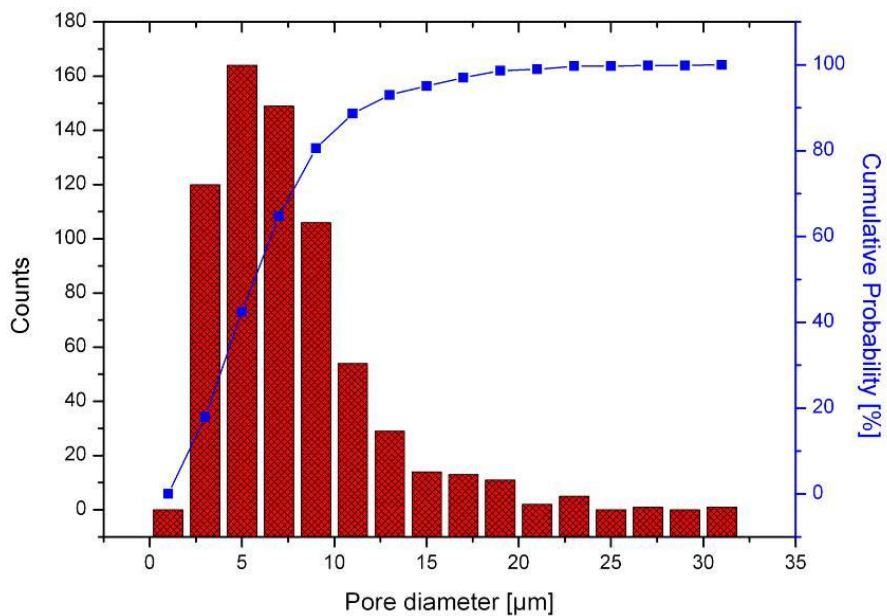


Fig. 55. Pore diameter distribution and cumulative probability for 25MIM35L samples.

The average pore diameter was approximately 7 μm and the maximum pore diameter measured was 31 μm (670 pores were analysed). In general, a slight reduction of the pore size diameter is observed by changing the maximum powder particle size from 45 μm to 25 μm .

Table 7 illustrates the tensile behaviour and the impurity levels of the sintered 25MIM35L samples. For comparison, the impurity levels and tensile properties of MIM35H samples are shown, too. Better tensile properties were obtained for MIM samples processed with particle size below 25 μm . Moreover, a marginal increase of the impurity levels was observed for 25MIM35L samples compared to the samples processed with the powder size below 45 μm .

Table 7. Microstructural features and tensile properties of MIM35H and 25MIM35L samples.

Microstructural features and tensile properties	MIM35H	25MIM35L
Sinter density [g/cm³]	4.25	4.32
Porosity [%]	3.6	2.0
α colony size [μm]	148 \pm 20	150 \pm 23
Average C content [$\mu\text{g/g}$]	409 \pm 23	652 \pm 53
Average N content [$\mu\text{g/g}$]	172 \pm 24	178 \pm 6
Average O content [$\mu\text{g/g}$]	2318 \pm 44	2449 \pm 24
O_(eq.) [$\mu\text{g/g}$]	2969 \pm 109	3295 \pm 72
σ_y [MPa]	720 \pm 2	791 \pm 8
UTS [MPa]	824 \pm 4	900 \pm 7
Elongation [%]	13.4 \pm 0.7	15.3 \pm 1

5.4.2. Fatigue behaviour

The results of high cycle four-point bending fatigue test for 25MIM35L and MIM35H with shot peening are shown in Fig. 56. Only the high cycle region (10^6 to 10^7 cycles) was investigated for the 25MIM35L samples. A relative small increase of the fatigue resistance of the 25MIM35L samples with shot peening is observed compared to the MIM35H samples with shot peening.

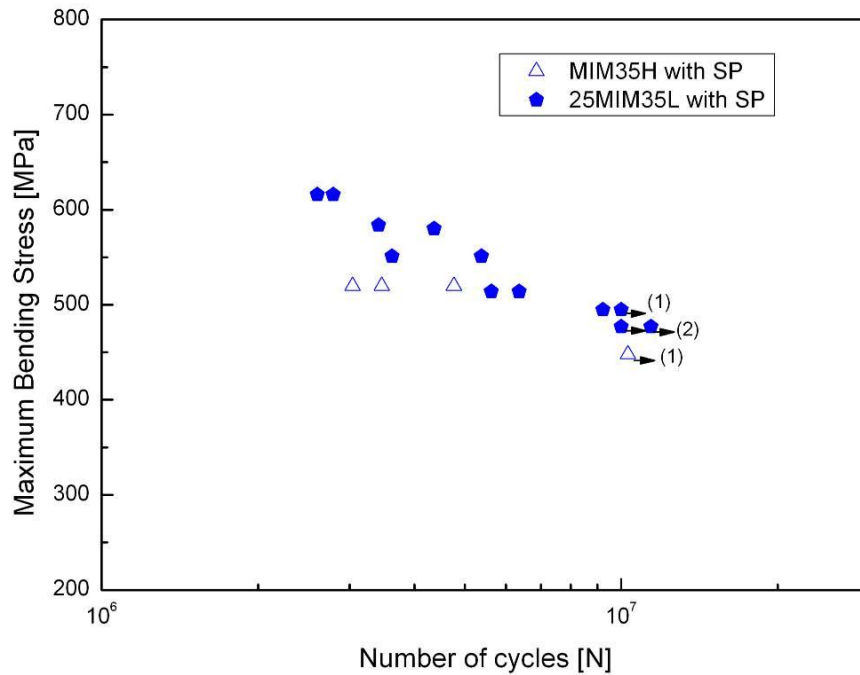


Fig. 56. S-N curves for 25MIM35L and MIM35H samples. All samples were exposed to shot peening (SP) prior to testing.

A typical fracture surface of 25MIM35L samples is illustrated in Fig. 57. The shape of the rough region indicates that the crack initiation location was close to the lower right corner.

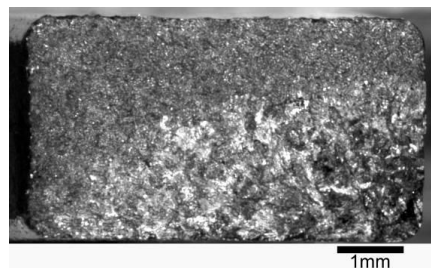


Fig. 57. Typical fracture surface of 25MIM35L samples.

SEM micrographs of the assumed crack nucleation region are shown in Fig. 58. Facets and pores are typical visible features. Apparently, as for the other configurations that were exposed to shot peening, the crack initiation location was in a subsurface level.

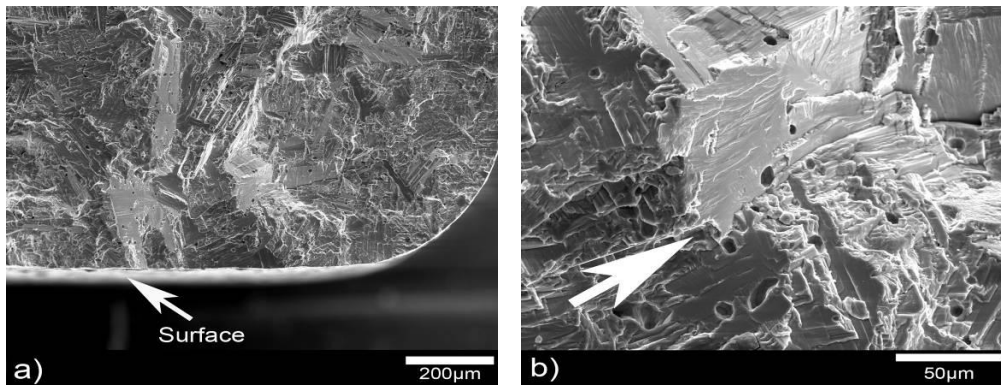


Fig. 58. Typical fracture surface of 25MIM35L samples with shot peening: (a) lower magnification and (b) higher magnification of crack initiation location.

5.5. The MIM+HIP configuration

5.5.1. Microstructural features

The microstructure of the MIM35H samples after the HIP process is shown in Fig. 59.

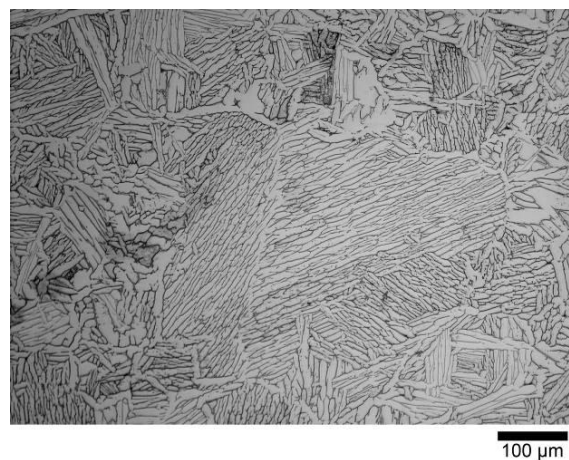


Fig. 59. Microstructure of MIM35H samples after HIP process.

After the HIP process no remaining porosity was observed on the investigated microstructure. The relative density was determined using the immersion method, and the value obtained (4.41 g/cm^3) was similar to the values accepted for the wrought Ti-6Al-4V alloy after annealing [17].

Table 8. Microstructural features and impurity levels of MIM35H samples with and without HIP.

Microstructural Features	MIM35H	MIM35H + HIP
Sinter density [g/cm³]	4.25	4.41
Porosity [%]	3.6	-
α colony size [μm]	148 \pm 20	174 \pm 26
Average C content [$\mu\text{g/g}$]	409 \pm 23	480 \pm 7
Average N content [$\mu\text{g/g}$]	172 \pm 24	177 \pm 5
Average O content [$\mu\text{g/g}$]	2318 \pm 44	2308 \pm 16
O_(eq.) [$\mu\text{g/g}$]	2969 \pm 109	3023 \pm 32

The impurity levels were investigated and the results are shown in Table 8. Furthermore, due to an additional exposure of the samples to a relative high temperature (915 °C) and pressure (100 MPa), a coarsening of the microstructure was observed (Fig. 59). The MIM35H+HIP samples presented similar values for the oxygen, nitrogen and carbon contents as the MIM35H samples.

5.5.2. Tensile properties

The tensile properties of the MIM35H+HIP samples are compared to the MIM35H samples in Table 9.

Table 9. Tensile properties of MIM35H with and without HIP.

Tensile property	MIM35H	MIM35H + HIP
Yield Stress [MPa]	720 \pm 2	841 \pm 5
Maximum Stress [MPa]	824 \pm 4	937 \pm 3
Elongation [%]	13.4 \pm 0.7	17.1 \pm 2

A significant improvement of the tensile properties was observed for the MIM35H+HIP samples. The tensile fracture surface demonstrated a completely fine dimpled structure (Fig. 60). Such structure is in agreement with the obtained higher values for plastic elongation.

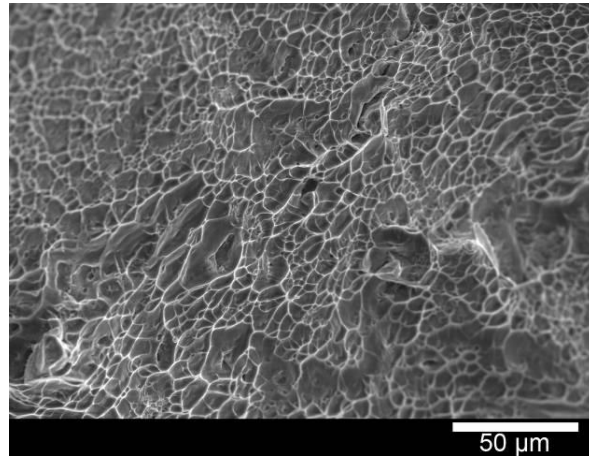


Fig. 60. Typical tensile fracture surface of MIM35H+HIP samples. An fine dimpled structure is visible.

5.5.3. Fatigue behaviour

Fig. 61 illustrates the results of the high cycle four-point bending fatigue tests for MIM35H+HIP samples with shot peening. The elimination of the porosity promoted an improvement of the fatigue behaviour, from 450 MPa to 500 MPa. The fracture surfaces of the MIM35H+HIP samples with shot peening are shown in Fig. 62 and Fig. 63.

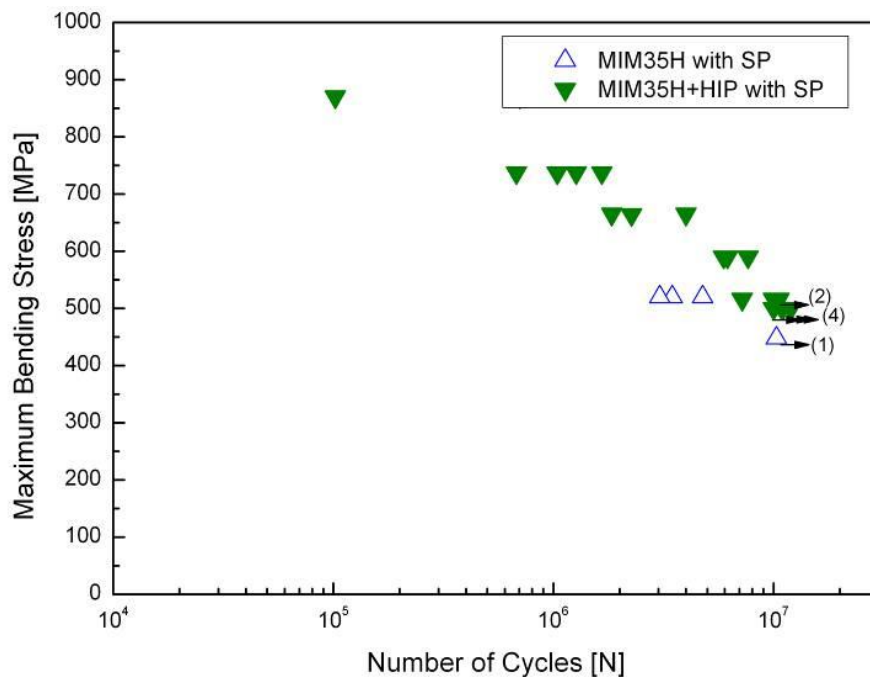


Fig. 61. S-N curves for MIM31L and MIM35H+HIP samples. All samples were exposed to shot peening (SP) prior to testing.

Based on the topography difference exhibited in Fig. 62, it was possible to assume that the crack initiation location was at a subsurface level located approximately in the lower centre site of the fracture surface.

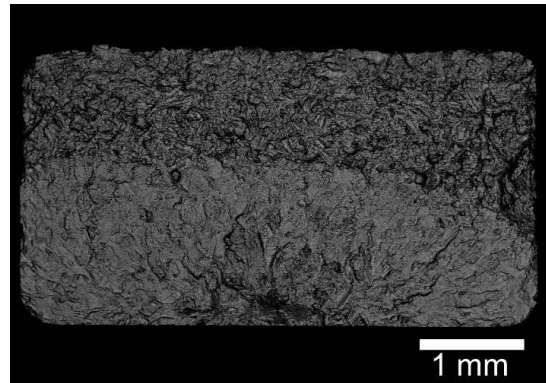


Fig. 62. BSE micrograph of a typical fracture surface of MIM+HIP samples with shot peening.

The white arrow in Fig. 63 indicates the surface that was exposed to tensile stress during the four-point bending fatigue test. As for the previous fracture surfaces studied in this investigation, the facets were also observed for the MIM35H+HIP samples. No porosity and surface defects were identified.

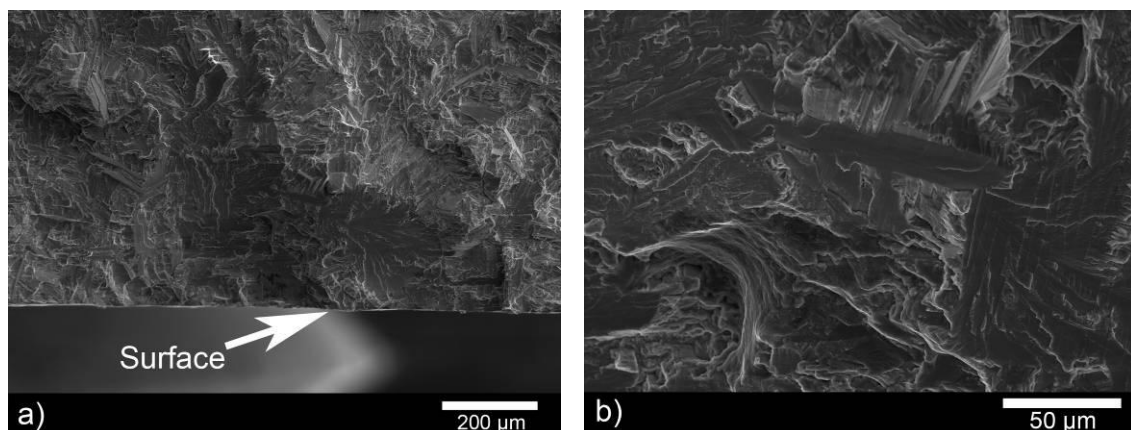


Fig. 63. Typical fracture surface of MIM35H+HIP samples with shot peening: (a) lower magnification and (b) higher magnification of crack initiation location.

Note that apart from the facets, a region with a different topography pointed out by the white arrow (a) in Fig. 64 is presented in the assumed crack nucleation region. The energy dispersive X-ray spectroscopy (EDX) of this region (white arrow (a) in Fig. 64) and the facets (white arrow (b) in Fig. 64) are summarized in Table 10.

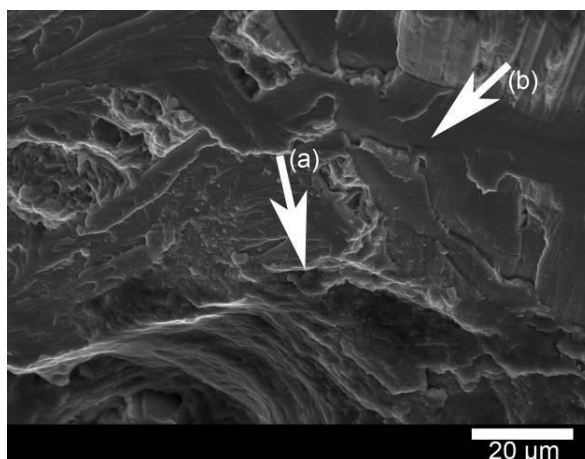


Fig. 64. Typical fracture surface of MIM35H + HIP samples with shot peening at higher magnification of crack initiation location. White arrows (a) and (b) indicated the EDX analysed regions.

The region pointed by the white arrow (a) in Fig. 64 exhibited higher oxygen content than the region indicated by the white arrow (b), see Table 10.

Table 10. EDX of the fine particles and the facet regions.

Position	Element	Weight [%]	Atomic [%]
White arrow (a) in Fig. 64	Ti	44.8	22.7
	Al	2.5	2.3
	V	4.3	2.1
	O	48.3	73.0
White arrow (b) in Fig. 64	Ti	84.6	80.9
	Al	6.5	11.0
	V	9.0	8.1
	O	-	-

5.6. The Powder+HIP configuration

5.6.1. Microstructural features

The microstructure of the Ti-6Al-4V alloy Powder+HIP samples is shown in Fig. 65. The dark regions are the β phase and the white regions are the α phase. The grain size and the lamellae are not well defined. However, it was possible to observe that there were regions with very fine lamellae and other regions with larger α phase that resemble the equiaxed microstructure. Therefore, it is assumed that this microstructure is a transition between equiaxed and lamellar microstructure. Although the identification of the grain boundaries was not clear, the microstructure of the Powder+HIP samples apparently is much finer than the MIM samples (lamellar microstructure).

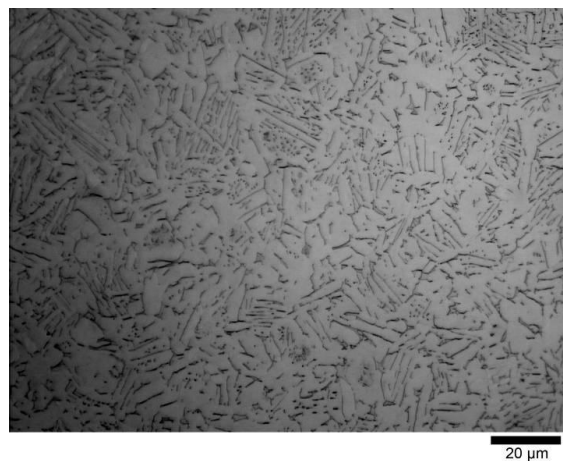


Fig. 65. Microstructure of Powder+HIP samples.

In an attempt to quantify the microstructure size of the Powder+HIP samples EBSD measurements were performed and the results are shown in Fig. 66. Based on Fig. 66b, the average α grain and α colony sizes were estimated to be around 9 μm . Although the BSE image (Fig. 66a) and the β phase mapping (Fig. 66c) are in a good agreement, the thinner β phase regions were not indexed as β phase, only coarser β regions were indexed properly.

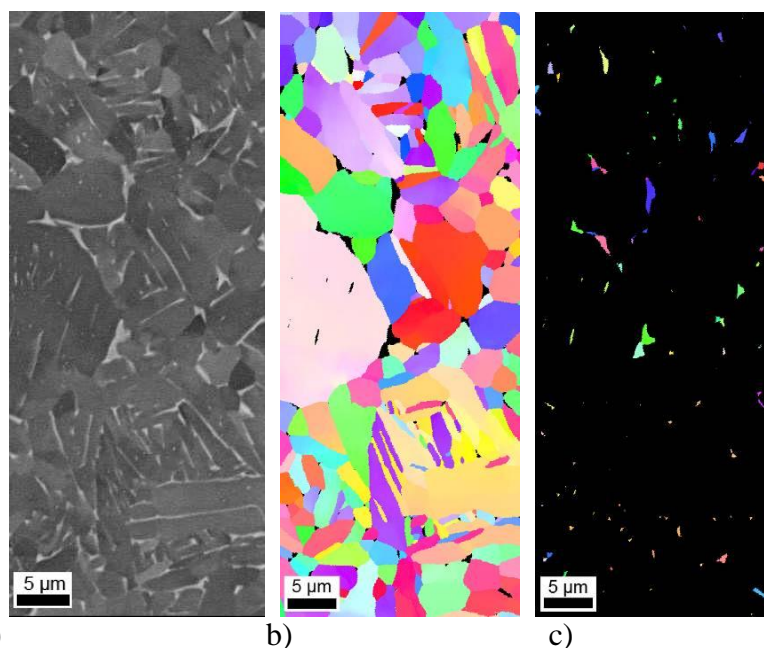


Fig. 66. EBSD phase map of Powder+HIP sample: representation of the (a) BSE image, (b) α phase and (c) β phase. Each colour (gray scale for copy) is related to a specific orientation.

The impurity levels of the Ti-6Al-4V alloy Powder+HIP samples are illustrated in Table 11.

Table 11. Chemical concentration of interstitial alloying element of Ti-6Al-4V alloy powder and Ti-6Al-4V alloy powder+HIP.

Interstitial alloying element	Ti-6Al-4V ELI Powder	Powder+HIP
Average C content [$\mu\text{g/g}$]	200	205 ± 67
Average N content [$\mu\text{g/g}$]	100	179 ± 10
Average O content [$\mu\text{g/g}$]	1000	1768 ± 136
$\text{O}_{(\text{eq.})}$ [$\mu\text{g/g}$]	1350	2280 ± 207

After the HIP process, the impurity levels increased, especially for oxygen content. However, the oxygen levels for the Powder+HIP samples are still below the common values obtained for the investigated MIM samples (1900 – 2300 $\mu\text{g/g}$).

5.6.2. Tensile properties

The tensile properties of the Powder+HIP samples were obtained by using micro-tensile specimens. In order to compare the properties with the MIM dog-bone shaped samples, micro-tensile specimens from MIM35H samples were also investigated. Table 12 illustrates the results for Powder+HIP samples and MIM35H samples.

Table 12. Tensile properties of Powder+HIP and MIM35H samples

Tensile property	Powder+HIP*	MIM35H*	MIM35H
Yield Stress [MPa]	772 ± 18	655 ± 48	720 ± 2
Maximum Stress [MPa]	832 ± 20	750 ± 14	824 ± 4
Elongation [%]	13.9 ± 4	8.2 ± 1.1	13.4 ± 0.7

*values obtained by using micro-tensile specimens.

The tensile behaviour was affected by the specimen geometry. The tensile property for the MIM35H samples using the micro-tensile specimens exhibited poorer values and larger scatter than the values obtained for the dog-bone specimens. Considering the elongation values, even larger scatter was observed for the Powder+HIP samples compared to the MIM35H samples. The tensile elongation scattering for the Powder+HIP samples is significant and a more detailed analysis was required. Tensile fracture surfaces of the Powder+HIP samples, that demonstrated different plastic elongation, were investigated in order to describe such phenomenon. Fig. 67 shows two tensile fracture surfaces of Powder+HIP samples: (a) is referring to 10 % of plastic elongation and (b) to 17 % of plastic elongation.

A fine dimpled structure is observed for both fracture surfaces. However, a particle surrounded by a flat region (white arrow in Fig. 67a indicated this defect) is observed on the tensile fracture surface of the sample that exhibited only 10 % of plastic elongation. Such a defect was not identified on the tensile fracture surface of the samples that presented higher plastic elongation.

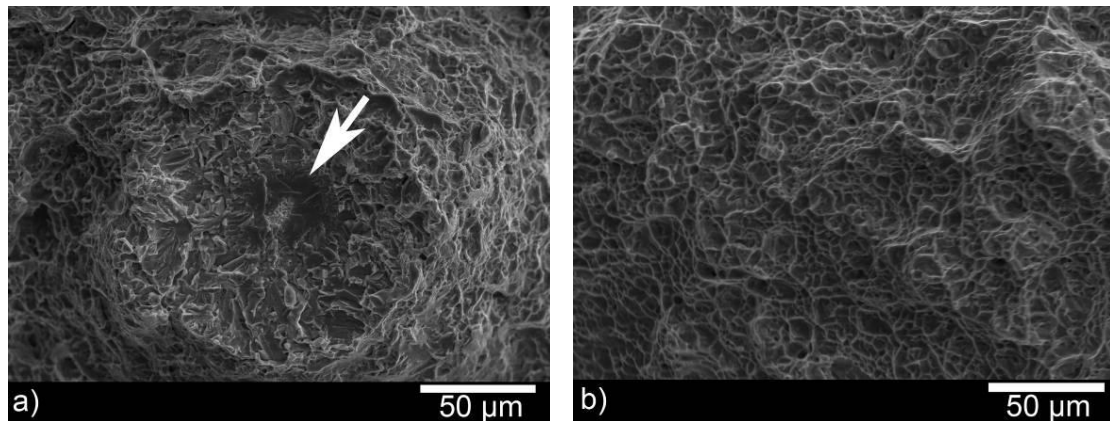


Fig. 67. Tensile fracture surfaces of Powder + HIP samples: (a) 10 % of plastic elongation, (b) 17 % of plastic elongation.

A typical tensile fracture surface of the MIM35H samples (micro-tensile specimens) is shown in Fig. 68. Regions with fine dimples, coarser dimples and pores are presented. Such features were also observed for the tensile fracture surface of the dog-bone samples (Fig. 36).

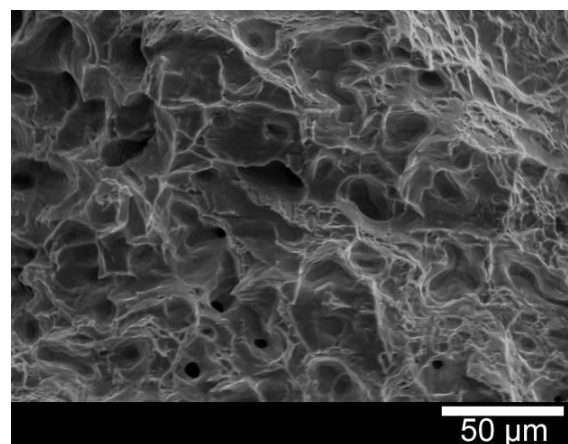


Fig. 68. Typical tensile fracture surface of the MIM35H samples (micro-tensile specimens).

5.6.3. Fatigue behaviour

All samples shown here were exposed to the shot peening process prior to the fatigue experiments. The S-N curve for the Powder+HIP samples is plotted in Fig. 69 together with the MIM35H and the MIM35H+HIP samples.

The large scattering observed for tensile test was also present in the fatigue results for Powder+HIP samples. In general, the fatigue resistance of Powder+HIP samples was higher than the MIM35H and MIM35H+HIP samples. Fig. 70 illustrates a typical fatigue fracture surface of Powder+HIP samples with shot peening.

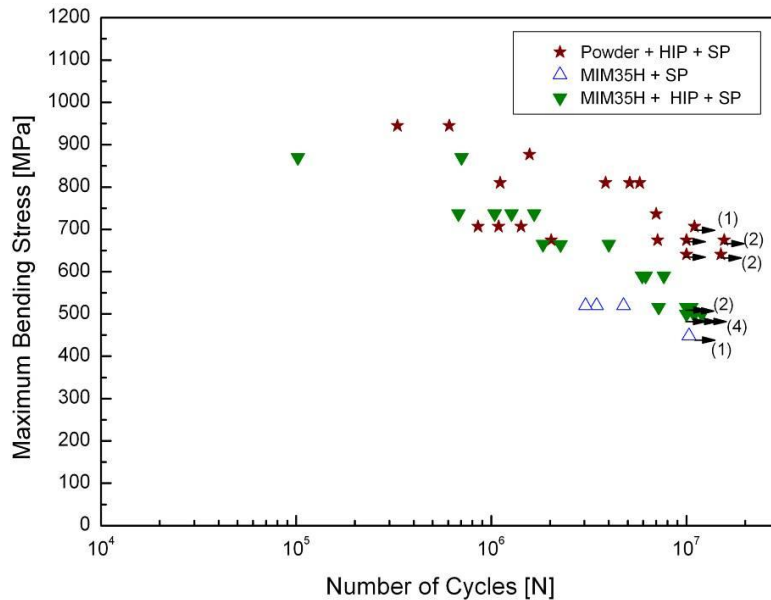


Fig. 69. S-N curves for MIM35H, MIM35H+HIP and Powder+HIP samples. All samples were exposed to shot peening (SP) prior testing.

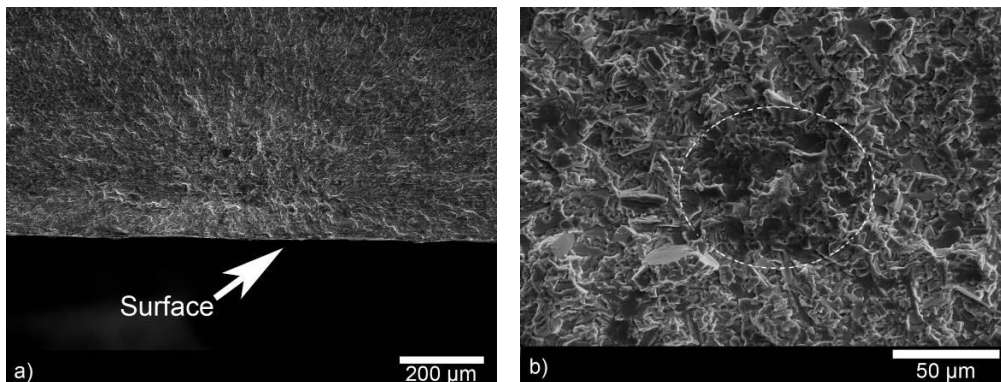


Fig. 70. Typical fracture surface of Powder + HIP samples with shot peening: (a) lower magnification and (b) higher magnification of crack initiation location.

The white ellipse indicates approximately the crack nucleation site. A higher magnification micrograph of this region is shown in Fig. 71. The particle observed in Fig. 71 exhibited a complete different morphology compared to the typical fracture

surface. Apart from the particle, it was also possible to identify the presence of the facets in the assume crack initiation location.

The EDX analyses of the particle and a region near by the particle are shown in Table 13. They indicate that most probably the particle was magnesium oxide. It is important to note that at the assume crack initiation location for all investigated fatigue fracture surfaces of Powder+HIP samples a particle such as illustrated in Fig. 71 was presented.

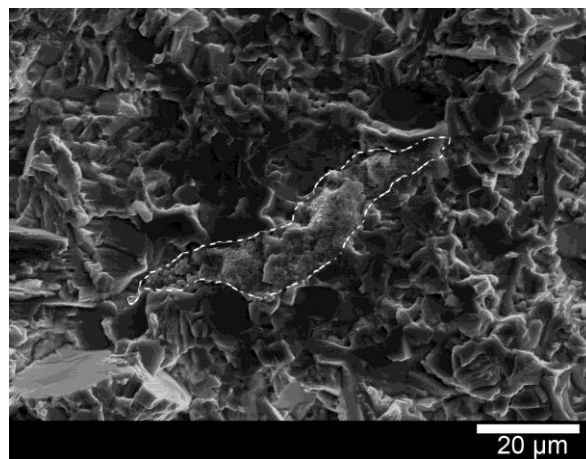


Fig. 71. Typical fracture surface of Powder+HIP samples with shot peening. Higher magnification at the assume crack nucleation site. The particle is highlighted by the white line.

Table 13. EDX of the particle and the matrix (Fig. 71).

Position	Element	Weight [%]	Atomic [%]
Particle	Ti	50.8	29.0
	Al	1.2	1.2
	V	1.5	0.8
	Mg	17.8	20.0
	O	28.7	49.0
Matrix	Ti	88.4	83.4
	Al	7.9	13.2
	V	3.7	3.3
	Mg	-	-
	O	-	-

5.7. Addition of boron on Ti-6Al-4V alloy

5.7.1. Boron content

The influence of small boron additions on the microstructure evolution during sintering process of the Ti-6Al-4V alloy processed by MIM was investigated. The microstructure of samples with additions of 0, 0.1 and 0.5 wt. % of boron on the Ti-6Al-4V alloy sintered at 1250 °C are shown in Fig. 72, Fig. 73 and Fig. 74, respectively.

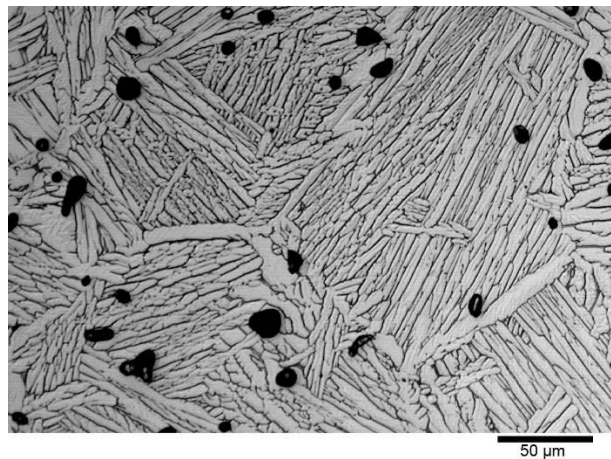


Fig. 72. Microstructure of Ti-6Al-4V alloy sintered at 1250 °C for two hours and 10 °C/min cooling rate.

As it can be seen in all figures, the addition of boron significantly modifies a number of microstructural features. In terms of α colony size the Ti-6Al-4V alloy samples with no addition of boron showed values of approximately 100 μm . With the addition of 0.1 wt.% of boron, the α colony size was reduced to approximately 80 μm .

The samples with 0.5 wt.% of boron addition exhibited a microstructure with no well defined α colony: in other words, the lamellar structure was suppressed. Because the grain boundaries were not clearly detectable by common microscopy, the grain size was quantified by EBSD measurements. The results are shown in section 5.7.3.

The white arrows in Fig. 73 and Fig. 74 indicate the TiB_w particles ($w = 1$ or 2) formed during the sintering process (in situ reaction). The increase of boron content apparently promoted a refinement of the microstructure; however, at this maximum sintering

temperature of 1250 °C, an increase of porosity was also observed: the Ti-6Al-4V alloy samples sintered at 1250 °C exhibited a relative densification of approximately 97 %. The addition of 0.1 wt.% boron promoted a decrease in the relative densification to approximately 96%. Furthermore, addition of 0.5 wt.% boron significantly decreased the relative densification to a value of approximately 91%. In order to obtain samples with a lower level of porosity the samples with 0.5 wt.% of boron addition were sintered at higher temperature. The relative densification results are plotted in Fig. 75 for samples sintered at 1250 °C and 1400 °C.

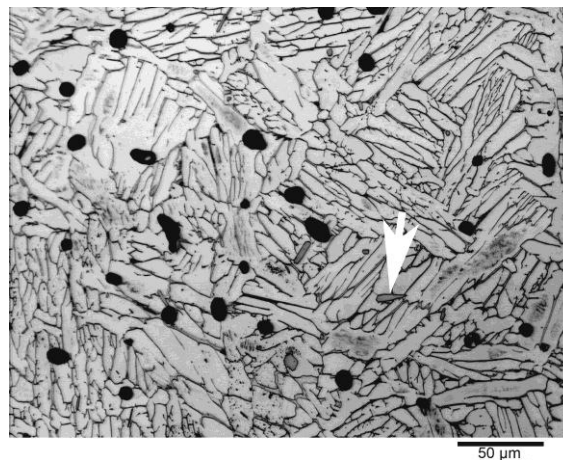


Fig. 73. Microstructure of Ti-6Al-4V-0.1B alloy sintered at 1250 °C for two hours and 10 °C/min cooling rate.

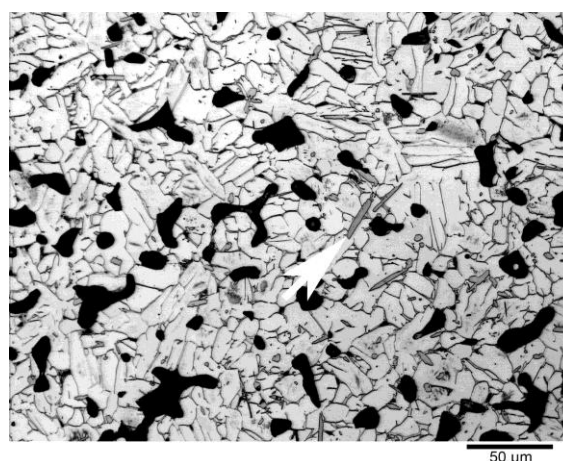


Fig. 74. Microstructure of Ti-6Al-4V-0.5B alloy sintered at 1250 °C for two hours and 10 °C/min cooling rate.

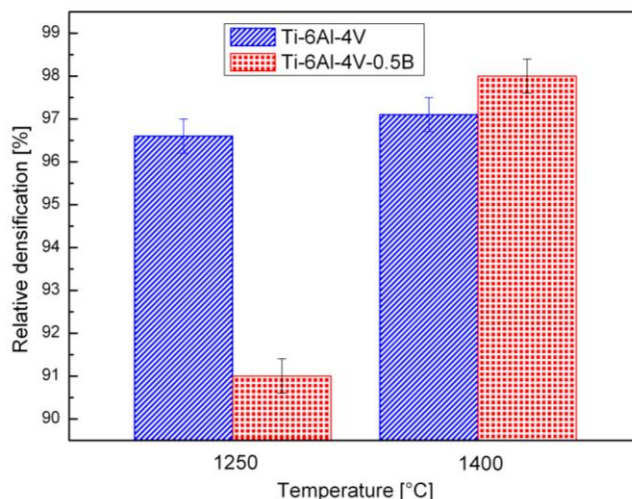
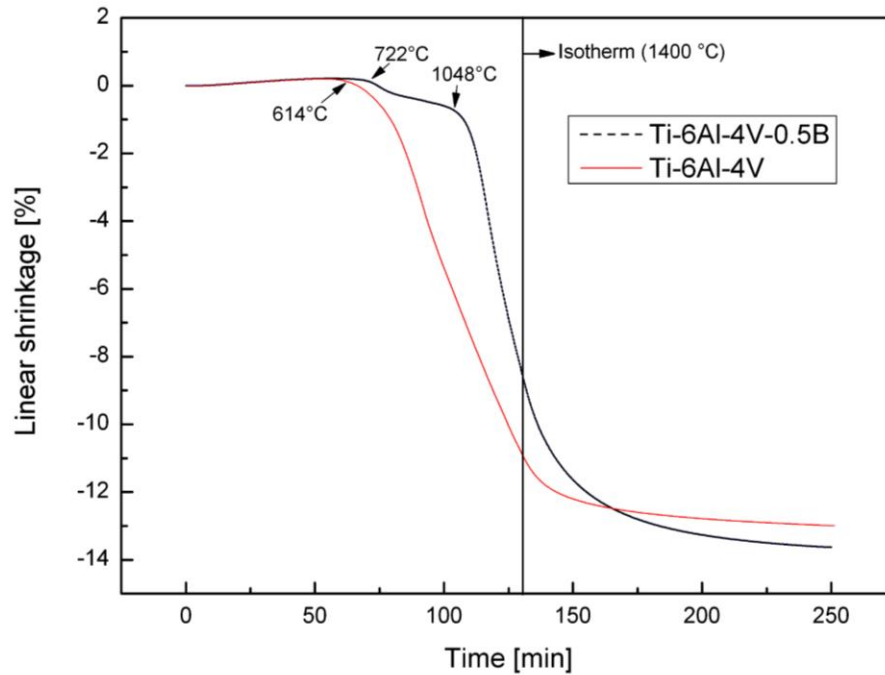


Fig. 75. Relative densification of Ti-6Al-4V alloy with and without addition 0.5 wt.% of boron at two different maximum sintering temperatures: 1250 °C and 1400 °C.

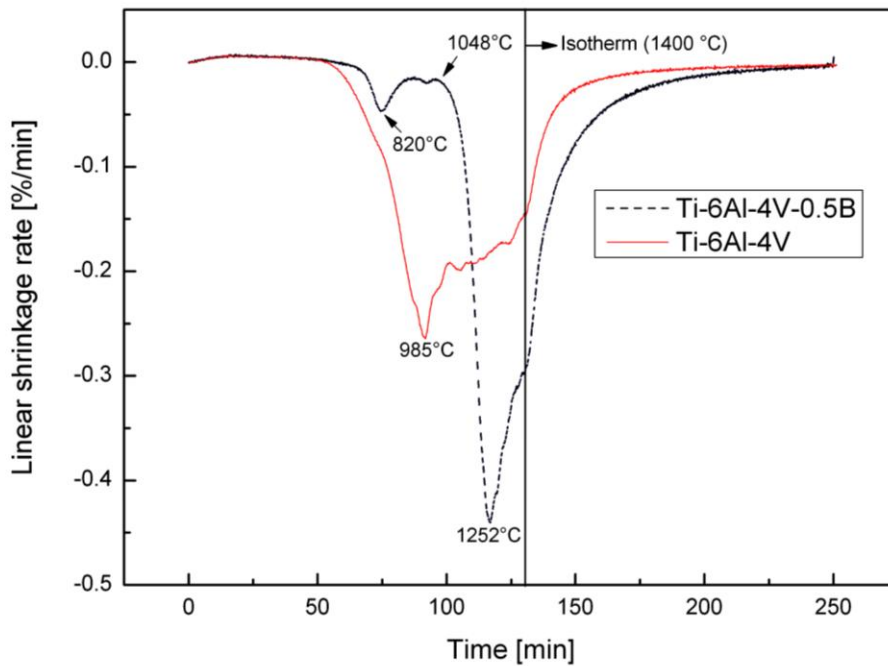
The negative influence of boron addition on the densification of the samples during sintering at 1250 °C was not observed for the samples sintered at 1400 °C. In this case the samples with boron addition exhibited even a higher relative densification than those samples without boron addition. This interesting behaviour was detailed investigated by using the dilatometry technique.

5.7.2. Dilatometry

Fig. 76a and b illustrate the linear shrinkage (LS) and the linear shrinkage rate (LSR) of the Ti-6Al-4V alloy with and without 0.5 wt.% of boron, respectively. The Ti-6Al-4V alloy started earlier to shrink compared to the samples with boron addition. After 820 °C the Ti-6Al-4V-0.5B sample exhibited a significant decrease of the LSR until approximately 1048 °C. The Ti-6Al-4V alloy exhibited a maximum LSR of 0.27 %/min at approximately 985 °C. Above this temperature the LSR started to decrease which is an indication of the final sintering stage's initiation. On the other hand, the Ti-6Al-4V-0.5B alloy started to shrink significantly above 1048 °C. The maximum LSR achieved for this alloy during dilatometry experiments was approximately 0.45 %/min at about 1252 °C. The maximum LSR for Ti-6Al-4V-0.5B was approximately two times higher. Additionally, the alloys with and without boron addition exhibited after two hours at 1400 °C a LS of approximately 13.6 % and 12.9 %, respectively.



a)



b)

Fig. 76. Dilatometry of Ti-6Al-4V and Ti-6Al-4V-0.5B alloys: a) linear shrinkage (LS) and b) linear shrinkage rate (LSR). Starting acquisition data at 75 °C.

It is important to note that the LS of the Ti-6Al-4V-0.5B alloy achieved higher values than the Ti-6Al-4V alloy only after 33 minutes at 1400 °C, as it started later.

5.7.3. Impurity levels and microstructural features

The impurity levels of the Ti-6Al-4V-0.5B samples sintered at 1400 °C together with the MIM35H samples are shown in Table 14. Lower remaining porosity was observed for the samples with 0.5 wt. % of boron addition compared to the MIM35H samples. In terms of impurity levels, the samples with boron addition exhibited lower oxygen equivalent. Fig. 77 shows the microstructure of the Ti-6Al-4V-0.5B alloy sintered at 1400 °C for two hours. A significantly finer microstructure was observed compared to the MIM35H (Fig. 32).

Table 14. Microstructural features of Ti-6Al-4V-0.5B and MIM35H samples

Microstructural Features	Ti-6Al-4V-0.5B	MIM35H
Sinter density [g/cm ³]	4.31	4.25
Porosity [%]	2.3	3.6
α colony size [μm]	18 \pm 5	148 \pm 20
Average C content [$\mu\text{g/g}$]	390 \pm 33	409 \pm 23
Average N content [$\mu\text{g/g}$]	164 \pm 6	172 \pm 24
Average O content [$\mu\text{g/g}$]	1960 \pm 21	2318 \pm 44
O _(eq.) [$\mu\text{g/g}$]	2580 \pm 58	2969 \pm 109

The remaining porosity was investigated and the pore size distribution is plotted in Fig. 78. The average pore size was 12 μm and the total number of analyzed pores was 345. The maximum observed pore diameter was 41 μm .

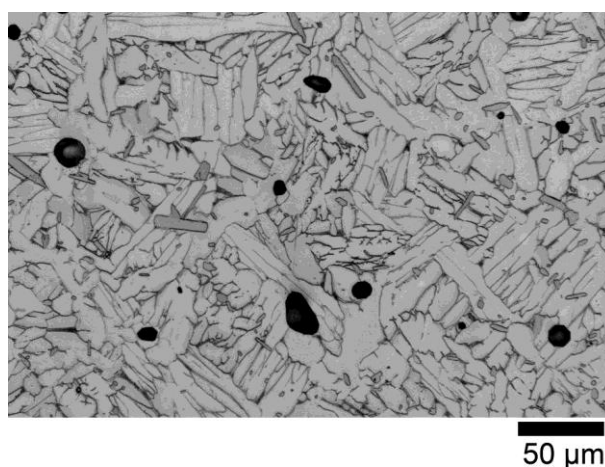


Fig. 77. Microstructure of Ti-6Al-4V-0.5B alloy sintered at 1400 °C for two hours a cooling rate of 10 °C/min.

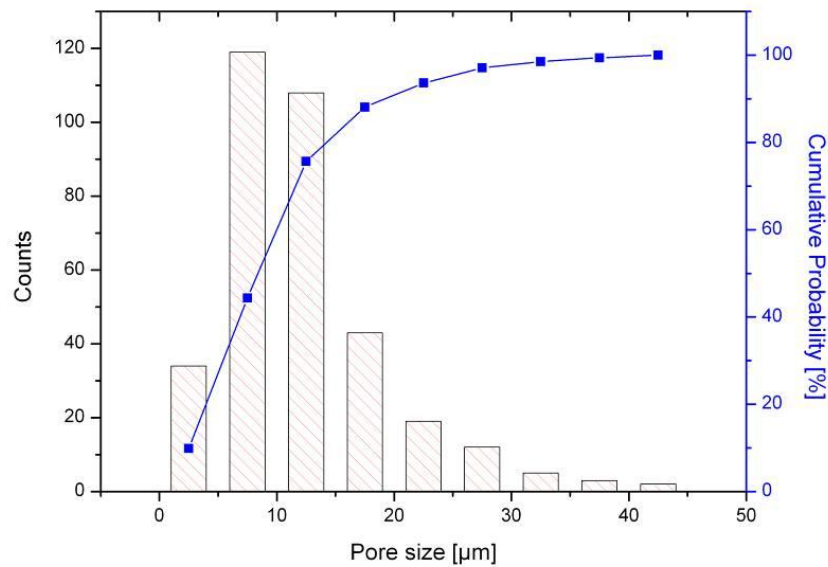


Fig. 78. Pore diameter distribution and cumulative probability for Ti-6Al-4V-0.5B samples.

With the EBSD measurements (Fig. 79) it was possible to identify clearly the phases and their orientation. Each different colour represents a different orientation. Regions with α colonies (α lamellae with the same orientation) and single α grains (no β phase was detected in these specific grains, which is a typical feature of the equiaxed microstructure) were observed in Fig. 79b.

A higher magnification was used in order to better identify these two regions (α colonies and α grains). The regions defined as (I) in Fig. 80b refer to the α colonies. Note that only few lamellae had the same orientation at a specific α colony. The regions (II) indicate a single α grain with no orientation relationship to neighboured α phase lamellae or grain.

Furthermore, it was possible to clearly identify the β phase (Fig. 79c) and the related orientations. Information regarding to the β phase grain size was obtained by analysing the β phase regions with same orientation.

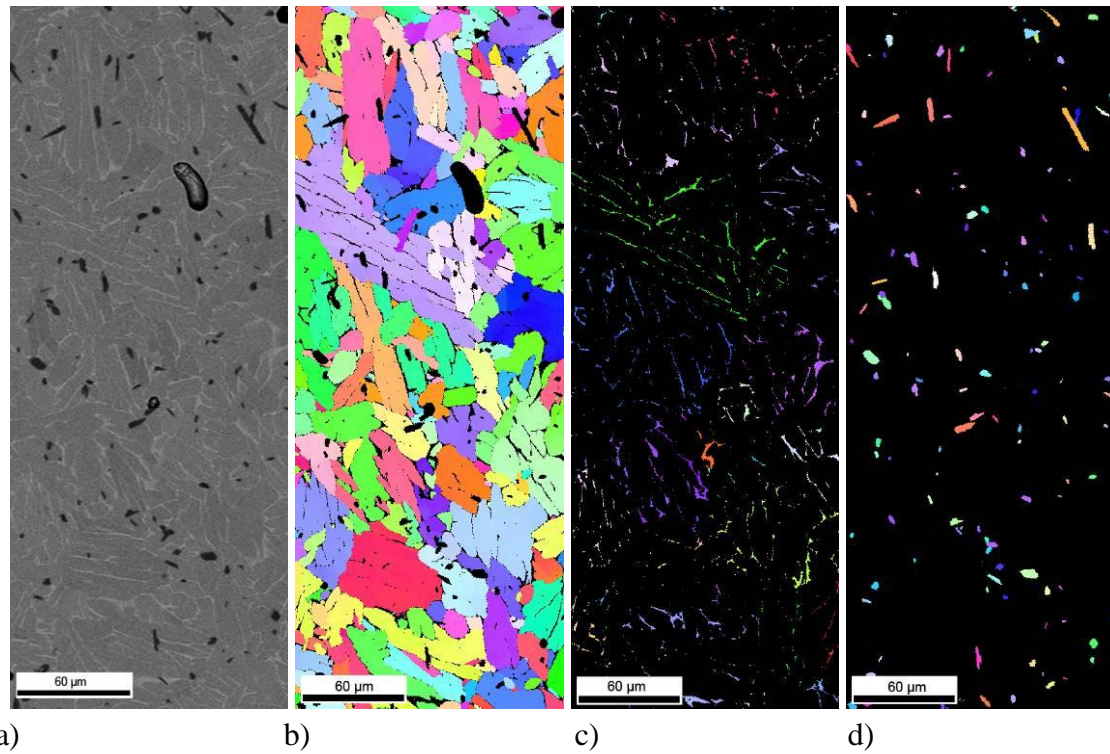


Fig. 79. EBSD phase map of Ti-6Al-4V-0.5B sintered at 1400 °C: representation of the (a) BSE image, (b) α phase, (c) β phase and (d) TiB particles. Each colour (gray scale for copy) is related to a specific orientation.

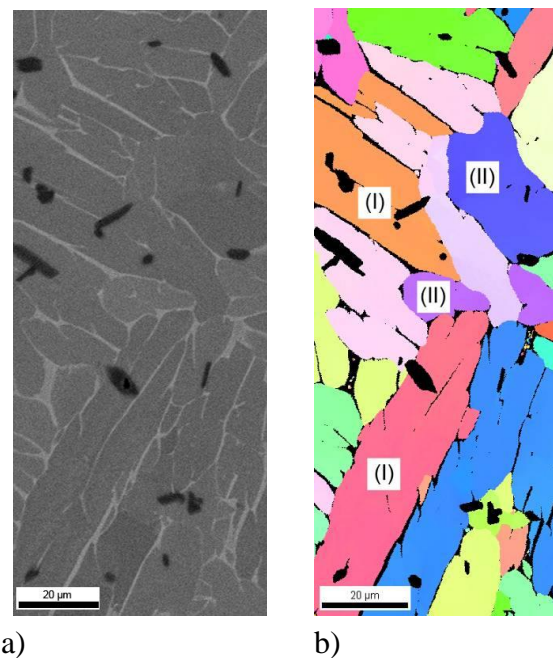


Fig. 80. High magnification EBSD phase map for Ti-6Al-4V-0.5B sintered at 1400 °C. (a) BSE image, (b) α phase.

Two more phases were investigated during the EBSD measurements: TiB and TiB₂. However, only the TiB phase (Fig. 79d) was indexed and no TiB₂ particles were identified. As can be seen in Fig. 81 relatively well defined Kikuchi patterns were obtained from the TiB particles.

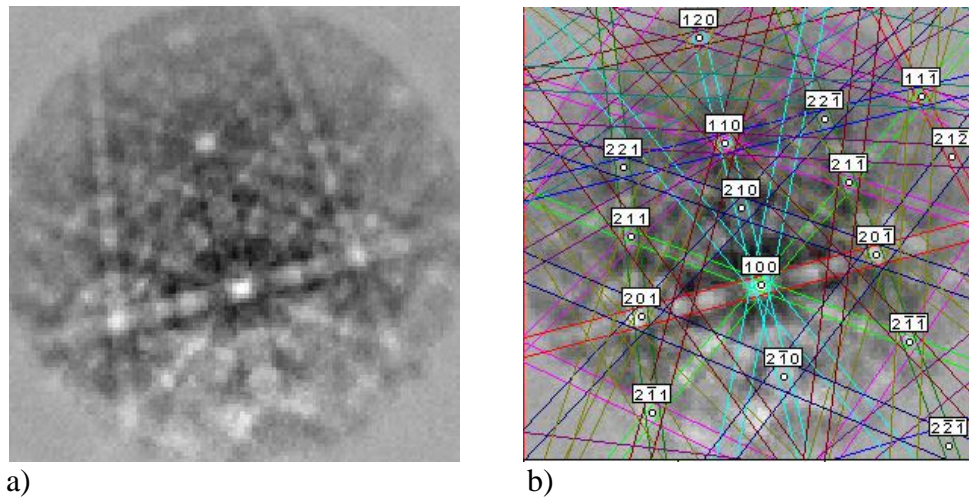


Fig. 81. Electron backscattered diffraction patterns obtained from TiB particles in Ti-6Al-4V-0.5B alloy. a) EBSD pattern, b) indexed EBSD pattern.

All the phases, including TiB particles, exhibit a texture free microstructure as illustrated in Fig. 82. The average grain size (for this microstructure the grain was assumed to be either an α colony or an α grain) measured is $18 \pm 5 \mu\text{m}$ which is a significant reduction compared to the $148 \mu\text{m}$ α colony size measured for the MIM35H samples.

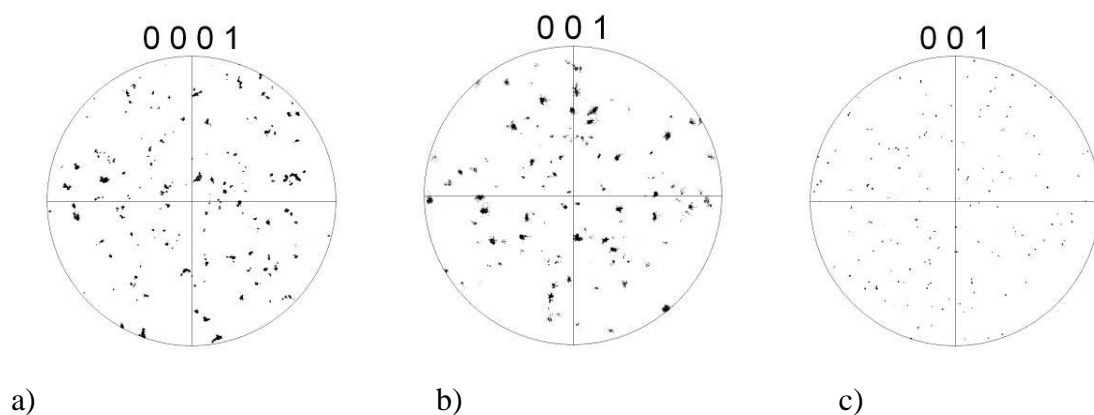


Fig. 82. Pole figures of the phases presented in Fig. 79. (a) α phase, (b) β phase and (c) TiB particles.

In order to provide more evidences of the influence of boron addition on the microstructure changes, a MIM Ti-6Al-4V sample without boron addition sintered at 1400 °C were submitted to the EBSD analysis. As illustrated in Fig. 83, the α phases and the β phases (β phases with the same orientation) are significantly larger than those of the samples with boron addition. The white phases in Fig. 83a represented the β phase and those regions should be presented in the mapping of β phases (Fig. 83c). Although the thinner β phases were not indexed for the Ti-6Al-4V sample, the β grains tend to be larger than the samples with boron addition, see Fig. 83c and Fig. 79c.

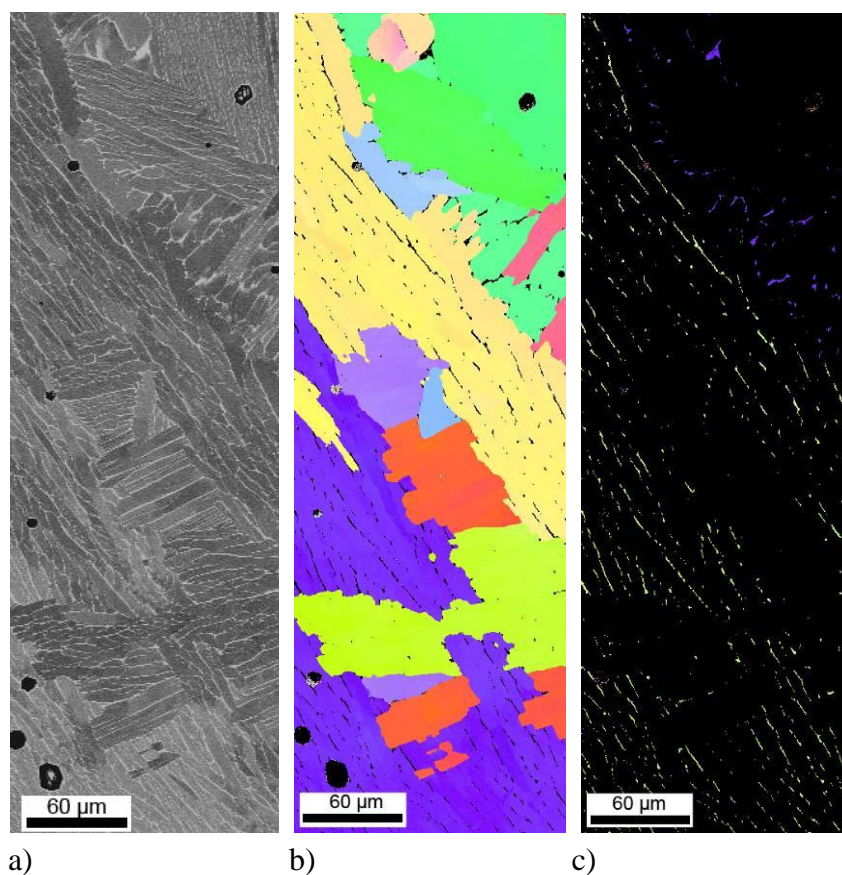


Fig. 83. EBSD phase map of Ti-6Al-4V sintered at 1400 °C: representation of the (a) BSE image, (b) α phase and (c) β phase. Each colour (gray scale for copy) is related to a specific orientation.

5.7.4. Tensile properties of the Ti-6Al-4V-0.5B alloy

The tensile behaviour of the Ti-6Al-4V-0.5B alloy is compared with the MIM35H in Table 15. A significant increase of yield strength and UTS is observed for the alloy with boron. On the other hand, the ductility decreases approximately by 2 %.

Table 15. Tensile properties of Ti-6Al-4V-0.5B and MIM35H.

Tensile property	Ti-6Al-4V-0.5B	MIM35H
Yield Stress [MPa]	787 ± 1	720 ± 2
Maximum Stress [MPa]	902 ± 3	824 ± 4
Elongation [%]	11.8 ± 1	13.4 ± 0.7

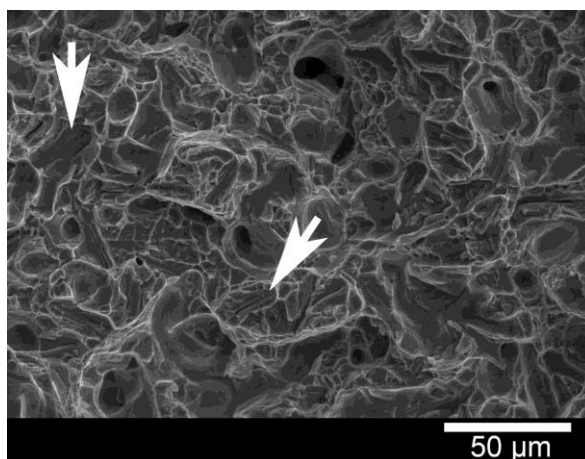


Fig. 84. Typical tensile fracture surface of Ti-6Al-4V-0.5B. Fine and coarse dimpled structures and pores are visible. Additionally, broken and debonded TiB particles are indicated by the white arrows.

The white arrows in Fig. 84 indicate broken TiB particles and interfacial decohesion between TiB particle and titanium matrix. Moreover, fine and coarse dimples with remaining porosity were typical features of the tensile fracture of Ti-6Al-4V-0.5B samples.

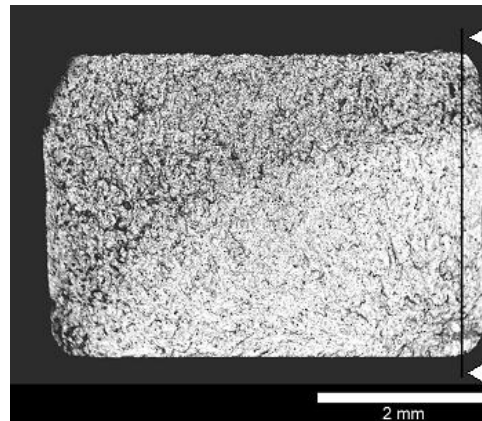


Fig. 86. Typical BSE micrograph of the fracture surface. The black line indicates the approximately position where the crack front profile (Fig. 88) was evaluated.

As can be seen in Fig. 87, the facets and pores were also observed in the possible crack nucleation location of Ti-6Al-4V-0.5B.

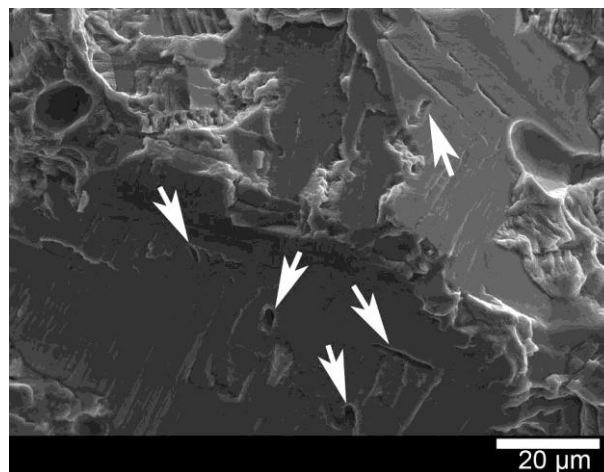


Fig. 87. Typical fracture surface of Ti-6Al-4V-0.5B with shot peening at the assumed crack nucleation site.

The apparent nucleation site is located inside of the sample instead of at the surface. Another interesting aspect of the crack nucleation location is the evidence of secondary crack formation and a possible interfacial decohesion (pull-out) between TiB particles and matrix as pointed out by the white arrows in Fig. 87.

The black line in Fig. 86 illustrates approximately the region where the crack front profile (Fig. 88) was carried out. The left side of Fig. 88 represents the lower right

corner of Fig. 86, which is the assumed crack initiation site. A higher magnification of the assumed crack nucleation region is illustrated in Fig. 89.

Crack propagation direction →

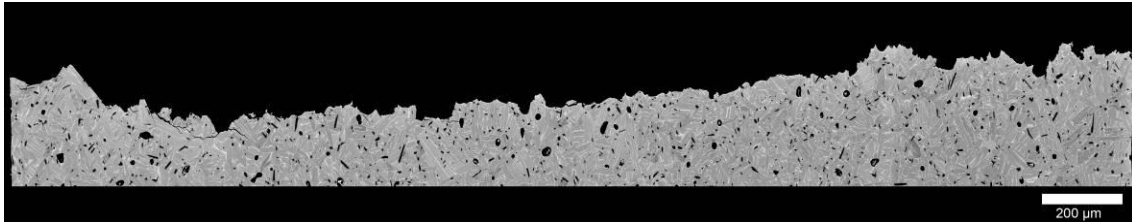


Fig. 88. Typical crack front profile of Ti-6Al-4V-0.5B samples

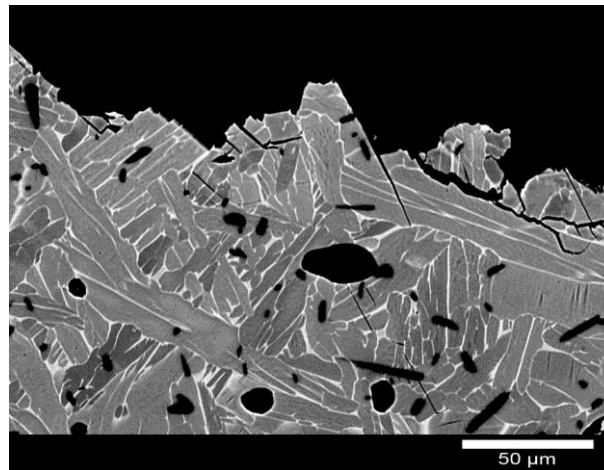


Fig. 89. High magnification of the crack front profile (Fig. 88). Directed at the assumed crack nucleation site.

Flat surfaces (indication of slip band fracture) and secondary cracks are typical features of the crack front profile near the assumed crack nucleation site. These features are not present on the right side of the crack front profile.

The micro cracks in Fig. 89 apparently were related to the presence of pores and TiB particles. Fig. 90 illustrated clearly the interfacial decohesion between the matrix and the TiB particles. Apparently, the crack propagated around the particles and no evidences of the eventual particle fracture were observed during this investigation.

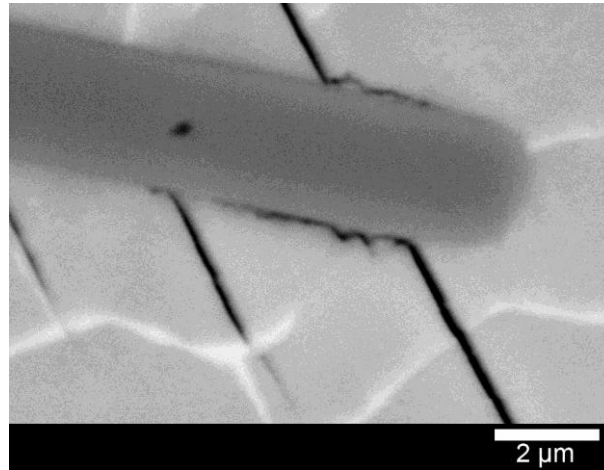


Fig. 90. Crack propagation interaction with TiB particle.

6. Discussion

In the following section, the relevant parameters that describe the fatigue behaviour of the MIM Ti-6Al-4V components are identified and evaluated. Based on the existent crack nucleation mechanism for the annealed wrought Ti-6Al-4V alloy and on the fatigued fracture surfaces analysis of MIM Ti-6Al-4V parts a crack initiation mechanism is proposed. As mentioned before, the qualitative influence of critical features such as surface quality, porosity and microstructure morphology is obtained by the following set of samples:

- Surface quality —→ samples with different binder content
samples with surface treatment (shot peening)
- Porosity —→ samples with different initial powder size
sintered MIM samples with additional HIP
- Microstructure morphology —→ samples fabricated from powder+HIP route
samples with boron addition

This experimental approach is evaluated in terms of its validation and limitations.

The last part focuses on the enhancement of the MIM Ti-6Al-4V fatigue behaviour. A desired microstructure is obtained by small addition of boron. The microstructure morphology changes and the required process parameters are discussed in detail.

6.1. The influence of interstitial elements on the mechanical properties of MIM samples

As described by Lütjering [103] the high cycle fatigue strength (resistance to crack nucleation) depends primarily on the resistance to dislocation motion, and therefore in most cases on the yield strength. A parameter that could influence the yield strength of the Ti-6Al-4V alloy is the concentration of interstitial elements in both α and β phases. Typical interstitial elements for the Ti-6Al-4V alloy are oxygen, carbon and nitrogen. These elements increase strength and decrease ductility [104]. Gysler and Lütjering [105] investigated the influence of oxygen equivalent on the yield strength of a wrought annealed and aged Ti-6Al-4V alloy with a lamellar microstructure. They observed an

increase in the yield strength from 800 MPa to 940 MPa by changing the oxygen equivalent from 990 $\mu\text{g/g}$ to 2390 $\mu\text{g/g}$, respectively. In a first approach, it is possible to assume that this relationship might be proportional, as suggested by Meester [16]. Therefore, for an increase of 100 $\mu\text{g/g}$ in the oxygen equivalent an enhancement in the yield strength of around 10 MPa is expected.

However, in the case of the MIM samples, the situation seems to be different. For the MIM31L and MIM31L* samples a variation of approximately 250 $\mu\text{g/g}$ did not promote any increase in the yield strength (see Table 2 and Table 3). This difference in the amount of interstitial elements between the MIM31L and MIM31L* samples is related to the process conditions. Although same process parameters are used to fabricate a specific set of samples, the samples processed at different sintering runs usually exhibited a variation in the amount of interstitial elements. Previous work performed at GKSS with the same process parameters applied for the fabrication of the MIM31L samples reported an oxygen equivalent value of 2069 $\mu\text{g/g}$ and a respective yield strength of 698 MPa. This result suggested that even a variation of approximately 800 $\mu\text{g/g}$ does not significantly affect the yield strength of the MIM Ti-6Al-4V alloy. Thus it is possible to propose that the observed variation of oxygen equivalent between the MIM samples promoted a minor influence on the yield strength and consequently on the fatigue behaviour. Most probably two factors contributed to the observed difference between MIM samples and the results reported by Gysler and Lütjering [105]: in the case of MIM samples the existence of pores and for the Gysler and Lütjering results the effect of annealed and aged microstructure condition.

As a result, predominant parameters that explain the mechanical properties of the studied materials are most likely the surface quality, the existence of residual compressive stresses, porosity and microstructure morphology rather than an interstitial alloying elements effect.

6.2. Ti-6Al-4V alloy processed by MIM

In this section the influence of the MIM process on the microstructural features and mechanical properties are discussed. Comparison between the MIM process results and

standard literature values for wrought annealed Ti-6Al-4V alloy with a lamellar microstructure is carried out.

6.2.1. Tensile properties

As illustrated in Table 3 lower tensile strength was observed for the MIM31L samples compared to wrought Ti-6Al-4V ELI (grade 23), here referred to as standard material. This behaviour is expected. Previous studies [7, 61, 106] reported similar values for tensile strength of Ti-6Al-4V components fabricated by MIM and obviously, this degradation of tensile property was related to the presence of the pores. Under tensile test, porosity reduces the effective load bearing cross-section area and acts as a stress concentration site for strain localization and damage, decreasing both strength and ductility [107]. Other features such as grain size and impurity levels were assumed to be of minor relevance compare to the porosity effect. As a matter of fact, the amount, shape and distribution of the pores are very important parameters in order to describe the mechanical properties of sintered materials [108]. For the MIM31L samples the volume percentage of remaining porosity was approximately 3.5%, meaning the porosity being most probably closed. For porous materials it is commonly accepted that the limit between open and closed porosity is around 5 vol.% as reported by several authors [107-111]. The porosity morphology exhibited in Fig. 22 for MIM31L samples contributes to the assumption of closed porosity, because another typical characteristic of a closed porosity is the fact that the pores are usually isolated and rounded [111].

It is expected that a closed porosity will not promote a severe degradation of the ductility [110] and indeed the elongation of MIM31L samples (Table 3) was greater than the minimal value tolerated for this alloy (10%). Additionally, the dimpled tensile fracture surface structure observed in Fig. 24 indicated that predominantly ductile fracture occurred.

6.2.2. Fatigue behaviour

A reduction of approximately 9 % is observed for the yield strength of the MIM31L samples compared to the wrought Ti-6Al-4V ELI (grade 23) alloy. A proportional reduction is expected for the fatigue strength; however, the results indicated that a degradation of approximately 39 % occurred.

The significant lower endurance limit of 350 MPa compared to 575 MPa of the standard material (Fig. 25) can be explained in terms of surface quality and crack initiation mechanisms. It is well known that surface quality can affect the fatigue behaviour of engineering materials dramatically [112]. As illustrated in Fig. 26 the surface of MIM31L samples exhibited notches. The presence of these notches can be related to injection and debinding steps of MIM processing. During injection, the sample surface is exposed to higher shear stress compared to the interior regions of the sample due to turbulence effects promoted by fluid (hot feedstock) and mould wall interaction. Such shear stress could promote local separation of binder/powder mixture. This separation leads to regions where only binder is present with no powder particles. Consequently, the notches are formed during thermal debinding and sintering in these specific surface regions due to missing particle powder contact. Another possibility is the fact that the powder particles, on specific surface sample regions after injection, could be surrounded by only one binder component of the binder system, e.g. paraffin. Therefore, during chemical debinding these particles will be removed together with the paraffin which leads to a local empty space.

Another result that supports the assumption that the notches are created during the injection and debinding processes is the fact that the maximum notch size observed on the fracture surface of MIM31L samples was around 100 μm , which was much larger than the maximum analysed pore size (approximately 33 μm , see Fig. 23).

These notches are, from the fracture mechanical point of view, cracks located directly on the samples surface. Consequently, the high cycle fatigue behaviour will be affected by the presence of such notches. Evidence of the presence of these notches on the assumed crack nucleation site of the MIM31L samples fracture surfaces is depicted in Fig. 28 and Fig. 30.

Crack initiation in a wrought Ti-6Al-4V alloy is invariably associated with the formation of facets [89]. The formation of such facets is related to the fact that the weak grains, favourably orientated for slip, generate a dislocation pile-up at the boundary with the neighbouring strong grain. The pile-up leads to the required combination of shear and tensile stresses on the unfavourably plane which induces facet formation. This mechanism was proposed for the first time by Stroh [88] describing the fatigue

behaviour of wrought Ti-6Al-4V alloy. Apparently the same mechanism holds for the MIM31L samples. The facets (region 1 in Fig. 28) are also presented together with the notches (region 2) on the assumed nucleation site. Another interesting feature near by the assumed nucleation site is the presence of secondary cracks, as illustrated in Fig. 30. It is important to note that the secondary cracks and an overall tortuous crack path (Fig. 29) are postulated features responsible for the superior crack growth resistance of the lamellar microstructure compared to e.g. bi-modal microstructure [113].

6.3. Influence of surface quality

As discussed in the section 6.2 the notches presented on the surface of the MIM31L samples are a determinant factor in order to describe the fatigue behaviour. Furthermore, the presence of these notches is most probably related to injection and debinding processes. The binder content is a critical parameter in order to describe the rheological behaviour of the feedstock during injection. Therefore, in one attempt to modify the surface quality the binder content was varied.

In order to facilitate the interpretation of the results Table 16 summarizes the variation of the factors assumed being relevant for the fatigue behaviour of the MIM components. A factor such as surface quality is ranked as bad (-), good (0) and very good (+). The existence of compressive stresses due to shot peening is labelled as (yes) or (no). Furthermore, grain size, porosity and impurity levels are represented as actual measured values for each set of samples.

Table 16. Selected samples for the evaluation of the surface quality influence.

Samples	Surface quality	Compressive stresses	Grain size [μm]	Porosity [%]	Oxygen Equivalent [μg/g]
MIM31L	-	no	97 ± 9	3.4	2598 ± 135
MIM31L*	-	no	100 ± 11	3.4	2850 ± 264
MIM35L	0	no	77 ± 10	5.7	2763 ± 90
MIM35H	0	no	148 ± 20	3.6	2969 ± 109

It is important to note that by changing process parameters usually more than one feature such as grain size, porosity or oxygen equivalent is influenced in some way. Consequently, it is extremely difficult to isolate their effect on the mechanical behaviour of sintered materials in general. The MIM31L and MIM35H samples are a typical example of such limitation. In order to obtain approximately the same level of porosity for samples with different surface quality a higher sintering temperature was applied. However, it was inevitable to avoid the coarsening of the microstructure.

6.3.1. Influence of the binder content

Microstructural features and tensile properties

The increase of the binder content from 31 vol.% to 35 vol.% promoted a decrease of the apparent density of the sintered samples (Table 4), if sintered at the same temperature. The porosity level of MIM35L samples was even slightly above the assumed boundary between open and closed porosity. As illustrated in Fig. 31 significant pore clusters were observed. Thus, most likely due to the presence of these clusters, large pores up to 86 μm were identified (Fig. 33). As a result of the high amount of pores, the MIM35L samples (Table 5) demonstrated poorer tensile properties compared to MIM31L (Table 3). However, the elongation was still above the minimum value tolerated for the wrought Ti-6Al-4V ELI (ASTM grade 23). Although large pores are presented on the tensile fracture surface of MIM35L samples (Fig. 35), a dimpled structure is also observed which is in agreement to the elongation values obtained for these samples.

On the other hand, the MIM35H samples, which were sintered at higher temperature (1350 $^{\circ}\text{C}$), displayed an amount of porosity similar to the MIM31L samples. This means that the larger initial particle distance was compensated by applying a higher sintering temperature. The increase of sintering temperature promoted an increase in α colony size due to the tendency of coarsening mechanism domination over densification mechanisms (Table 4). Another consequence of sintering at high temperature is the smaller maximum pore diameter for the MIM35H samples of around 46 μm (Fig. 34), which is a significant reduction compared to 86 μm of the MIM35L samples.

Usually the increase of grain size promotes a degradation of the mechanical properties. However, in this study the increase of α colony size observed in the MIM35H samples did not result in a decrease of strength or ductility (Table 5). As the MIM31L samples and MIM35H samples have nearly the same apparent density and impurity levels (Table 4), the higher tensile strength of the MIM35H samples has to be associated with some other effect involved by the higher sintering temperature. This effect overcomes the influence of grain size on mechanical properties as supported by the observed higher amount of “fine dimples” on the tensile fracture surface of MIM35H samples (Fig. 36) compared to MIM31L samples (Fig. 24). Even the MIM35L samples, sintered at low temperature, showed less fine dimples (Fig. 35). However, the exact mechanism behind the different amount of the fine dimples cannot be explained in the scope of the present investigation. A detailed investigation focused on dislocation concentration, low grain boundaries and possible preferential concentration of carbon or oxygen in the microstructure of the sintered samples needs to be performed to elucidate this phenomenon.

Nevertheless, the presence of these dimples on the tensile fracture surface of Ti-6Al-4V alloy without pores has been reported on the literature before [114, 115]. The dimensions of the dimples shown in those investigations are in the same range as those observed in this study for MIM35H samples, here referred to as “fine dimples”. In contrast, for Ti-6Al-4V alloy produced by MIM and sintered at 1250 °C, Zhang et al. [116] proposed as the typical ductile dimple structure a surface similar to the fracture surfaces of the MIM31L and MIM35L samples, here referred to as “coarse dimples”. Even if such a coarse structure is also present in the fracture surface of MIM35H samples (region inside the white ellipse in Fig. 36), its occurrence is much less pronounced. Therefore, as mentioned before, the maximum sintering temperature seems to be a critical factor for increasing the “fine dimples” structure in the tensile fracture surface.

Fatigue property

Several authors [109, 110, 117-119] assumed that the fatigue resistance of powder metallurgy materials is mainly controlled by porosity. However in terms of porosity, it

is not possible to explain the fatigue behaviour difference of MIM31L and MIM35H samples since the amount of porosity is almost identical for the two configurations (Table 4). Furthermore, even the grain size difference between the two configurations cannot explain the fatigue behaviour difference, since the relatively coarser microstructure exhibits the higher fatigue resistance. Therefore, other mechanisms have to be taken into account to cause such behaviour. One possible explanation is the fact that fatigue behaviour is very sensitive to surface quality, especially under bending conditions. As it can be seen in Fig. 26 (MIM31L), Fig. 38 (MIM35H) and Fig. 39 (MIM35L) the surface quality appears to be different in terms of surface roughness. It is clear to see that a higher content of binder promotes a better surface quality for the injected samples. The explanation for such behaviour is most likely related to the lower viscosity of the feedstock when higher binder content is used. As a consequence, during injection the powder particles in the feedstock with the higher amount of binder are able to fill a possible surface defect more easily.

Fractography of fatigued specimens revealed the possible region for the crack nucleation of MIM35L (Fig. 40) and MIM35H (Fig. 41). The maximum observed size of the notches located at the surface of the samples was approximately 50 μm . Notches are well known to exhibit a negative influence on the fatigue properties [120, 121], thus, the differing results in fatigue resistance of MIM31L compared to MIM35L and MIM35H could be related to surface roughness differences.

Another possible explanation for the higher fatigue strength of MIM35H compared to MIM31L is the influence of the sintering parameters on the mechanical properties. As discussed before, the increase of maximum sintering temperature results in an improvement of the tensile properties together with an apparently higher presence of fine dimples on the tensile fracture surface. Results presented by Hadrboletz and Weiss [108] for Fe-2C-2.5Ni samples made by powder metallurgy showed that fatigue strength increases when a more intensive sintering process (higher temperature, longer sintering time) has been chosen.

The MIM35L samples apparently achieved a fatigue behaviour similar to that of the MIM35H samples (Fig. 37). This result is unexpected since the MIM35L presented higher porosity and poorer tensile properties (Table 5). However, it is possible to

explain this behaviour with Fig. 31, which illustrates that the MIM35L samples exhibit a finer microstructure when compared to MIM35H (Fig. 32). It is well known that a refinement of the microstructure leads to an increase of the high cycle fatigue resistance [86, 122]. In fact, refinement of the microstructure means reduction of the slip length and, consequently, reduction of the number of dislocation pile-ups at critical preferential locations for crack nucleation as e.g. pores and grain boundaries.

Furthermore, Fig. 37 shows that MIM35L samples exhibit also a better fatigue behaviour than MIM31L samples. This behaviour is expected since as illustrated in Fig. 39 and Fig. 26, the MIM35L samples present smaller surface defects than MIM31L samples. Obviously, a better surface quality compensate for the negative influence of porosity with respect to high cycle fatigue behaviour. Although pores with a diameter of approximately 90 μm were observed in the interior of the MIM35L samples (Fig. 33), the maximum observed size of the notches located at the surface was only approximately 50 μm (Fig. 40). This is a clear indication that for the fatigue behaviour amount and size of the pores, within the range observed in this study, is not the most critical factor. In contrast, as indicated in Table 5, for the tensile properties amount, size and distribution of the porosity are the determinant parameters.

6.3.2. Influence of shot peening

As a surface treatment shot peening was applied in order to modify the surface quality without affecting microstructural features such as grain size, porosity and impurity levels. Table 17 illustrates the selected samples for the evaluation of the shot peening influence.

The application of shot peening (SP) promotes a better surface quality and introduces residual compressive stresses. In order to separate the relevance of these parameters the MIM35H+SP and MIM35H+SP+HT samples are compared. In the following the influence of different surface quality and existence of residual compressive stresses on the fatigue behaviour of MIM components are discussed in terms of microstructural features and fracture surface analyses.

Table 17. Selected samples for the evaluation of the shot peening

Samples	Surface quality	Compressive stresses	Grain size [μm]	Porosity [%]	Oxygen Equivalent [$\mu\text{g/g}$]
MIM31L	-	No	97 ± 9	3.4	2598 ± 135
MIM35H	0	No	148 ± 20	3.6	2969 ± 109
MIM31L+SP	+	Yes	97 ± 9	3.4	2598 ± 135
MIM35H+SP	+	Yes	148 ± 20	3.6	2969 ± 109
MIM35H+SP+HT	+	No	150 ± 19	3.6	2673 ± 152

Fatigue behaviour

The shot peening promoted a significant improvement of the surface quality for the MIM31L and MIM35H samples as illustrated in Fig. 44 and Fig. 45, respectively. This is mainly due to the fact that the shot peening process leads to a local plastic deformation which practically removes the notches and promotes residual compressive stress. Consequently, higher endurance limit was achieved for the samples exposed to shot peening as shown in Fig. 42 and Fig. 43. It is important to note that for almost all samples the crack initiated at a location inside the samples instead of at the surface (see Fig. 46 and Fig. 47), except for the samples marked with parentheses in Fig. 42. In these samples, the local plastic deformation promoted by shot peening application was not sufficient to close the surface defects. Most probably, there is a critical shape and size of the surface defect that limits the shot peening benefit. As can be seen in Fig. 48 the crack initiated at the surface instead of the inner region. Therefore, the fatigue life of these samples is closer to that of the MIM31L samples without shot peening.

Internal fatigue origins are not common, however after shot peening application, it is frequently encountered in titanium alloys [11, 99, 100]. Subsurface crack initiation sites in fully lamellar Ti-6Al-4V alloy were related to cross-colony slip-band fracture [123]. This fracture behaviour is also presented in the fracture surface of MIM samples with shot peening. The crack is supposed to nucleate at the intersection of two slip bands, as indicated by the white arrow in Fig. 47b. Apart from the cross-colony fracture facets, the presence of pores is another origin of the crack nucleation in MIM samples. In this

investigation, the fracture surface of MIM samples with shot peening always exhibited both features (pores and cross-colony fracture facets) present at its nucleation site.

As observed for the samples without shot peening, an overall tortuous crack path (Fig. 49) and secondary cracks (Fig. 50) were also presented for the samples with shot peening. In fact, the application of shot peening moves the crack initiation site from the surface to a subsurface level, mainly due to the existence of compressive residual stresses (local plastic deformation). However, it is possible to assume that approximately the same mechanism, formation of facets, for the crack nucleation occurred. Instead of dislocations pile-up at a notch located at the surface which is the assumed mechanism of the samples without shot peening, for the samples with shot peening the pile-up of the dislocations took place most likely in a pore located in a subsurface level.

Influence of the residual stress promoted by the shot peening

As intended, most probably the heat treatment at 915 °C relieved the residual compressive stresses and due to that the fatigue resistance for the MIM35H+SP+HT samples tends to decrease as illustrated in Fig. 52. Furthermore, the facets at the assumed crack nucleation site for these samples are located closer to the surface indicating a crack initiation in the surface instead of subsurface level (Fig. 53). As reported by several authors [11, 12, 99, 101, 102, 124, 125], the presence of residual compressive stresses is assumed to be mainly responsible for the subsurface crack nucleation and subsequent increase of the high cycle fatigue behaviour. Such assumption is also made in the present work in order to interpret the obtained results for the MIM35H samples. However, it is important to note that the improvement of the surface quality promoted by the shot peening application also contributes to the increase of the fatigue behaviour, especially in the case of MIM31L samples.

As a second point, the heat treatment could promote a refinement of the microstructure at a subsurface level. However, as illustrated in Fig. 51 the desired refinement of the microstructure did not occur. This is probably related to the fact that the amount of dislocations created by the local plastic deformation during shot peening was not high enough to promote the nucleation of new grains during the heat treatment process. Gray

et al. [101] reported that mechanical surface treatment combined with a subsequent recrystallization was successfully applied for Ti8.6Al and Ti-6242 alloys. They were able to reduce approximately five times the average grain size of the near surface. Several factors as annealing temperature, isotherm time, cooling rate, shot peening pressure and material used for the shot peening could have contributed for the unsuccessful recrystallization of the MIM35H samples. However, among these parameters, most probably the main factor responsible for this behaviour is the relatively low shot peening pressure used in this investigation (around 4 bar).

6.4. Influence of the porosity

The degradation of the mechanical properties due to the presence of the remaining porosity in the MIM components was investigated. In order to obtain different porosity levels two different routes were applied: 1. using a smaller powder particle size and 2. addition of a HIP process. In the following the results are discussed. As for the previous section, Table 18 illustrates the samples selected to perform this investigation.

Table 18. Selected samples for the evaluation of the porosity influence.

Samples	Surface quality	Compressive stresses	Grain size [μm]	Porosity [%]	Oxygen Equivalent [$\mu\text{g/g}$]
MIM35H+SP	+	Yes	148 ± 20	3.6	2969 ± 109
25MIM35L+SP	+	Yes	150 ± 23	2	3295 ± 72
MIM35H+HIP+SP	+	Yes	174 ± 26	0	3023 ± 32

6.4.1. Influence of the particle size

High binder content (35 vol.%) was used for the production of 25MIM35L samples. Two reasons contributed to the utilization of the higher binder content: the first one is related to the possibility to decrease the surface size defect and the second one is the fact that smaller particles tend to promote an increase in the viscosity of the feedstock mainly due to the increase of surface area [126]. In one attempt to obtain a porosity level below the values achieved for the MIM31L or MIM35H samples without having a significantly coarsening of the microstructure, the 25MIM35L samples were sintered at

1250 °C. As shown in Table 7 and Table 18 the 25MIM35L samples exhibited lower porosity level and similar grain size compared to MIM35H samples. This occurred due to the fact that the driving force for sintering is the reduction of surface energy. The surface energy per unit volume depends on the inverse of the particle diameter; thus, finer particles increase the driving force. Consequently, it is possible to achieve higher density using lower temperature and less time [127].

Another effect that is probably related to the finer particles is the slight increase of the impurity levels, especially related to carbon and oxygen content (Table 7). Nevertheless, as discussed in the section 6.1 such a variation is assumed to be of minor relevance in terms of mechanical properties. In fact, the significant improvement of the tensile properties is most probably related to the lower porosity size (Fig. 55) and porosity level (Table 7) compared to MIM35H samples.

Fatigue behaviour

The 25MIM35L samples exhibited a slight improvement of the fatigue behaviour compared to MIM35H samples (Fig. 56). Obviously, the smaller amount of pores is the probable reason to explain the observed increase of the fatigue resistance. Additionally, another factor that may contribute is the fact that the 25MIM35L samples tend to exhibit smaller pores diameter (Fig. 55) than MIM35H samples (Fig. 34).

As can be seen in Fig. 57 and Fig. 58, again facets and pores were present on the crack nucleation site of the 25MIM35L fatigued fracture surface. This, as discussed in the previous sections, is a further indication that the mechanism that describes the crack nucleation is the dislocation pile-up at critical points (grain boundaries, pores, particles, etc).

6.4.2. Influence of the HIP process

The MIM35H sample configuration was chosen due to the fact that the quality of the sintered surface was much better than that of the samples with a lower binder volume fraction e.g. MIM31L. Furthermore, the amount of remaining porosity for the MIM35H was approximately 3.6%. In this investigation this value is assumed to be a typical and sound porosity level for the components processed by MIM technology.

The additional exposure of the MIM35H samples to a relatively high temperature during the HIP processing did not promote a subsequent increase of the impurity levels (Table 8). Consequently, the difference in the mechanical properties can be attributed to existence of pores and grain size difference.

Tensile properties

The significant improvement of the tensile properties of the MIM35H+HIP samples compared to MIM35H samples is related to the elimination of the porosity. This effect overbalances the detrimental larger grain size of the samples with HIP (Fig. 59 and Table 8). It is important to note that even small and round pores exhibit associated stress concentration which influence the tensile mechanical behaviour.

The tensile fracture surface of the MIM35H+HIP samples (Fig. 60) exhibits a well defined dimpled structure, which is in agreement to the high values obtained for the tensile elongation (Table 9). Contrary to the MIM35H samples only fine dimples are visible. This indicates that the “coarse dimples” are most likely related to the existence of remaining porosity.

Fatigue behaviour

The significant increase of the yield stress of approximately 17 % was not completely observed for the fatigue behaviour; in fact, the improvement of the endurance limit was only around 11 % (Fig. 61). The fatigue fracture surface illustrated in Fig. 62 and Fig. 63 suggests that, as for the other configurations exposed to shot peening, the crack initiated at subsurface level. Another similarity of the fracture surfaces of MIM35H and MIM35H+HIP samples was the presence of the facets. This indicates that most likely again the mechanism responsible for the crack nucleation was the pile-up of dislocations at a critical point. Instead of pores as a critical point, the features presented in Fig. 64 suggest that an oxide particle could have acted as a barrier for the dislocation motion. The results presented in Table 10 confirm that the region pointed to by the arrow (a) in Fig. 64 exhibited a higher concentration of oxygen than the region pointed by the arrow (b) in Fig. 64. This is one indication that with the absence of porosity the next defect class acts as the determinant factor for the fatigue behaviour, which in this case is the

oxide particle. Avoiding foreign particles completely is nearly impossible in powder metallurgy.

It should be recognised, however, that no other element apart from titanium, aluminium, vanadium and oxygen were identified in the rich oxygen region of the fatigued fracture surfaces. The possibility of titanium oxide particles existence in the MIM Ti-6Al-4V is very low. The Ti-O binary phase diagram shows that oxygen has a large solubility (over 30 at.%) in low-temperature titanium and assuming that Ti-6Al-4V exhibits approximately the same trend the oxygen should be soluble in the matrix especially after sintering under vacuum and temperatures above 1250 °C. Nevertheless, as reported in section 5.6 magnesium oxide particles appear to be a typical powder contamination. These particles are not dissolved under the applied HIP conditions (maximum temperature of 850 °C and a pressure of 200 MPa). However, in the case of MIM samples, it is not clear what will happen with these particles. Based on available thermodynamic data, it is unlikely that these particles will dissolve at higher temperature, e.g. at 1250 °C. Therefore the enhanced oxygen content remains unclear.

6.5. Influence of the microstructure morphology

In order to achieve a finer microstructure, samples were consolidated from powder below β transus temperature by applying a HIP process. The influence of finer microstructure on the mechanical properties of the Ti-6Al-4V alloy produced by powder metallurgy route will be discussed in the following. Table 19 lists the samples used for the estimation of the grain size influence on the fatigue behaviour.

Table 19. Selected samples for the evaluation of the grain size influence.

Samples	Surface quality	Compressive stresses	Grain size [μm]	Porosity [%]	Oxygen Equivalent [$\mu\text{g/g}$]
MIM35H+SP	++	+	148 \pm 20	3.6	2969 \pm 109
Powder+HIP+SP	++	+	9 \pm 5	0	2280 \pm 207
MIM35H+HIP+SP	++	+	174 \pm 26	0	3023 \pm 32

6.5.1. Microstructural features

As illustrated in Fig. 65 and Fig. 66 the Powder+HIP samples exhibited a relatively fine microstructure. The microstructure morphology resembles a typical equiaxed microstructure with some region containing a very fine lamellar structure. This is mainly related to the fact that the process was carried out below β transus temperature. After handling and HIP processing a moderate increase of the impurity levels was observed, especially related to oxygen level (Table 11). However, this level was still lower than the minimal levels obtained for the MIM samples.

6.5.2. Tensile properties

As mentioned in 3.5.4 the tensile properties of the Powder+HIP samples were characterized by using micro-tensile specimen. It is well known that the miniaturization of tensile specimen causes so-called “size effects” [128-131], which lead to different material behaviour in the micro scale compared to the macro scale. Kals et al. [128] found out that the proportion of grain size versus sheet thickness plays an important role in the tensile properties. With respect to plastic deformation, grains located at the specimen surface and grains located within the specimen volume are expected to behave differently. This difference is connected to the fact that the presence of a free surface strongly reduces the constraints on the grains near the surface, and consequently, the grains will be deformed at substantial lower stress. The behaviour of the grains located at the free surface becomes more and more dominant with the reduction of the specimen size. To the author’s knowledge no relationship between thickness and grain size was established for the Ti-6Al-4V alloy; however, in e.g. ferrous materials the size effect was observed for samples with thicknesses smaller than about 6 to 10 times the average grain size [130]. Consequently, based on the results for ferrous materials, the size effect is expected to occur for the MIM35H samples since only few grains are present along the thickness of the micro-tensile specimens (thickness = 500 μm). This correlates to the results illustrated in Table 12. The micro tensile specimens exhibited poorer tensile properties than the dog-bone samples. However, in terms of tensile fracture surface no significant difference was observed between the dog bone samples (Fig. 36) and micro-tensile specimens (Fig. 68).

The Powder+HIP samples exhibited significantly better tensile properties than the MIM35H samples of same geometry. Furthermore, this is even valid compared to the MIM35H dog-bone shaped samples. Such behaviour is most probably related to the size effect and the positive effect of microstructure refinement on the tensile properties. Furthermore, a larger scatter especially of the elongation was also observed. This behaviour is most probably related to the fact that particles were found in the fracture surface of the samples exhibiting lower elongation (Fig. 67a). These particles were not identified on the samples with higher elongation (Fig. 67b). This could be an indication that the amount of these particles is relatively small.

6.5.3. Fatigue behaviour

As for the tensile tests the fatigue results of the Powder+HIP samples exhibited a larger scatter than those of the MIM samples (Fig. 69). Such behaviour is most probably related to the presence of particles at the assumed crack nucleation size as demonstrated in Fig. 70 and Fig. 71. The size and location of these particles varied among the samples, which might be the explanation for the observed larger scatter. The particle shown in Fig. 71 displays a higher concentration of magnesium and oxygen (Table 13). The particles observed on the fatigued fracture surface apparently are the same of those presented on the tensile fracture surface. The presence of such a particle can be related to:

- typical contamination of the material used to do the atomization process or
- handling of the powder.

It is important to note here that the Powder+HIP samples were processed twice. This means that two different charges from Ti-6Al-4V ELI powder were used. This extra experiment was performed in order to evaluate a possible contamination during handling of the powder prior the HIP processing. The two sets of samples exhibited always such particles on the fatigued fracture surface. This indicates that most likely these particles are a common contamination of the powder.

Most probably these particles (impurities) are also present in the MIM samples. However, it was not possible to identify such particles on the fatigued fracture surface of the MIM samples. This could be related to the fact that other defects such as pores are more relevant to the crack initiation mechanisms than the particles. Another

argument that contributes to this assumption is the fact, that even the fatigued MIM35H+HIP samples exhibited a contaminated region at the assumed crack nucleation site (Fig. 64). Thus, with the elimination of the porosity the next defect class appears to be the determinant factor for the crack nucleation, here being the presence of small oxide particles.

As reported by Froes et al. [27] the endurance limit of the Ti-6Al-4V pre-alloyed powder after HIP processing is in the range of 400 MPa to 600 MPa. Testing conditions were axial loading with stress ratio of 0.1 and use of smooth samples. The value obtained for Powder+HIP samples is above this range probably due to the shot peening application. Consequently, it is possible to assume that the oxide particles found on the crack initiation sites are a typical impurity feature related to the powder metallurgy processing. Thus, the value obtained in this study for the endurance limit is in agreement to the literature.

Finally, it is important to highlight that in spite of the observed foreign particles the high cycle fatigue limit was much higher than that of the MIM35H and MIM35H+HIP samples. The main reason for this is assumed to be the grain size and the microstructure morphology differences among the investigated configurations. As described by Miller and O'Donnell [132] high cycle fatigue resistance of a material is enhanced if a large number of barriers is placed in the path of a growing microscopically short crack. The misorientation of the slip systems of neighboured grains is one of the most effective barriers. Consequently, due to more barriers per unit area, a small grain size material has a greater fatigue resistance than a large grain size material.

6.6. Enhancement of the high cycle fatigue behaviour of the MIM components by microstructure design

As described in this investigation and in the literature [86, 103], the grain size is a determinant factor regarding the high cycle fatigue behaviour of a material. The addition of boron on the MIM Ti-6Al-4V alloy was performed with the objective to obtain a finer microstructure. In this section, the influence of the boron addition on the

Ti-6Al-4V alloy will be discussed in terms of microstructural features and mechanical properties.

6.6.1. Variation of boron content

As a preliminary investigation the samples with different boron additions were sintered at 1250 °C. With the addition of 0.1 wt.% of boron, the α colony size was reduced to approximately 80 μm compared to MIM31L (around 100 μm). Such a phenomenon can be related to the TiB particles (the particles in the form of needles in Fig. 73) influence on grain coarsening. Komizo et al. [133] demonstrated by using high-temperature laser scanning confocal microscopy that TiB particles act as a barrier for β grain growth at high temperatures. However, it is important to note that the lamellar microstructure is still the predominant microstructure morphology in Ti-6Al-4V-0.1B. In contrast, the samples with 0.5 wt.% of boron addition exhibited a microstructure with no defined α colony: in other words, the lamellar structure is almost totally suppressed (Fig. 74).

Another important microstructural feature is the porosity. The addition of 0.1 wt.% and 0.5 wt.% of boron promoted a decrease in the relative densification (Table 14). This is a clear indication that the formation of TiB particles affects the sintering behaviour of the Ti-6Al-4V alloy. On the other hand, the negative influence of boron addition in terms of porosity was not observed for samples sintered at 1400 °C. In this case samples with boron addition exhibited even higher densification level than samples without boron (Fig. 75). Therefore, a better understanding of the sintering process of the Ti-6Al-4V alloy powder with added amorphous boron powder is required. One technique that is very helpful in describing the evolution sintering process is dilatometry.

6.6.2. Sintering process

The addition of boron in the Ti-6Al-4V shifted the start temperature of the shrinkage process by almost 110 °C as illustrated in Fig. 76a. As stated by German [127] the shrinkage of the powder compact is a result of a change in the interparticle spacing as neck growth takes place which is promoted by bulk transport processes. Consequently, based on the results of the dilatometry experiments it is possible to argue that the boron causes a delay of the bulk transport processes responsible for the shrinkage of the

powder compact. Therefore due to the presence of boron the sample starts to shrink only at 722 °C rather than 614 °C. It is important to note that the pre-sinter of the samples with and without boron addition was carried out in a single furnace run. No temperature difference between the samples is expected since they were positioned very close to each other. Thus it is possible to attribute the delay of the sintering process to the presence of boron.

Another interesting behaviour of the samples with boron addition is the fact that the sample progressively increased the linear shrinkage rate (LSR) from 722 °C up to 820 °C (Fig. 76b). After this temperature the LSR decreased until approximately 1050 °C. This phenomenon can be related to the formation of TiB particles. For this formation a solid diffusion process needs to take place between boron from amorphous boron powder and titanium from Ti-6Al-4V alloy powder. Divinski et al. [134] investigated the tracer diffusion of boron in pure α -Ti by secondary ion mass spectroscopy using the stable ^{11}B isotope. They observed that at temperatures below 760 °C, diffusion profiles of acceptable quality could no longer be measured, probably due to the low solubility of boron in α -Ti. On the other hand, they reported that boron is the fastest diffuser in α -Ti after hydrogen. Therefore, it is reasonable to assume that most probably the TiB particles are formed above 760 °C. The dilatometry experiment suggests that the TiB formation occurred above 820 °C which is in a good agreement to the values obtained by Divinski et al. [134].

It is well known [135-137] that TiB particles can restrict grain growth of cast Ti-6Al-4V alloy. By extension of this concept it can also be assumed that the initial and intermediate sintering stage can be inhibited by the presence of TiB particles as well.

The Ti-6Al-4V alloy exhibited a maximum LSR of 0.25 %/min at approximately 985 °C. Above this temperature the LSR started to decrease which is an indication of the final sintering stage's initiation. For most materials, it is common that a separation of grain boundaries and pores occurs, leaving the pores isolated in the grain interior at final sinter stage process [127]. This leads to coarsening of the microstructure, and further elimination of the porosity (further densification) becomes difficult since lattice

diffusion, which is much slower than grain boundary diffusion, is needed for elimination of the pores.

On the other hand, the Ti-6Al-4V-0.5B alloy started to shrink significantly above 1050 °C. The maximum LSR achieved for this alloy during dilatometry experiments was approximately 0.45 %/min at around 1250 °C. It is important to note that the maximum LSR for Ti-6Al-4V-0.5B was roughly two times higher than for the alloy without boron addition. This behaviour can be explained in terms of densification and coarsening processes. As pointed out before, the presence of TiB particles decreases the grain growth. Consequently, a separation of pores and grain boundaries might be delayed. This leads to an optimum configuration for the elimination of pores by grain boundary diffusion [138].

In fact, the addition of boron to a Ti-6Al-4V alloy results in a delay of the bulk transport processes responsible for the shrinkage of the powder compact. Most probably due to the formation of TiB particles the shrinkage process is retarded from 820 °C up to 1050 °C. This delay of densification occurred due to the pinning effect promoted by the presence of TiB particles. Such a pinning effect is beneficial for the densification at a later stage's of sintering process due to postpone separation of pores and grain boundaries which extended the elimination of the pores by grain boundary diffusion.

6.6.3. The microstructure of Ti-6Al-4V-0.5B alloy sintered at 1400 °C

As described before, the α colony size is not well defined for the Ti-6Al-4V-0.5B samples (see Fig. 77 and Fig. 79) which can be related to a tendency to form equiaxed α instead of the lamellar structure. Such behaviour was also reported in the work of Hill et al. [139] for cast Ti-6Al-4V alloy with a small addition of boron. They obtained the equiaxed microstructure after additional heat treatment with slow cooling from above the β transus without being subjected to any thermo-mechanical treatment in the $\alpha + \beta$ phase field (a typical procedure to create globular microstructure of $\alpha + \beta$ titanium alloys). They suggested that α nucleating at and growing from the TiB precipitates usually results in equiaxed or globular morphology.

Tamirisakandala et al. [94] also tried to describe the mechanism responsible for the microstructure refinement of the cast Ti-6Al-4V with a small additions of boron. In their study, the refinement of the microstructure was explained by three mechanisms: refinement of β -grains, the heterogeneous α nucleation and grain growth restriction. The β -grain refinement was related to the influence of boron partitions ahead of the titanium solid/liquid interface. In hypoeutectic Ti-B alloys the β_{Ti} grains are formed prior to the precipitation of TiB particles. Therefore, TiB particles cannot be nucleation sites for the β_{Ti} grains. More recently, Bermingham et al. [137] described similar observations for cast commercially pure titanium with a small addition of boron. The second mechanism, the heterogeneous α nucleation, is related to the influence of TiB particles on the nucleation of α phase. They suggested that the presence of TiB particles enhanced the kinetics of phase transformation from β to α , which occurs by nucleation and growth according to Burger's orientation relationship, by providing additional nucleation sites. As a consequence of these additional nucleation sites a microstructure with equiaxed α grains is more likely to occur than the lamellar microstructure. Finally, the grain growth restriction mechanism is related to the pinning effect promoted by the TiB particles on grain growth. This mechanism for cast materials is assumed to be relevant during subsequent thermal exposure at elevated temperatures by restricting the mobility of grain boundaries.

It is important to note that the refinement of β -grains mechanism is not likely to occur for the sintered MIM Ti-6Al-4V-0.5B samples since no liquid phase is expected to be present during the sintering process. Nevertheless, as for the cast Ti-6Al-4V alloy with a small addition of boron, the heterogeneous α nucleation is a relevant mechanism in order to describe the microstructure changes of the MIM Ti-6Al-4V-0.5B samples after sintering. Although the grain growth restriction is assumed to be a secondary microstructure refinement mechanism for cast Ti-6Al-4V alloy with a small addition of boron, for the MIM samples this mechanism is significantly relevant for the sintering process and for the final microstructure.

For the Ti-6Al-4V-0.5B alloy both α colonies and α grains were assumed to define the grain size (slip length) because both features exist in the microstructure. Fig. 80b shows

regions (I) where α lamellae are oriented in the same direction, setting up a colony. However, also regions (regions II) can be observed where neighbored single α phases have no correlated orientation. These regions are considered as single grains. A lower magnification mapping of the α phase orientation (Fig. 79b) confirms the existence of both small α colonies and α grains. The microstructure of the samples with 0.5 wt.% of boron addition can be considered as a transition between lamellar and equiaxed.

In addition, it was possible to clearly identify the β phase between α lamellae and at grains boundaries (Fig. 79c). The β grain size of the samples with boron addition, apparently, is smaller than that of samples without boron (Fig. 83c). This is an indication that the TiB particles act as a barrier to grain growth of β grains.

Three boron compounds exist in the Ti-B system: TiB, Ti₃B₄ and TiB₂. These occur at boron concentrations of about 18%, 22%, and 30% by weight, respectively. Feng et al. [140] stated that only TiB can be in situ synthesized from the reaction between Ti powder and boron powder. In this investigation, during the EBSD experiments, only the TiB phase (Fig. 79d) was indexed and no TiB₂ was observed for the Ti-6Al-4V-0.5B alloy. This is in agreement with thermodynamic expectation [141-145] and with the Feng et al. [140] statement.

Another interesting aspect of the Ti-6Al-4V-0.5B alloy microstructure produced by MIM technology is the apparent homogeneous distribution of the TiB particles. This is a clear advantage of the MIM process over the cast process. As reported by Srinivasan et al. [146], the cast Ti-6Al-4V alloy with a small addition of boron (0.1 wt.%) tends to exhibit a microstructure with TiB precipitated at the grain boundaries. This preferential precipitation at the grain boundaries promotes a degradation of mechanical properties, especially with respect to ductility.

6.6.4. The tensile property of Ti-6Al-4V-0.5B alloy sintered at 1400 °C

As reported in the literature [147, 148] the TiB particles tend to deteriorate the ductility of Ti-6Al-4V alloy. Such behaviour was also observed for the Ti-6Al-4V-0.5B samples produce by MIM (Table 15). However, the level of this expected reduction was rather moderate (around 2 %). As illustrated in Fig. 84 a typical ductile tensile fracture with

the presence of fine dimples, coarse dimples and pores occurred for the Ti-6Al-4V-0.5B samples, being in agreement to the low reduction of tensile elongation. Although a significant improvement occurred due to the boron addition, the tensile properties are still inferior to those of the samples without pores (MIM35H+HIP, Table 9). This is a clear indication that the influence of porosity on the tensile behaviour of MIM components is greater than the influence of grain size or microstructure morphology.

Another relevant parameter is the maximum sinter temperature. Since the samples with boron were sintered at higher temperature, it seems possible to attribute the increase of strength and the decrease of ductility to a possibly higher impurity level. However, as can be seen in Table 14, impurity levels for the alloy sintered at 1400 °C are in the accepted variation range and as discussed in section 6.1 no significantly influence on the mechanical properties is expected.

6.6.5. Fatigue behaviour of Ti-6Al-4V-0.5B alloy sintered at 1400 °C

The addition of boron in the Ti-6Al-4V alloy promoted a significant improvement of the fatigue behaviour. The endurance limit was approximately 640 MPa. Even the MIM35H+HIP samples exhibited a lower endurance limit. This is an indication that, in contrast to the tensile behaviour, for the high cycle four-point bending fatigue behaviour of MIM components the pores are not the most significant parameter. Instead, the grain size seems to be much more relevant.

As described before, the boron addition induces a refinement of the microstructure. It is known that refinement of the microstructure can promote an increase of the Ti-6Al-4V alloy fatigue strength, e.g. from 440 to 670 MPa as reported in [86]. Furthermore, the TiB particles are expected to effectively decrease the slip length when compared to the slip length of fully lamellar Ti-6Al-4V alloy [136]. Therefore, the reduction of the slip length, which means a more homogeneous distribution of dislocation densities, is assumed to be one of the main origins for the significant enhancement of the fatigue behaviour by adding boron as performed in this work.

In this investigation, it was assumed so far, that the crack nucleation is related to dislocation pile-up at critical points (e.g. pores), leading to the formation of facets in the crack nucleation region of the fracture surface. As can be seen in Fig. 87, these facets

and pores were also observed in the assumed crack nucleation location of Ti-6Al-4V-0.5B samples. In addition another mechanism that might be determinant for the crack nucleation is the evidence of interfacial decohesion around the TiB particles as appointed by the white arrows in Fig. 87. Such mechanism was proposed before by Soboyejo et al. [149] in order to explain the fatigue results obtained for an ingot Ti-6Al-4V-0.5B alloy.

Flat surfaces as an indication of slip band fracture and micro cracks are typical features of the crack front profile near the assumed crack nucleation site (Fig. 89). The micro cracks exhibited microscopic deflection, which is a well known mechanism for the crack propagation behaviour of $\alpha + \beta$ titanium alloys with a lamellar microstructure [141]. Furthermore, micro cracks apparently are formed near TiB particles, which is a further indication of the interfacial decohesion mechanism between the matrix and the TiB particles as clearly illustrated in Fig. 90. Most probably, such phenomenon is associated to stress concentration promoted by the particles and due to the dislocation pile-up at the particles.

As a result, for nearly fully dense materials, it is possible to assume that a fine microstructure can tolerate a higher number of defects than a coarse microstructure. It is also important to note that apart from the typical crack nucleation mechanisms of the Ti-6Al-4V alloy fabricated by MIM technology, a further mechanism, the interfacial decohesion between matrix and TiB particles, apparently occurs during crack nucleation in the Ti-6Al-4V-0.5B alloy.

7. Conclusions

In the present work, the high cycle four-point bending fatigue behaviour of a Ti-6Al-4V alloy processed by MIM was investigated and evaluated. Critical process parameters and the most relevant microstructural features responsible for the fatigue behaviour of the MIM parts were identified and assessed. Based on the results obtained in this study, it is proposed that the factors determining the fatigue behaviour of MIM Ti-6Al-4V components can be ranked in the following order of relevance:

- 1st: Surface quality
- 2nd: Microstructure (grain size)
- 3rd: Porosity
- 4th: Foreign particles (e.g. oxides)

The amounts of interstitial elements were not considered in the above ranking, since the observed variation of oxygen equivalent turned out to be irrelevant to describing the mechanical properties of the MIM Ti-6Al-4V components investigated. However, such an assumption is only valid for the oxygen equivalent range ($O_{eq} = 2598 - 3238 \mu\text{g/g}$) investigated.

The MIM Ti-6Al-4V samples sintered at 1250 °C with 31 vol. % binder in the feedstock exhibit a fatigue strength degradation of approximately 39 % compared to the annealed, wrought Ti-6Al-4V alloy with a lamellar microstructure. This occurs mainly due to the presence of notches at the surface of the MIM samples. Such notches are assumed to be created during the injection and debinding processes.

A better surface quality is achieved by using feedstock with higher binder content and as a result, superior fatigue behaviour is obtained. A clear relationship between the type of porosity (open or closed) and the tensile properties is observed. However, variations in porosity (3.6 – 5.7 %) surprisingly did not affect the fatigue behaviour of Ti-6Al-4V alloy components fabricated by MIM. This is an indication that, at these specific porosity levels, the surface quality and grain size are the main factors that influence the fatigue behaviour, not the porosity.

Typical features such as facets and pores are always present in the assumed crack nucleation site of the MIM samples. Dislocation pile-ups at critical, preferential locations such as e.g. notches, grain boundaries, pores and oxide particles are assumed to be responsible for the crack initiation mechanism, which promotes the occurrence of facets on the fatigued fracture surfaces.

Shot peening was successfully used to generate residual compressive stresses in the surface regions via local plastic deformation and practically remove notches. As a result the fatigue behaviour improves and cracks tend to initiate in subsurface regions instead of at the surface. For high quality surfaces obtained by shot peening, the residual compressive stresses are the main factor responsible for the enhancement of the fatigue behaviour.

The elimination of pores by using HIP led to significant improvements in the mechanical properties. In terms of the yield strength an increase of 17 % was observed, however, for the fatigue behaviour the improvement was only around 11 %. Such behaviour might be related to the coarsening of the microstructure promoted by the HIP processing. Possible oxide particles are the determining defect class in the absence of porosity.

The samples consolidated directly from powder by applying a HIP process exhibit a drastic change in the microstructure compared to the microstructure of the MIM samples. This microstructural refinement promotes a significant improvement in the mechanical properties. The powder+HIP samples have an approximately 28% higher endurance limit than the MIM+HIP samples.

Since the refinement of the microstructure seems to be more relevant than the presence of pores in terms of fatigue behaviour, a small addition of boron was added to the Ti-6Al-4V during the MIM process. The refinement of the microstructure occurs mainly due to the fact that TiB particles act as new nucleation sites for the α phase (heterogeneous nucleation) and as pinning sites to restrict grain growth. Such a pinning effect promotes a delay in the starting point of the sintering process. On the other hand, this effect is beneficial for densification in the later stages of sintering due to the delayed separation of pores and grain boundaries.

The significant improvement in the fatigue behaviour to an endurance limit of approximately 640 MPa is most probably related to the finer grain size. Common features such as facets and pores are present at the assumed crack nucleation location. Apart from these features, a further mechanism involving the interfacial decohesion between matrix and TiB particles may have occurred during the crack nucleation process. Moreover, it is important to emphasise that even with approximately 2 vol.% of residual porosity, the samples with boron exhibited higher fatigue resistance than the MIM+HIP samples (samples with no pores).

As a matter of fact, the results presented in this investigation demonstrate that it is possible to produce MIM parts with sound mechanical properties even in terms of high cycle fatigue behaviour. Consequently, entirely new application possibilities may be considered by designers and engineers in terms of using the MIM technology for the manufacture of highly loaded components for sectors such as biomedical, aerospace and automobile industries.

8. Suggestions for future work

The fatigue behaviour of the MIM component is mainly determined by the presence of notches on the surface, which is assumed to be related to the MIM process (injection and debinding steps). It was demonstrated that the amount of binder plays an important role in the size of such notches. However, it is necessary to investigate systematically the influence of other parameters such as:

- different particle morphology, e.g. instead of spherical powder, an irregular powder might be applied.
- different binder system, e.g. a binder based on naphthalene. With this experiment it would be possible to evaluate the effect of a different debinding process, in this case sublimation of the naphthalene, on the size of the notches.

The presence of fine and coarse dimples on the tensile fracture surface of the MIM samples need to be careful investigated. A detailed investigation focused on dislocation concentration, low grain boundaries and possible preferential concentration of carbon or oxygen in the microstructure of the sintered samples needs to be performed to elucidate this phenomenon.

The exact influence of impurity levels on the mechanical properties of the MIM components remains unclear. The results so far suggested that a critical point might exist. A methodological investigation on the relationship among amount of porosity, oxygen equivalent and mechanical properties is necessary.

It should be noted that this study was a preliminary investigation of the boron addition influence on the MIM Ti-6Al-4V alloy. It is clear that more research is needed in order to evaluate the relationship between mechanical properties and boron addition content.

The development of the microstructure during sintering and cooling steps for the samples with small addition of boron is still not totally understood. In situ experiments might be helpful in order to describe the mechanisms involved during the process.

The biocompatibility of the Ti-6Al-4V alloy with small boron additions should be systematically investigated in order to evaluate a possible degradation of this property. Furthermore, another interesting property that should be investigated is the effect of boron addition on the corrosion resistance.

References

- [1] S. Anken, C.A. Greene, *Materials Science and Engineering A* 236 (1999) 127-131.
- [2] E. Nyberg, M. Miller, K. Simmons, K. S. Weil, *Material Science and Engineering C* 25 (2005) 336-342.
- [3] K. Faller, F. H. Froes, *Journal of Metals* 52 (2004) 27-28.
- [4] J.C. Williams, E.A. Starker, *Acta Materialia* 51 (2003) 5775-5799.
- [5] F.H. Froes, J. E. Smngeresky, in: *Proceedings of TMS-ALME Symposium, Las Vegas, 1980*, p. 175.
- [6] Y. Itoh, T. Harikou, K. Sato, H. Miura, *Improvement of ductility for injection moulding Ti-6Al-4V alloy*, in: *PM2004*, vol 4, EPMA, Wien, 2004.
- [7] M. Niinomi, T. Akahori, M. Nakai, K. Ohnaka, Y. Itoh, K. Sato, T. Ozawa, *Mechanical properties of $\alpha + \beta$ type titanium alloys fabricated by metal injection molding with targetting biomedical applications*, in: N. Gungor, M.A. Iman, F.H. (Sam) Froes (Eds.), *TMS*, 2007, pp. 209-217.
- [8] F.H. Froes, S.J. Mashl, V.S. Moxson, J.C. Hebeisen, V. A. Duz, *Journal of Metals* (2004) 46-48.
- [9] J. O. Peters, R. O. Ritchie, *International Journal of Fatigue* 23 (2001) 413-421.
- [10] T. Akahori, M. Niinomi, *Materials Science and Engineering A* 243 (1998) 237-243.
- [11] M.Y.P. Costa, H.J.C. Voorwald, W.L. Pigatin, V.A. Guimaraes, M. O. H. Cioffi, *Materials Research* 9 (2006) 107-109.
- [12] N. Tsuiji, S. Tanaka, T. Takasugi, *Materials Science and Engineering A* 488 (2008) 139-145.
- [13] *Titanium and titanium alloys*, edited by C. Leyens and M. Peters, Wiley-VCH, 2003.
- [14] G. Lütjering, J. C. Williams, *Titanium*, Springer, Heidelberg, Germany, 2003.
- [15] H. Conrad, *Acta Metallurgica* 14 (1966) 1631-1633.
- [16] B. D. Meester, M. Doner, H. Conrad, *Metallurgical Transactions A* 6 (1975) 1965-1975.
- [17] P. S. Prevey, *Fatigue and Fracture*, American Society for Metals, Metal Park, 1986, p. 829-853.

-
- [18] H. M. Conrad, M. Doner, B. D. Meester, Critical review deformation and fracture, in: International Conference on Titanium, Proceedings of Titanium Science and Technology, Boston, 1973, p. 969.
- [19] R. W. Judy, I. L. Caplan, F. D. Bogar, Effects of oxygen and iron on the environmental and mechanical properties of unalloyed titanium, in: F. H. Froes, J. Caplan (Eds.), Titanium '92, TMMS, 1993, pp. 2073-2080.
- [20] G. Welsch, W. Bunk, Metallurgical and Materials Transactions A 13 (1982) 889-899.
- [21] K. Schwartzwalder, Ceramic Bulletin 28 (1949) 459-461.
- [22] R. M. German, Powder injection molding, Metal powder industries federation, Princeton, New Jersey, 1990.
- [23] R. M. German, A. Bose, Injection molding of metals and ceramics, MPIF, Princeton, 1997.
- [24] C. H. Ji, N. H. Loh, K. A. Khor, S. B. Tor, Materials Science and Engineering A 311 (2001) 74-82.
- [25] B.C. Mutsuddy, R. G. Ford, Ceramic injection molding, Chapman & Hall, London, 1995.
- [26] T. Hartwing, G. Veltl, F. Petzoldt, H. Kunze, R. Scholl, B. Kieback, Journal of the European Ceramic Society 18 (1998) 1211-1216.
- [27] F.H. Froes, J. R. Pickens, Journal of Metals (1984) 14-28.
- [28] C. I. Chung, B. O. Rhee, M. Y. Cao, C. X. Liu, Advances in Powder Metallurgy 3 (1989) 67-78.
- [29] N. H. Loh, S. B. Tor, K. A. Khor, Journal of Materials Processing Technology 108 (2001) 398-407.
- [30] P. T. Vielma, A. Cervera, B. Levenfeld, A. Várez, Journal of the European Ceramic Society 28 (2008) 763-771.
- [31] W. Limberg, E. Aust, T. Ebel, R. Gerling, B. Oger, Metal Injection Molding of an Advanced Bone Screw Ti-6Al-7Nb Alloy Powder, in: PM 2004, vol 4, EPMA, Wien, 2004, pp. 436-441.
- [32] K.S. Weil, E. Nyberg, K. Simmons, Journal of Materials Processing Technology 176 (2006) 2005-2209.

-
- [33] B. Huang, S. Liang, X. Qu, *Journal of Materials Processing Technology* 137 (2003) 132-137.
- [34] Y. Li, L. Li, K. A. Khalil, *Journal of Materials Processing Technology* 183 (2007) 432-439.
- [35] M. J. Edirisinghe, J. R. G. Evans, *Journal of Materials Science* 22 (1987) 269-277.
- [36] V. V. Bilovol, L. Kowalski, J. Duszczyk, L. Katgerman, *Journal of Materials Processing Technology* 178 (2006) 194-199.
- [37] R. Heldele, S. Rath, L. Merz, R. Butzbach, M. Hagelstein, J. Haußelt, *Nuclear Instruments and Methods in Physics Research B* 246 (2006) 211-216.
- [38] Y. Li, F. Jiang, L. Zhao, B. Huang, *Material Science and Engineering A* 362 (2003) 292-299.
- [39] M. R. Barone, J. C. Ulicny, *Journal of American Ceramic Society* 73 (1990) 3323-3333.
- [40] M. J. Cima, J. A. Lewis, A. D. Devoe, *Journal of American Ceramic Society* 72 (1989) 1192-1199.
- [41] J. G. Zhang, M. J. Edirisinghe, R. G. Evans, *Industrial Ceramics* 9 (1989) 72-82.
- [42] R. M. German, *Sintering Theory and Practice*, John Wiley & Sons, New York, 1996.
- [43] E. A. Olevsky, *Materials Science and Engineering R* 23 (1998) 41-100.
- [44] R. M. German, Z. A. Munir, *Journal of Materials Science* 10 (1975) 1719-1724.
- [45] C. Herring, *Journal of Applied Physics* 21 (1950) 301-303.
- [46] R. F. Walker, *Journal of the American Ceramic Society* 38 (1955) 187-197.
- [47] M. Braginsky, V. Tikare, E. Olevsky, *International Journal of Solids and Structures* 42 (2005) 621-636.
- [48] J. S. Reed, *Principles of Ceramics Processing*, John Wiley & Sons, New York, 1995.
- [49] F. V. Lenel, *Powder Metallurgy and Metal Ceramics* 3 (1964) 523-529.
- [50] C. Herring, *Journal of Applied Physics* 21 (1950) 437-445.
- [51] A. Taskinen, *Journal of Materials Science* 15 (1980) 2253-2257.
- [52] M. N. Rahaman, L. C. D. Jonghe, *Journal of the American Ceramic Society* 69 (1986) 53-58.

- [53] P. Balakrishnan, B. N. Murty, K. P. Chakraborty, R. N. Jayaraj, C. Ganguly, *Journal of Nuclear Materials* 297 (2001) 35-42.
- [54] J. E. Burke, *Journal of the American Ceramic Society* 40 (1957) 80-85.
- [55] Z. He, J. Ma, *Ceramics International* 27 (2001) 261-264.
- [56] R. J. Brook, *Journal of the American Ceramic Society* 52 (1969) 56-57.
- [57] J. Liu, A. Lal, R. M. German, *Acta Metallurgica* 47 (1999) 4617-4626.
- [58] T. Fujita, A. Ogawa, C. Ouchi, H. Tajima, *Materials Science and Engineering A* 213 (1996) 148-153.
- [59] M. N. Gungor, K. R. Reasbeck, I. Ucock, L. S. Kramer, H. Dong, W. T. Tack, *Microstructures and mechanical properties of extruded and cast Ti-6Al-4V*, in: S. A. M. Ninomi, M. Ikeda, M. Hagiwara, K. Maruyama (Ed.) *Ti-2007 Science and Technology*, The Japan Institute of Metals, 2007, pp. 391-394.
- [60] F. H. Froes, *Powder Metallurgy and Metal Ceramics* 46 (2007) 303-310.
- [61] F. H. S. Froes, *Advances in titanium metal injection molding*, in: N. Gungor, M.A. Iman, F.H. (Sam) Froes (Eds.), TMS, 2007, pp. 157-166.
- [62] B. Oger, T. Ebel, W. Limberg, *The manufacture of highly-ductile and geometrically complex MIM-parts based on TiAl6V4*, in: *EUROPOM 2006*, vol 2, EPMA, 2006, pp. 191-196.
- [63] R. Zhang, J. Kruszewski, J. Lo, *A study of the effects of sintering parameters on the microstructure and properties of PIM Ti6Al4V alloy*, in: N. Gungor, M.A. Iman, F.H. (Sam) Froes (Eds.), TMS, 2007.
- [64] G. Shibo, Q. Xuanhui, H. Xinbo, Z. Ting, D. Bohua, *Journal of Materis Processing Technology* 173 (2006) 310-314.
- [65] T. Ebel, *Powder Injection Moulding International* 2 (2008) 21-30.
- [66] Y. Li, X. M. Chou, L. Yu, *Powder Metallurgy and Metal Ceramics* 49 (2006) 236-239.
- [67] E. S. Thian, N. H. Loh, K. A. Khor, S. B. Tor, *Biomaterials* 23 (2002) 2927-2938.
- [68] R. R. Boyer, G. Welsch, E. W. Collings, *Materials Properties Handbook: Titanium Alloys*, International Materials Park, OH, 1994.
- [69] F. H. Froes, R. M. German, *Metal Powder Report* 5 (2000) 12-21.
- [70] J. Schijve, *International Journal of Fatigue* 25 (2003) 679-702.
- [71] A. Wöhler, *Zeitschrift für Bauwesen* 20 (1870) 73-106.

- [72] C. Bathias, *Fatigue and Fracture of Engineering Materials and Structure* 22 (1999) 559-565.
- [73] M. Klesnil, P. Lukas, *Fatigue of metallic materials*, Elsevier, Amsterdam, 1980.
- [74] S. Suresh, *Fatigue of materials*, Cambridge University Press, New York, USA, 1991.
- [75] U. Krupp, *Fatigue Crack Propagation in Metals and Alloys*, Wiley-VCH, Weinheim, 2007.
- [76] R. O. Ritchie, Y. Murakami, *Comprehensive Structural Integrity*, Elsevier Pergamon, Oxford, 2003.
- [77] S.V. Nair, J.K. Tien, R.C. Bates, O. Buck, *Fracture Mechanics: Microstructure and Micromechanisms*, ASM International, Ohio, 1987.
- [78] J. C. Grosskreutz, *Physics Status Solid* 47 (1971) 11.
- [79] N. F. Moot, *Acta Metallurgica* 6 (1958) 195-197.
- [80] A. H. Cottrell, D. Hill, *Extrusion and Intrusion by Cyclic Slip in Copper*, in: *Proceedings of the Royal Society of London. Series A. Mathematical and Physical Sciences*, vol 242, 1957, pp. 211-213.
- [81] E. A. Starke, G. Lutjering, *Fatigue and Microstructure*, American Society for Metals, Metal Park, Ohio, 1979.
- [82] K. Miller, *The Three Thresholds for Fatigue Crack Propagation*, in: R. S. Piascik, J. C. Newman, N. E. Dowling (Eds.), *Fatigue and Fracture Mechanics*, ASTM STP 1296, vol 27th, 1997, pp. 267-286.
- [83] H. Kitagawa, S. Takahashi, *Applicability of fracture mechanics to very small cracks or the cracks in the early stage*, in: *International Conference on Mechanical Behaviour of Materials*, American Society of Metals, Metal Park, OH, 1976, pp. 627-631.
- [84] K. S. Chan, *International Journal of Fatigue* 32 (2010) 526-534.
- [85] C. Leyens, M. Peters, *Titanium and titanium alloys*, Wiley-VCH, 2003.
- [86] C.A. Stubbington, A. W. Bowen, *Journal of Material Science* 9 (1974) 941-947.
- [87] R.K. Nally, B.L. Boyce, J.P. Campbell, J.O. Peters, R. O. Ritchie, *Metallurgical and Materials Transactions A* 33 (2002) 899-918.
- [88] A. N. Stroh, *The formation of cracks as a result of plastic flow*, in: *Proceedings of the Royal Society of London*, London, 1954, pp. 404-414.

- [89] M. R. Bache, *International Journal of Fatigue* 21 (1999) 105-111.
- [90] A.L. Pilchak, A. Bhattacharjee, A.H. Rosenberger, J. C. Williams, *International Journal of Fatigue* 31 (2009) 989-994.
- [91] K. Tanaka, T. Mura, *Journal of Applied Mechanics* 48 (1981) 97-103.
- [92] K. Tanaka, T. Mura, *Metallurgical and Materials Transactions* 13A (1982) 117-123.
- [93] K. S. Chan, *Metallurgical and Materials Transactions* 34A (2003) 43-58.
- [94] S. Tamirisakandala, R.B. Baht, J.S. Tiley, D.B. Miracle, *Scripta Materialia* 53 (2005) 1421-1426.
- [95] E. W. Collings, *Physical metallurgy of titanium alloys*, ASM, Metal Park, OH, 1984.
- [96] D.F. Neal, P. A. Blenkinsop, *Acta Materialia* 24 (1975) 59-63.
- [97] A. W. Bowen, *Acta Materialia* 23 (1975) 1401-1409.
- [98] R.J. Morrissey, D.L. McDowell, T. Nicholas, *International Journal of Fatigue* 21 (1999) 679-685.
- [99] S.A. Namjoshi, V.K. Jain, S. Mall, *Engineering Material and Technology* 124 (2002) 222-228.
- [100] X.P. Jiang, C.S. Man, M.J. Shepard, T. Zhai, *Materials Science and Engineering A* 468-470 (2007) 137-143.
- [101] H. Gray, L. Wagner, G. Lütjering, in: H. Wohlfahrt, R. Kopp, O. Vöhringer (Eds.), *Shot Peening*, DGM, 1987, pp. 467-476.
- [102] X.P. Jiang, C.-S. Man, M.J. Shepard, T. Zhai, *Materials Science and Engineering A* 468-470 (2007) 137-143.
- [103] G. Lütjering, *Materials Science Engineering A* 243 (1998) 32-45.
- [104] P. S. Prevey, *Fatigue and fracture*, in: *Metal Handbook*, vol 19, Metal Park, 1986, pp. 829-853.
- [105] A. Gysler, G. Lütjering, *Metallurgical Transactions A* 13 (1982) 1435-1443.
- [106] R. Zhang, J. Kruszewski, J. Lo, *Powder injection moulding international* 2 (2008) 74-78.
- [107] B. Weiss, R. Stickler, H. Sychra, *Metal Powder Report* 45 (1990) 187-192.
- [108] A. Hadrboletz, B. Weiss, *International Materials Reviews* 42 (1997) 1-44.
- [109] N. Chawla, X. Deng, *Materials Science and Engineering A* 390 (2005) 98-112.

- [110] N. Chawla, T.F. Murphy, K.S. Narasimhan, M. Koopman, K. K. Chawla, *Materials Science and Engineering A* 308 (2001) 180-188.
- [111] K.D. Christian, R. M. German, *International Journal Powder Metallurgy* 1 (1995) 51-61.
- [112] D. E. Dieter, *Mechanical Metallurgy*, MCGraw-Hill, New York, 1986.
- [113] A.W. Thompson, J.C. Williams, J.D. Frandsen, J. C. Chesnutt, The effect of microstructure on the fatigue crack propagation rate in Ti-6Al-4V, in: J.C. Williams, A. F. Belov (Eds.), *Titanium and titanium alloys: scientific and technological aspects*, Plenum Press, 1982, pp. 691-704.
- [114] B. Venkatesh, D.L. Chen, S. D. Bhole, *Scripta Materialia* 59 (2008) 291-394.
- [115] E. D. Tabachnikova, A. V. Podolskiy, V. Z. Bengus, S. N. Smirnov, M. I. Bidylo, K. Csach, J. Miskuf, L. R. Saitova, I. P. Semenova, R. Z. Valiev, *Mat. Scie. and Eng. A* (2008).
- [116] R. Zhang, J. Kruszewski, J. Lo, *Powder injection moulding international* 2 (2008) 74-78.
- [117] C. Xu, B. Weiss, G. Khatibi, H. Danninger, Ultra high cycle fatigue behaviour of high density PM alloy steels, in: *PM 2004*, vol 3, EPMA, Wien, 2004, pp. 36-41.
- [118] R.B. Wassenberg, O.F. Nurol, P.Beiss, Bending fatigue of a high performance PM steel, in: *PM 2004*, vol 3, EPMA, Wien, 2004, pp. 133-138.
- [119] S. Akaslan, S. Saritas, R.J. Causton, W.B. James, T.F. Murphy, A. Lawley, Effect of porosity and microstructural inhomogeneities on the fatigue crack growth response of a sinter-hardenable hybrid PM steel, in: *PM 2004*, vol 3, EPMA, Wien, 2004, pp. 117-126.
- [120] D.B. Lanning, T. Nicholas, G.K. Haritos, *International Journal of Fatigue* 27 (2005) 45-57.
- [121] G.K. Haritos, T. Nicholas, D.B. Lanning, *International Journal of Fatigue* 21 (1999) 643-652.
- [122] J. Mueller, T. Ludian, H.J. Rack, L. Wagner, Microstructural and mean stress effects in fatigue performance of shot peened Ti-6Al-4V, in: *Ti-2007 Science and Technology*, The Japan Institute of Metals, 2007, pp. 375-378.
- [123] R.K. Nalla, B.L. Boyce, J.P. Campbell, J.O. Peters, R. O. Ritchie, *Metallurgical and Materials Transactions A* 33 (2002) 899-918.

- [124] R.L. Barrie, T.P. Gabb, J. Telesman, P.T. Kantzos, A. Prescenzi, T. Biles, P. J. Bonacuse, *Materials Science and Engineering A* 474 (2007) 71-81.
- [125] N. Tsuji, S. Tanaka, T. Takasugi, *Surface & Coatings Technology* 203 (2009) 1400-1405.
- [126] Q. Wang, H. Yin, X. Qu, J. L. Johnson, *Powder Technology* 193 (2009) 15-19.
- [127] R. M. German, *Powder Metallurgy Science*, MPIF, Princeton, 1984.
- [128] T.A. Kals, R. Eckstein, *Journal of Materials Processing Technology* 103 (2000) 95-101.
- [129] L.V. Raulea, A.M. Goijaerts, L.E.K. Govaert, F. P. T. Baaijens, *Journal of Materials Processing Technology* 115 (2001) 44-48.
- [130] A. Kohyama, K. Hamada, H. Matsui, *Journal of Nuclear Materials* 179-181 (1991) 417-420.
- [131] J.F. Michel, P. Picart, *Journal of Materials Processing Technology* 141 (2003) 439-446.
- [132] K. J. Miller, W. J. O'Donnell, *Fatigue and Fracture Engineering Materials and Structure* 22 (1999) 545-557.
- [133] Y. Komizo, H. Terasaki, M. Ikeda, F. Nishino, M. Toudai, Fine-grained titanium by inclusion-assisted microstructure control in: *Ti-2007 Science and Technology*, 2007, pp. 741-744.
- [134] S.V. Divinski, F. Hisker, T. Wilger, M. Friesel, C. Herzig, *Intermetallics* 16 (2008) 148-155.
- [135] I. Sen, U. Ramamurty, Mechanical behaviour of B modified Ti-6Al-4V alloys, in: *Ti-2007 Science and Technology*, 2007.
- [136] W. Chen, C. J. Boehlert, *Materials Science and Engineering A* 494 (2008) 132-138.
- [137] M.J. Bermingham, S.D. McDonald, K. Nogita, D.H.ST. John, M. S. Dargusch, *Scripta Materialia* 59 (2008) 538-541.
- [138] P. E. Zovas, R. M. German, *Metallurgical Transactions A* 15 (1984) 1103-1110.
- [139] D. Hill, R. Banerjee, D. Huber, J. Tiley, H. L. Fraser, *Scripta Materialia* (2005) 387-392.
- [140] H. Feng, Y. Zhou, D. Jia, Q. Meng, *Material Science and Engineering A390* (2005) 344-349.

-
- [141] X. Zhang, W. Lü, D. Zhang, R. Wu, *Scripta Materialia* 41 (1999) 39-46.
- [142] S.S. Sahay, K.S. Ravichandran, R. Atri, *Journal of Material Research* 14 (1999) 4214-4223.
- [143] Z.Y. Ma, S.C. Tjong, L. Gen, *Scripta Materialia* 42 (2000) 367-373.
- [144] G. Wen, S.B. Li, B.S. Zhang, Z. X. Guo, *Acta Materialia* 49 (2001) 1463-1470.
- [145] S. Tamirisakandala, R.B. Bhat, V.A. Ravi, D. B. Miracle, *Journal of Metals* (2004) 60-63.
- [146] R. Srinivasan, D. Miracle, S. Tamirisakandal, *Materials Science and Engineering A* 487 (2008) 541-551.
- [147] I. Sen, S. Tamirisakandala, D.B. Miracle, U. Ramamurty, *Acta Materialia* (2007) 4983-4993.
- [148] T.M.T. Godfrey, A. Wisbey, P.S. Goodwin, K. Bagnall, C. M. Ward-Colse, *Materials Science and Engineering A* 282 (2000) 240-250.
- [149] W.O. Soboyejo, W. Shen, T. S. Srivatsan, *Mechanics of Materials* 36 (2004) 141-159.

Tables

Table 1 – Crystal structure, lattice parameters, and fractional coordinates in TiB and TiB ₂	28
Table 2. Chemical concentration of interstitial alloying element.....	36
Table 3. Tensile properties of the Ti-6Al-4V ELI (ASTM Grade 23) and the MIM31L samples.	37
Table 4. Microstructural features of samples sintered at a maximum temperature of 1250 °C and 1350 °C with different binder content.	42
Table 5. Tensile property and fracture surface analysis.	44
Table 6. Chemical concentration of interstitial alloying element of MIM35H and MIM35H+SP+HT samples.....	53
Table 7. Microstructural features and tensile properties of MIM35H and 25MIM35L samples.	57
Table 8. Microstructural features and impurity levels of MIM35H samples with and without HIP.	60
Table 9. Tensile properties of MIM35H with and without HIP.	60
Table 10. EDX of the fine particles and the facet regions.....	63
Table 11. Chemical concentration of interstitial alloying element of Ti-6Al-4V alloy powder and Ti-6Al-4V alloy powder+HIP.....	65
Table 12. Tensile properties of Powder+HIP and MIM35H samples	66
Table 13. EDX of the particle and the matrix (Fig. 71).....	69
Table 14. Microstructural features of Ti-6Al-4V-0.5B and MIM35H samples	74
Table 15. Tensile properties of Ti-6Al-4V-0.5B and MIM35H.....	79

Table 16. Selected samples for the evaluation of the surface quality influence..... 88

Table 17. Selected samples for the evaluation of the shot peening 93

Table 18. Selected samples for the evaluation of the porosity influence. 95

Table 19. Selected samples for the evaluation of the grain size influence..... 98

Figures

Fig. 1. Figure (a) illustrates the processing route for fully lamellar microstructure, and (b) the resultant microstructure..... 3

Fig. 2. Figure (a) illustrates the processing route for fully equiaxed microstructure, and (b) the resultant microstructure..... 4

Fig. 3. Figure (a) illustrates the processing route for bi-modal microstructure, and (b) the resultant microstructure. 5

Fig. 4. A schematic diagram of the processing steps, equipments involved and sample configuration in powder injection moulding. 7

Fig. 5. A schematic comparison of the sequential feedstock flow in progressive mould filling and jetting [22]..... 8

Fig. 6. Possible defects in a MIM component that might be noted after debinding or sintering process [22]. 10

Fig. 7. Grain size and pore size interaction during sintering, showing the condition where breakaway may occur [56]..... 12

Fig. 8. Schematic illustration of single slip system of intrusion formation [80]. 15

Fig. 9. Schematic of the growth of microstructurally short cracks in a polycrystal..... 17

Fig. 10. High cycle fatigue behaviour of Ti-6Al-4V alloy obtained by different processes route [85]..... 17

Fig. 11. Stroh’s model to describe quasi-cleavage facets formed in titanium alloys [88]. 18

Fig. 12. A schematic showing the fatigue crack initiation process along a planar slip band due to dislocation pile-up. (d) is referring to grain size and (h) is the slip band width [91]. 19

Fig. 13. Scanning electron microscope image (SE-mode) of the powder size fraction used for the present metal injection moulding experiments. 20

Fig. 14 – Geometry of bending fatigue specimens. Dimensions of as sintered part and measured in millimetres..... 21

Fig. 15 - Geometry of “dog-bone” tensile test specimen. Dimensions of as sintered part and measured in millimetres..... 21

Fig. 16. HIP process cycle..... 24

Fig. 17. Typical MIM lamellar microstructure; a) α colony size; b) β grain size..... 27

Fig. 18. Quasi-equiaxed microstructure; a) α grain size, b) α colony size. 27

Fig. 19. Micro-tensile specimen geometry. Dimensions are in millimetres..... 29

Fig. 20. BSE image of the reference material microstructure (equiaxed microstructure). 33

Fig. 21. S-N curve for reference materials samples with shot peening (SP)..... 33

Fig. 22. Microstructure of MIM Ti-6Al-4V with 31 vol.% of binder and sintered at 1250 °C for two hours (MIM31L)..... 35

Fig. 23. Pore diameter distribution and cumulative probability for MIM31L samples.. 36

Fig. 24. Typical tensile fracture surface of MIM31L samples. Pores and dimples are visible. 37

Fig. 25. S-N curves for MIM31L samples and the standard material [9]..... 38

Fig. 26. Surface quality of MIM31L samples. 39

Fig. 27. Typical fracture surface of MIM31L samples. The black line indicates the position where the crack front profile (Fig. 29) was evaluated. 39

Fig. 28. Typical fracture surface of MIM31L samples: (a) lower magnification and (b) higher magnification of the assumed crack initiation location..... 40

Fig. 29. Typical crack front profile of MIM31L samples. 40

Fig. 30. Higher magnification of the crack front profile at crack nucleation site: (a) BSE image, (b) SE image. 41

Fig. 31. Microstructure of MIM Ti-6Al-4V with 35 vol.% of binder and sintered at 1250 °C (MIM35L). 42

Fig. 32. Microstructure of MIM Ti-6Al-4V with 35 vol.% of binder and sintered at 1350 °C (MIM35H). 43

Fig. 33. Pore diameter distribution and cumulative probability for MIM35L samples.. 43

Fig. 34. Pore diameter distribution and cumulative probability for MIM35H samples. 44

Fig. 35. Typical tensile fracture surface of MIM35L samples. Pores and dimples are visible. 45

Fig. 36. Typical tensile fracture surface of MIM35H samples. Pores and dimples are visible. 45

Fig. 37. S-N curves for MIM31L, MIM35L and MIM35H samples. 46

Fig. 38. Surface quality of the MIM35H samples. 47

Fig. 39. Surface quality of the MIM35L samples. 47

Fig. 40. Typical fracture surface of MIM35L samples. Possible crack nucleation region. 47

Fig. 41. Typical fracture surface of MIM35H samples. Possible crack nucleation region. 48

Fig. 42. S-N curves for MIM31L samples with and without shot penning (SP)..... 49

Fig. 43. S-N curves for MIM35H samples with and without shot penning (SP). 49

Fig. 44. Surface quality of the MIM31L samples with shot peening..... 50

Fig. 45. Surface quality of the MIM35H samples with shot peening..... 50

Fig. 46. Typical fracture surface of MIM31L samples. The black line indicates the position where the crack front profile (Fig. 49) was evaluated. 51

Fig. 47. Typical fracture surface of MIM31L samples with shot peening: (a) lower magnification and (b) higher magnification of crack initiation location..... 51

Fig. 48. Typical fracture surface of MIM31L samples (Fig. 42 with parentheses) with shot peening and (a) lower magnification (b) higher magnification of crack initiation location. 51

Fig. 49. Typical crack front profile of MIM31L samples with shot peening..... 52

Fig. 50. Higher magnification of the crack front profile at crack nucleation site of MIM31L samples with shot peening, BSE image mode. 52

Fig. 51. Typical microstructure of the MIM35H+SP+HT samples..... 53

Fig. 52. S-N curve of the MIM35H, MIM35H+SP and MIM35H+SP+HT samples..... 54

Fig. 53. Typical fracture surface of MIM35H+SP+HT samples, (a) lower magnification (b) higher magnification of crack initiation location..... 55

Fig. 54. Microstructure of MIM Ti-6Al-4V with 35 vol.% of binder, particle size below 25 μm and sintered at 1250 $^{\circ}\text{C}$ (25MIM35L)..... 56

Fig. 55. Pore diameter distribution and cumulative probability for 25MIM35L samples. 56

Fig. 56. S-N curves for 25MIM35L and MIM35H samples. All samples were exposed to shot peening (SP) prior to testing. 58

Fig. 57. Typical fracture surface of 25MIM35L samples. 58

Fig. 58. Typical fracture surface of 25MIM35L samples with shot peening: (a) lower magnification and (b) higher magnification of crack initiation location..... 59

Fig. 59. Microstructure of MIM35H samples after HIP process..... 59

Fig. 60. Typical tensile fracture surface of MIM35H+HIP samples. An fine dimpled structure is visible..... 61

Fig. 61. S-N curves for MIM31L and MIM35H+HIP samples. All samples were exposed to shot peening (SP) prior to testing..... 61

Fig. 62. BSE micrograph of a typical fracture surface of MIM+HIP samples with shot peening. 62

Fig. 63. Typical fracture surface of MIM35H+HIP samples with shot peening: (a) lower magnification and (b) higher magnification of crack initiation location..... 62

Fig. 64. Typical fracture surface of MIM35H + HIP samples with shot peening at higher magnification of crack initiation location. White arrows (a) and (b) indicated the EDX analysed regions. 63

Fig. 65. Microstructure of Powder+HIP samples..... 64

Fig. 66. EBSD phase map of Powder+HIP sample: representation of the (a) BSE image, (b) α phase and (c) β phase. Each colour (gray scale for copy) is related to a specific orientation..... 65

Fig. 67. Tensile fracture surfaces of Powder + HIP samples: (a) 10 % of plastic elongation, (b) 17 % of plastic elongation..... 67

Fig. 68. Typical tensile fracture surface of the MIM35H samples (micro-tensile specimens)..... 67

Fig. 69. S-N curves for MIM35H, MIM35H+HIP and Powder+HIP samples. All samples were exposed to shot peening (SP) prior testing. 68

Fig. 70. Typical fracture surface of Powder + HIP samples with shot peening: (a) lower magnification and (b) higher magnification of crack initiation location..... 68

Fig. 71. Typical fracture surface of Powder+HIP samples with shot peening. Higher magnification at the assume crack nucleation site. The particle is highlighted by the white line. 69

Fig. 72. Microstructure of Ti-6Al-4V alloy sintered at 1250 °C for two hours and 10 °C/min cooling rate..... 70

Fig. 73. Microstructure of Ti-6Al-4V-0.1B alloy sintered at 1250 °C for two hours and 10 °C/min cooling rate..... 71

Fig. 74. Microstructure of Ti-6Al-4V-0.5B alloy sintered at 1250 °C for two hours and 10 °C/min cooling rate..... 71

Fig. 75. Relative densification of Ti-6Al-4V alloy with and without addition 0.5 wt.% of boron at two different maximum sintering temperatures: 1250 °C and 1400 °C..... 72

Fig. 76. Dilatometry of Ti-6Al-4V and Ti-6Al-4V-0.5B alloys: a) linear shrinkage (LS) and b) linear shrinkage rate (LSR). Starting acquisition data at 75 °C. 73

Fig. 77. Microstructure of Ti-6Al-4V-0.5B alloy sintered at 1400 °C for two hours a cooling rate of 10 °C/min. 74

Fig. 78. Pore diameter distribution and cumulative probability for Ti-6Al-4V-0.5B samples. 75

Fig. 79. EBSD phase map of Ti-6Al-4V-0.5B sintered at 1400 °C: representation of the (a) BSE image, (b) α phase, (c) β phase and (d) TiB particles. Each colour (gray scale for copy) is related to a specific orientation. 76

Fig. 80. High magnification EBSD phase map for Ti-6Al-4V-0.5B sintered at 1400 °C. (a) BSE image, (b) α phase. 76

Fig. 81. Electron backscattered diffraction patterns obtained from TiB particles in Ti-6Al-4V-0.5B alloy. a) EBSD pattern, b) indexed EBSD pattern. 77

Fig. 82. Pole figures of the phases presented in Fig. 79. (a) α phase, (b) β phase and (c) TiB particles. 77

Fig. 83. EBSD phase map of Ti-6Al-4V sintered at 1400 °C: representation of the (a) BSE image, (b) α phase and (c) β phase. Each colour (gray scale for copy) is related to a specific orientation..... 78

Fig. 84. Typical tensile fracture surface of Ti-6Al-4V-0.5B. Fine and coarse dimpled structures and pores are visible. Additionally, broken and debound TiB particles are indicated by the white arrows..... 79

Fig. 85. S-N curves for MIM35H, MIM35H+HIP and Ti-6Al-4V-0.5B alloy. All samples were exposed to shot peening (SP) prior to testing. 80

Fig. 86. Typical BSE micrograph of the fracture surface. The black line indicates the approximately position where the crack front profile (Fig. 88) was evaluated..... 81

Fig. 87. Typical fracture surface of Ti-6Al-4V-0.5B with shot peening at the assumed crack nucleation site. 81

Fig. 88. Typical crack front profile of Ti-6Al-4V-0.5B samples 82

Fig. 89. High magnification of the crack front profile (Fig. 88). Directed at the assumed crack nucleation site. 82

Fig. 90. Crack propagation interaction with TiB particle..... 83

Abbreviations index

BSE	Backscattering electrons image mode
CIM	Ceramic injection moulding
EBSD	Electron backscattering diffraction
EBSPs	Electron backscattering diffraction Kikuchi patterns
EDX	Energy dispersive X-ray spectroscopy
ELI	Extra low interstitial
EVA	Polyethylene vinyl acetate
HDH	Hydride-dehydride Ti powders
HIP	Hot isostatic pressing
LEFM	Linear elastic fracture mechanics
LS	Linear shrinkage
LSR	Linear shrinkage rate
MIM	Metal injection moulding
MFM	Microstructure fracture mechanics
O _(Eq.)	Equivalent oxygen
OPS	Struers oxide polish suspension
PIM	Powder injection moulding
PM	Powder metallurgy
SE	Secondary electron image mode
SEM	Scanning electron microscopy
SP	Shot peening
σ_y	Yield strength
UTS	Ultimate tensile strength

Curriculum Vitae

Name: Orley Milagres Ferri
Address: Bahnstraße 49, 21502 Geesthacht, Germany
Email: orley.milagres.ferri@volkswagen.de
Date of birth: 22.04.1981
Place of birth: Belo Horizonte, MG, Brasil
1999-2004: Graduation in Materials Engineering
Federal University of Santa Catarina, UFSC, Santa Catarina, Brazil
Thesis (Diplomarbeiten): Energy Balance of Electric Arc Furnaces
Supervisors: Dr. Ing. Andreas Opfermann, and Professor, Dr. Ing. Berend Snoeijer
2004-2006: Master of Science at Technische Universität Hamburg-Harburg
Erasmus Mundus scholarship granted by EMMS (Joint European Masters in Materials Science)
Master Thesis: Effect of Periodic Overloads on Fatigue Crack Propagation in Ti-6Al-4V
Supervisors: Professor Dr. Joachim Albrecht, and Dr. Ing. Jens Heidemann
2006-2010: Research Assistant at GKSS Research Center
Topic of doctoral thesis: Optimisation of fatigue behavior of Ti-6Al-4V alloy components fabricated by Metal Injection Moulding (MIM)
Supervisor: Professor Dr. Rüdiger Bormann
Actual Position: Engineer at Volkswagen AG, Baunatal, Germany